Master's thesis

Implementation and Characterization of a Three-Mode Circuit QED System

Markus Sifft

At the Faculty for Physics and Astronomy at the Ruhr-University Bochum
and the Institute of Quantum Optics and Quantum Information, Innsbruck

Bochum 2019

RUB

IQI
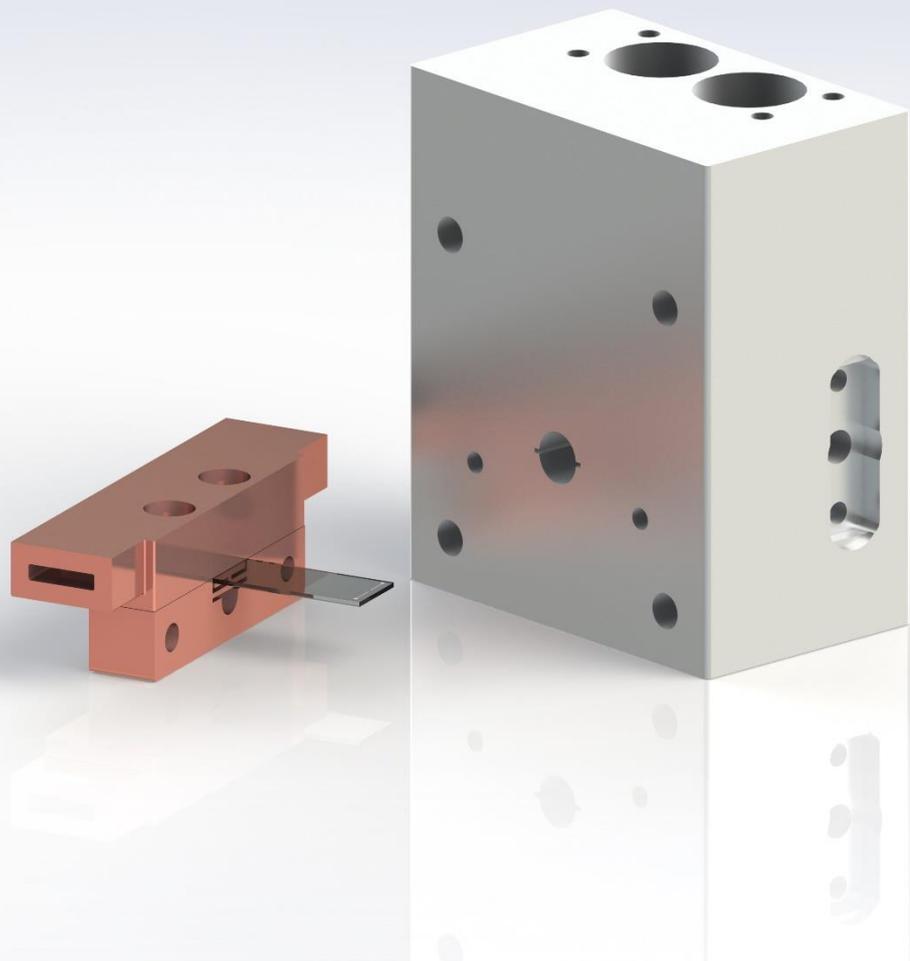
The institutions responsible for the supervision of this thesis are the Ruhr University Bochum, Germany, and the University Innsbruck, Austria. It was financed by the student exchange programme Erasmus+. The work described in this thesis was performed in the research group of Superconducting Quantum Circuits at the Institute for Quantum Optics and Quantum Information (IQOQI) of the Austrian Academy of Sciences and at the Institute for Experimental Physics at the University of Innsbruck, both located in Innsbruck, Austria.

1. Gutachter: Prof. Dr. D. Hägele
2. Gutachter: Univ.-Prof. Dr. Gerhard Kirchmair

Summary

Even though remarkable improvements have been made over the last decades, short coherence times are still a limiting factor for quantum computation. One solution to this problem could be the storage of the quantum state within highly coherent superconducting microwave cavities. These systems show a lifetime and coherence time of multiple milliseconds, whereas quantum states in transmon qubits decay in the tens of microseconds scale. Therefore, in this thesis, a cavity-qubit system is designed, which would allow for the transfer of the transmon state into a long-lived photonic mode within the cavity.

To achieve this goal, we designed a system, which consists of two cavities coupled to one qubit. One of the cavities is intended to be used as a storage for the transmon state. The other one is a readout resonator for the qubit. The cavities are both coaxial $\lambda/4$ resonators since they show a high quality factor while still being relatively easy to fabricate. The Hamiltonian parameters of the system are optimized via simulations.

For fabrication of the cavities, we used high purity aluminum (5N) and niobium to compare the performance of both materials. The transmon circuit is fabricated on a 330-µm-thick sapphire chip and can be inserted into the cavities.

We characterized the cavity-qubit system to confirm the simulated Hamiltonian parameters and to determine the lifetime and coherence time of the cavities and the qubit. Without inserting the qubit, we find a cavity lifetime of up to 0.69(4) ms, which is 17 times longer than the transmon's lifetime of 14.5 µs. The Hamiltonian parameters match those of the simulation up to an error of around 10 %. Moreover, we compared the calculation of the parameters, e.g., the state-dependent dispersive shift, via the fourth-order approximation and the numerical diagonalization. The results can deviate by more than 40 %.

Zusammenfassung

Obwohl in den letzten Jahrzehnten große Fortschritte bei der Realisierung eines Quantencomputers erzielt wurden, sind zu kurze Lebensdauern der Qubits immer noch einer der limitierenden Faktoren. Eine mögliche Lösung für dieses Problem wäre die Speicherung eines Quantenzustands in einer supraleitenden Mikrowellenkavität. Diese Systeme zeigten Lebens- und Kohärenzzeiten von mehreren Millisekunden, wohingegen der Zustand in Transmon-Qubits bereits nach einigen 10 μs zerfällt. Deshalb wird in dieser Arbeit ein Kavität-Qubit-System entworfen, das es ermöglicht, den Zustand des Qubits auf die langlebige Mode in der Kavität zu übertragen.

Das System besteht aus zwei Kavitäten, die an dasselbe Transmon-Qubit gekoppelt sind. Dabei könnte eine der Kavitäten zum Speichern des Qubitzustands und die andere zum Auslesen verwendet werden. Es handelt sich bei den Kavitäten um koaxiale $\lambda/4$-Resonatoren, da diese bekannt für ihre hohen Gütefaktoren und den relativ einfachen Herstellungsprozess sind. Das System wurde zunächst simuliert, um die Kopplungsparameter zu optimieren.

Die Kavitäten wurden sowohl aus hochreinem Aluminium (5N) und Niob hergestellt, um die beiden Materialien vergleichen zu können. Als Substrat für das Transmon wurde Saphir mit einer Dicke von 330 μm verwendet. Der Chip kann in das Kavitätensystem eingesetzt werden.

Das System wurde anschließend charakterisiert und die Werte mit der Simulation verglichen. Die Lebensdauer eines Zustands in der Kavität beträgt bis zu 0.69(4) ms, was der 17-fachen Lebensdauer des Transmons (14.5 μs) entspricht. Die Simulation stimmt mit einem Fehler von etwa 10 % mit den Messwerten überein. Es konnte gezeigt werden, dass die Kopplungsparameter, die über eine Näherung des Hamiltonoperators bis zur vierten Ordnung bestimmt wurden, von der exakten Diagonalisierung über 40 % abweichen können.

Contents

List of Figures

List of Tables

Acknowledgements

This work would not have been possible without the support of many people. I am grateful for all the experiences that I was fortunate enough to gather over the last years and especially the most recent one here in Austria led to a much deeper understanding of the topics I was working on, but also to leaps forward in my personal development.

First and foremost, I want to thank my advisor and supervisor GERHARD KIRCHMAIR not only for making the last few months possible but also for introducing me to superconducting qubits and microwave circuits. No matter how long of a day it has already been, his door was always open and he was keen to answer all of my questions in a private mini-lecture fashion. Thank you for that.

The second part of the foundation for this thesis was laid by my advisor and supervisor at my home university DANIEL HÄGELE, who without hesitation agreed to support me in my decision of conducting this scientific work abroad. Furthermore, I would like to thank you for the great lectures throughout the year before I started my master's thesis. Walking into the lectures has always been a thrill and walking out a little enlightenment.

The first members of the group, which convinced me to stay at the Institute for Quantum Optics and Quantum Information (IQOQI) in Innsbruck, were ALEKSEI SHARAFIEV and CHRISTIAN SCHNEIDER. Thinking back almost two years, I can vividly remember the day trip, which I took to get to know the people who are working in the superconducting group at the IQOQI. I want to thank the two quantum pioneers mentioned above not only for taking some time off and explaining the details of the different group projects and the science behind them but also for sharing their knowledge with me.

Moreover, since a considerable part of my work consisted of simulations, I am indebted to PHANI MUPPALLA and DAVID ZÖPFL, who had the patience to introduce me to all the magic functions of HFSS, which was extremely helpful to get started. Additionally, I am grateful for their help whenever I had follow-up questions.

The software infrastructure and all the custom python libraries were also something I had to get used to in the beginning, and therefore I would like to thank OSCAR GARGIULO for all the support, whenever I had a "bug", which was really just me forgetting a bracket or two. Moreover, it was a great experience working with you in the lab, even when we had to close the cryostat late at night.

I surely want to thank Paul Heidler because his recent work laid the foundation for this thesis. I could always discuss the next steps in the project with him and leverage his knowledge to improve my device or experimental setup.

Speaking of devices, all the parts of my experimental setup used throughout this thesis, I could not have fabricated myself. Luckily, one of our group members, MAXIMILIAN ZANNER,

1 Introduction

Since Richard Feynman realized that it appears to be infeasible to calculate an evolution of a quantum system on a classical computer efficiently and proposed his concept of simulating one quantum system by another in 1982 [1], the field of quantum information has come a long way. The advantages of using the quantum behaviour of a system instead of only its classical properties could potentially be so dramatic that this notion has propelled the research journeys of many scientists, including mine. And it is a rapid journey, indeed. It was only in the last century that the first experiments revealed the quantum nature of our universe and the theoretical work at the end of the 20th century set off the race towards one major goal in the field of quantum information: the realization of a universal quantum computer. Figure 1.1 shows a few examples, but there is a tremendous amount of theoretical and experimental papers stating that such a device would enable us to process information faster than a classical computer can [2, 3]. However, theory together with experiments based on the so-called NISQ (Noisy Intermediate-Scale Quantum) devices [4] need to improve even further since, up to now, there exists no device, which could demonstrate *quantum superiority* [5] meaning that this device would be outperforming any classical supercomputer in a specific task.

1982
Richard Feynman proposes quantum computer [1]

1992
David Deutsch and Richard Jozsa develop a task, that can be solved efficiently on a quantum computer [23]

1994
Peter Shor discovers an algorithm to factor larges numbers efficiently with a quantum computer [2]

1996
Lov Grover invents a quantum database search algorithm [3]

2001
A number is factored on a quantum computer at IBM's Almaden Research Center [74]

2002
First operation of an artificial two-level atom on a integrated electrical circuit [75]

2007
Koch et al. introduce the transmon qubit [22]

2012
Superconducting qubit in a waveguide cavity approaches coherence time of 0.1 ms [12]

2014
Using cat states to encode quantum information in cavities [82]

2018
Implementation of two qubits gates for two coupled microwave cavities [84]

2019
Simulation of vibronic molecular spectra with cavity qubits [83]

1980   1990   2000   2010

Figure 1.1: A timeline of the milestones in quantum computing with a focus on the development of superconducting microwave cavities. Since 2000 tremendous improvements have been made in the experimental realization of a universal quantum computer.

The motivation behind these research efforts lies not only in the dream to improve the computational power of humankind but in the fact that classical computers are starting to reach their limits. Moore's Law, stating that the computational power roughly doubles every two years, is slowly coming to an end. A classical processor can only be improved by either increasing its clock speed or by using smaller transistors. The maximum clock speed has long been reached since it is mostly limited by the cooling power that one is willing to supply to the processor. The second nob, which is nearly turned as far as possible, is the transistor size, which is limited by the phenomenon of quantum tunneling [6]. One idea to work around this problem is to simply use multiple processors and run computations in parallel. However, even this approach is bound by the so-called Amdahl's law [7]. Consequently, if we want to solve particularly hard problems, we will need innovative hardware, for which a quantum computer would be a potential candidate.

The fundamental building blocks of a quantum computer are quantum bits (qubits), which are a physical system of which two quantum states are denoted as a *0* and *1* and used for calculations. There have been many ideas for what system could be used as a qubit. Just to name a few, the energy states of the outer electron of an ion has been used as a two-level system [8], and one can also imagine using quantum dots as the building blocks for a quantum computer [9], but one of the most promising approaches are superconducting quantum circuits, which will be used throughout this thesis.

Especially when scaling up the number of qubits, which would allow for computationally more complex tasks, the innate frailty of the physical components of a quantum computer is becoming a fundamental problem. This is because qubits, unlike classical bits, can dephase. Since we have defined a qubit as two degenerate (or nondegenerate) eigenstates of a Hamiltonian, dephasing occurs whenever the energies of these two eigenstates randomly fluctuate in time. Even though the coupling to charges, spins, phonons, stray electric or magnetic fields are relatively weak, they contribute to the energy shift of the eigenstates. Longer coherence times, T_2^*, are required for these quantum systems, as it otherwise becomes an unbearable effort to ensure quantum error correction [10]. Therefore, a tremendous amount of effort has been put into extending the coherence time of superconducting qubits.

We have seen immense improvements over the last decades resulting in an exponential growth in coherence times. With these systems, coherence times of up to a hundred microseconds have been reached [11, 12] and with the shortest gate times in the nanosecond range [13], this approach is close to the threshold required for fault-tolerant quantum computation [14–16]. However, especially for two-qubit gates, a high fidelity comes at the cost of longer control pulses. Therefore, increasing T_2^* even further, would improve gate fidelity and drastically reduce the overhead needed for error correction [10].

The highest coherence times have been achieved by the so-called three-dimensional (3D) transmon qubits. These are superconducting qubits fabricated on a chip and embedded into a 3D microwave cavity. These cavity resonators are already well-developed and frequently used

for the creation and manipulation of non-classical photonic states, which can have a lifetime and coherence time of multiple microseconds [17]. Remarkably, these photonic states can be used as a quantum bit itself, going from a discrete- to a continuous-variable quantum system by encoding information in the larger available Hilbert space [18–20].

With such highly coherent superconducting 3D microwave cavity resonators, we can overcome the lifetime limitations of a quantum state in a superconducting qubit [21] by using the cavity as quantum storage.

In this thesis, a setup containing two superconducting microwave cavities interconnected via a transmon qubit [22] is designed and characterized to lay the foundation for the usage of photonic modes as quantum bits.

1.1 Overview of this thesis

We start by introducing the fundamentals of quantum information in Chapter 2. Here we take a closer look at two-level systems and how they are influenced by measurements and the environment.

In Chapter 3, the components of our system, e.g., quantum circuits and microwave cavities, are presented. This knowledge will also be needed to tailor the system to our experimental needs. After explaining, why transmons are well suited as qubits and how cavities store the electric field, we will see the effects of a coupling between the two.

In Chapter 4, we will dive into the experimental design. It is explained why a carefully shaped cavity is the linchpin of the whole setup and how it is designed using finite element simulations. Moreover, the unique geometry of the qubit interconnecting the two cavities is presented.

Building upon previous work by the group for superconducting quantum circuits at the Institute for Quantum Optics and Quantum Information, we fabricated the cavities out of two materials, aluminum and niobium. This process, together with the fabrication of the on-chip qubit, is presented in Chapter 5.

Before starting with the experiments, we will present our measurement setup in Chapter 6. It is shown how the signals for probing the cavities and controlling the qubits are generated and transported. Moreover, we will have a closer look at the amplifiers, which are crucial components for the readout of the cavity response.

Combining all the work in chapter 7, we will use the measurement techniques described earlier to characterize the whole system. We extract the lifetimes and coherence times of the cavities and the qubit and measure the coupling strength between the qubit and each cavity.

The closing chapter of this thesis provides a conclusion and will give an outlook on how the measurement data could be used to refine the system parameters to eventually incorporate it into the design of a universal quantum computer.

2 The fundamentals of quantum information

The smallest physical system to carry any information is one with two distinguishable states. These states can encode one bit of information and are referred to as *0* and *1*. By connecting n of such systems (bits), one can encode 2^n different states. To extract information out of this sequence of bits, it needs to be processed by an algorithm, which is described by specific operations working on the sequence. The output can then be decoded to provide the desired information.

Entering the quantum regime, the state of the system is defined by a wavefunction, and in contrast to the classical system, one of the quantum systems can also be in a superposition of its two states. While there are many theoretical and philosophical approaches to define (quantum) information, we here settle for the notion that quantum information is the one needed to fully describe a quantum system by providing the probability of the possible outcomes of measurements on this system.

In the last part of the 20th century, more and more scientists took advantage of the intrinsic probabilistic nature of quantum states and came up with quantum algorithms to process not a sequence of classical bits but quantum bits. To perform these algorithms, quantum computers, just like their classical counterpart, need the ability to perform a universal set of gates on the qubits. These are called quantum gates, and it is an important problem to find an optimal sequence of gates to perform a certain unitary operation. One possible universal set of quantum gates consists of the Hadamard gate, the S-gate, the T-gate, and a two-qubit operation such as CNOT [13].

Most importantly, we need to understand that the computational power of a quantum computer arises partly from something David Deutsch called *quantum parallelism* [23]. To achieve a quantum speed-up, we not only need to use the quantum gates to prepare superpositions of states, but we also have to entangle the states with each other. Entanglement describes non-classical correlations between pure states. For a two-qubit system, a maximally entangled state is the 2-qubit Bell state: $\frac{1}{\sqrt{2}}\left(|00\rangle + |11\rangle\right)$. With the usage of highly entangled quantum states, we could surpass the capabilities of today's supercomputers by exploiting the ability to perform computations on a superposition of 2^n states giving quantum algorithms like Groover's search [3], the quantum Fourier transform [24] their speed-ups compared to their classical counterparts. With the help of these algorithms we could, for example, simulate the properties of exotic materials and complex molecules more precisely, which in the long run could lead to technological advances, for example, in material science [25] or chemistry [26].
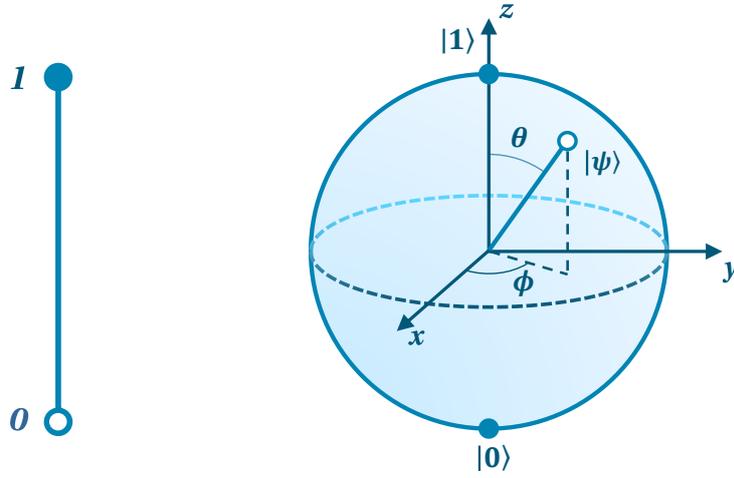
Figure 2.1: **Representation of a single classical (left) and pure quantum state (right).** In contrast to the classical state, the quantum state can be in a superposition of its two states and is represented by a point on the Bloch sphere defined by the two angles θ and ϕ

2.1 Quantum bits

The two states of a qubit acting as a fundamental building block of a quantum computer are basis vectors, which span a two-dimensional complex vector space, and are written as $|0\rangle$ and $|1\rangle$, or $|g\rangle$ and $|e\rangle$ respectively, where $|0\rangle$ represents the ground and $|1\rangle$ the excited state. Since the two quantum states can be in a superposition, the general qubit state is described by its wavefunction

$$|\psi\rangle = \alpha\,|0\rangle + \beta\,|1\rangle\,, \tag{2.1}$$

where α and β are complex numbers and $|\alpha|^2 + |\beta|^2 = 1$ to conserve a probability distribution. ψ is a vector in a two-dimensional Hilbert space, while $|0\rangle$ and $|1\rangle$ provide an orthonormal basis for this space.

Because of the normalization condition, the wavefunction is left with two degrees of freedom. Hence, a single qubit state can be represented by a point on a three-dimensional sphere, called the Bloch sphere shown in Figure 2.1. $|\psi\rangle$ can then be written with the spherical coordinates $\theta \in [0, \pi]$, giving the amplitude of a state within a superposition and the relative complex phase $\phi \in [0, 2\pi)$ as

$$|\psi\rangle = \cos\left(\frac{\theta}{2}\right)|0\rangle + e^{i\phi}\sin\left(\frac{\theta}{2}\right)|1\rangle\,. \tag{2.2}$$

To access any information about a given quantum system, one is required to measure its state. In theory, the measurement outcome can be calculated by defining observables. To conserve the normalization condition and since the operations need to be reversible, the observables are given by Hermitian operators with the system's dimension. Each observable O is built up by a sum of projectors Π_i spanning the Hilbert space of the system. Every projector has a real eigenvalue c_i such that $O = \sum_i c_i \Pi_i$. The probability P_i of observing the outcome c_i is then given by $P_i = \langle\psi| \Pi_i |\psi\rangle$ and the expected value of O by $\langle O \rangle = \langle\psi| O |\psi\rangle$, called the Born rule.

Additionally, during a measurement, the superposition is projected onto the measurement basis. For example, in the case of measuring σ_z, α^2 and β^2 determine the probability that the state of the qubit is projected onto $|0\rangle$ and $|1\rangle$, respectively. α and β can then be extracted, taking measurements on a sufficiently large ensemble of states.

2.2 Coherence of quantum states

In order to exploit the unique features of quantum mechanics, for example, the ability to perform operations on a superposition of states, we have to ensure that the state stays coherent and does not decay significantly during the algorithm. In the experiment, unintended changes of a state can occur due to environmental decoherence or imperfect gate operations. Decoherence occurs because the qubit is always finitely coupled to its environment, by which it is continuously being measured. Therefore, the system is collapsing onto one of its basis states. However, we cannot solve this problem by completely isolating the qubit from its environment since a certain coupling to the outside world is necessary to perform gate operations and readout measurements.

In a two-level system, there are two main types of mechanisms, which are causing decoherence. One is the undesired loss or generation of the population in the excited state at rate $\Gamma_\downarrow$ or $\Gamma_\uparrow$, respectively. This can be explained by the exchange of energy between the qubit and the thermal equilibrium population of its environment n_{th} happening at the timescale T_1, where $1/T_1 = \Gamma_\downarrow + \Gamma_\uparrow$. Another decoherence channel is dephasing. This type of error has no classical counterpart and describes changes in the phase relationship of the complex amplitudes α and β of the state taking place at the timescale T_ϕ.

Either of these processes will lead to the qubit reaching the thermal equilibrium with its environment as its population of states decays exponentially in time. Both decoherence channels contribute to the decoherence time T_2^*, where $1/T_2^* = 1/(2T_1) + 1/T_\phi$. It depends on the system, which mechanism limits the number of operations that can be applied when running an algorithm before all useful information is lost.

To overcome these limits of single qubits, it is our mission to design a cavity system, which can be used either as quantum storage or as a long-lived qubit itself. The following chapters will show how this can be done by coupling the qubit to a mode inside 3D microwave resonators.

3 Cavity and circuit QED

Before diving into the experimental part of this thesis, we have to develop a deep understanding of all the components of our setup. We will start by examining quantum circuits and cavities separately. Afterwards, the qubit-cavity coupling is addressed, which will lead to interesting phenomenons. This knowledge will help to identify the challenges we are facing and the requirements, which have to be met to manipulate quantum states at will.

3.1 Quantum circuits

Many groups are working on the realization of a robust and scalable quantum computer using a variety of different physical systems, such as ion traps [27], diamond nitrogen-vacancy centers [28], and, as in our case, superconducting circuits [29]. As stated in [30], all these systems are required to meet the so-called DiVincenzo criteria, named after David DiVincenzo. These include the ability to encode quantum information in a scalable system with a sufficient coherence time, initialize the qubits in the ground state, and perform measurements on the system after performing a universal set of gate operations.

3.1.1 Requirements for the superconducting circuits

To fulfil these prerequisites, we are using quantized superconducting electrical circuits as qubits, which consist of nonlinear oscillators in the quantum regime. In the general framework of circuit quantum electrodynamics (cQED) in analogy to cavity QED (CQED), these are often referred to as *artificial atoms.*

Superconductivity plays an important role in these systems as it allows for the lossless carriage of electrical signals necessary for the required lifetimes. Additionally, dissipationless nonlinear circuit elements can be constructed when combining superconductors with isolators. Without these, quantum computations could not be performed since otherwise, the eigenenergies of the oscillator's eigenstates would be equidistant, which makes addressing only two states impossible.

During the construction of these circuits, one must consider the energy gap Δ/h of the superconductor as a limit for the energies, which can be used for the excitation of the quantum system [31]. Therefore, this limit also provides an upper bound to the energy difference between the two states of the qubit. To avoid the generation of quasiparticles, the applied drives should be working at $\omega/2\pi < 2\Delta/h$. For aluminum, this means staying below 80–100 GHz.

Moreover, a lower limit for the energy difference between the ground and the excited state of the qubit $\hbar\omega_{ge}$ is given by the temperature, at which the qubits are operated. This is due to the requirement that the oscillators need to be in their quantum mechanical ground state. To reach a thermal excitation of the second state of the qubit of less than one percent, $5k_BT < \omega_{ge}/2\pi$ should be fulfilled. Since a commercial dilution refrigerator will be used for cooling, which is typically operated at temperatures of around 15 mK, $\omega_{ge}/2\pi$ should be greater than approximately 2 GHz. Therefore, the qubits are designed to work within the microwave regime.

3.1.2 Advantages of artificial atoms

In contrast to the usage of real atoms as two-level systems, microwave resonators are human-made objects. They can be fabricated as an integrated circuit on a substrate, which is typically sapphire or silicon. Thus, thanks to well-developed electron-beam and photolithography technologies, the resonators are highly customizable, and the fabrication process is fast and reliable. This provides us with the ability to determine and optimize the system parameters enabling us to meet the requirements above easily.

Lastly, also the sources for microwave signals have many advantages over control mechanisms for other types of qubits. For example, they are more stable than lasers, which are used when working with real atoms, and have more favourable noise properties compared to DC controls used when working with quantum dots as qubits. All these advantages make superconducting cQED systems particularly suitable for the realization of a quantum computer.

3.1.3 Quantum LC oscillators

One of the components required for building a superconducting qubit is an LC circuit operated in its quantum regime. Within an LC circuit, the total energy of the system is oscillating between a capacitance C and an inductance L. The dynamics of the system can be modelled with the Lagrangian $\mathcal{L}$ [32]

$$\mathcal{L} = \frac{LI^2}{2} - \frac{Q^2}{2C}, \tag{3.1}$$

where I is the current through the inductor and Q is the charge on the capacitor. Since the wavelengths of the oscillating current will be much longer than the physical size of the circuit, we can assume that charges are only building up on the capacitor. Consequently, $I = \dot{Q}$ leads to

$$\mathcal{L} = \frac{L\dot{Q}^2}{2} - \frac{Q^2}{2C}. \tag{3.2}$$
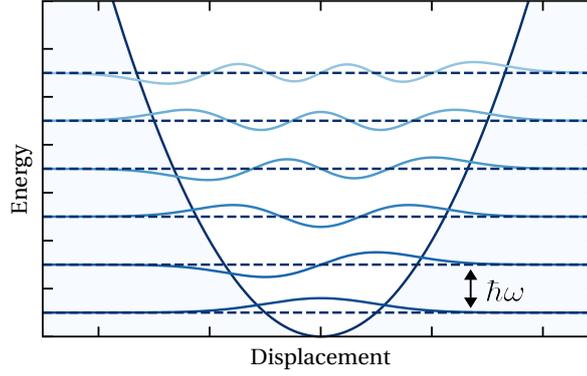
Figure 3.1: **The first six states of a quantum harmonic oscillator.** Due to the parabolic potential, the energy levels are equally spaced by $\Delta E = \hbar\omega$. Because of the zero-point fluctuations, the ground state has a finite probability of being measured at a non-zero value of $\hat{Q}$ or $\hat{\Phi}$

With the help of the Euler-Lagrange equation of motion we calculate

$$\ddot{Q} = -\omega^2 Q \tag{3.3}$$

with the resonance frequency of the resonator $\omega = 1/\sqrt{LC}$ corresponding to the collective motion of the electrons from one plate of the capacitor to the other. We recognize that the so-called node flux Φ is the conjugate variable to Q since $\frac{\delta\mathcal{L}}{\delta Q} = LI = \Phi$ and write the system's Hamiltonian as

$$H = \frac{\delta\mathcal{L}}{\delta Q}\dot{Q} - \mathcal{L} = \frac{\Phi^2}{2L} + \frac{Q^2}{2C}. \tag{3.4}$$

Now the variables can be converted into quantum mechanical operators and using $\hat{x}^2 + \hat{y}^2 = (\hat{x} + i\hat{y})(\hat{x} - i\hat{y}) - i[\hat{x}, \hat{y}]$ the Hamiltonian of the system is given by

$$\hat{H} = \left(\frac{\hat{\Phi}}{\sqrt{2L}} + i\frac{\hat{Q}}{\sqrt{2C}} \right) \left(\frac{\hat{\Phi}}{\sqrt{2L}} - i\frac{\hat{Q}}{\sqrt{2C}} \right) - \frac{i}{2\sqrt{LC}} \left[\hat{Q}, \hat{\Phi} \right]. \tag{3.5}$$

With the definition of the creation operator $\hat{a}^\dagger$ and annihilation operator $\hat{a}$ such that

$$\hat{a} = \frac{1}{\sqrt{\hbar\omega}} \left(\frac{\hat{\Phi}}{\sqrt{2L}} - i\frac{\hat{Q}}{\sqrt{2C}} \right) \tag{3.6}$$

$$\hat{a} = \frac{1}{\sqrt{\hbar\omega}} \left(\frac{\hat{\Phi}}{\sqrt{2L}} + i\frac{\hat{Q}}{\sqrt{2C}} \right), \tag{3.7}$$

we arrive at

$$\hat{H} = \hbar\omega \left(\hat{a}^\dagger \hat{a} + \frac{1}{2} \right). \tag{3.8}$$

This is the Hamiltonian of a simple harmonic oscillator. The associated parabolic potential well and the wavefunctions of the lowest energy states can be seen in Figure 3.1. The eigenstates of this Hamiltonian are known as Fock states $|n\rangle$ with a definite photon number $n = \left\langle \hat{a}^\dagger \hat{a} \right\rangle$. There is an infinite number of eigenstates, and their energies are evenly spaced by $\hbar\omega$.

For the derivation of the Hamiltonian of the LC circuit together with the nonlinear element, introduced later, we also need the inverted version of equation (3.7)

$$\hat{\Phi} = \Phi_{\mathrm{ZPF}} \left(\hat{a}^\dagger + \hat{a} \right) \tag{3.9}$$

$$\hat{Q} = -i Q_{\mathrm{ZPF}} \left(\hat{a}^\dagger - \hat{a} \right), \tag{3.10}$$

where the zero-point fluctuations of the flux and the charge of the ground state are given by $\Phi_{\mathrm{ZPF}} = \sqrt{\hbar Z/2}$ and $Q_{\mathrm{ZPF}} = \sqrt{\hbar/2Z}$, where $Z = \sqrt{L/C}$ is the impedance of the circuit.

One thing to note here is that the whole spectrum only depends on L and C, quantities which can be easily controlled using standard lithography or machining techniques. However, to achieve a nonlinear energy level structure, we need nonlinear circuit elements like the Josephson junction.

3.1.4 The Josephson junction

With the help of a Josephson junction, we can modify the harmonic superconducting LC oscillators such that the energy difference between neighbouring states decreases with higher energies. Before adding this type of junction to the circuit, we will introduce its most important properties.

As shown schematically in Figure 3.2 **A**, a Josephson junction consists of two superconducting islands separated by a thin insulating layer [33]. We will see that with this configuration, one can construct a nonlinear inductor. The Cooper pairs in either of the superconductors can cross the insulating layer by tunnelling between the superconducting islands. Typically, aluminum is used as superconducting material and aluminum oxide as an insulator, which is shown in Figure 3.2 **B**. The supercurrent I and voltage V across the junction can be described by the Josephson equations. These show that I and V depend on the normalized phase difference $\varphi = \frac{\Phi_1 - \Phi_2}{\Phi_0}$ between the wavefunctions of the Cooper pairs or its derivative with respect to time

$$I = I_c \sin\left(\varphi\right) \tag{3.11}$$

$$V = \frac{\Phi_0}{2\pi} \frac{\mathrm{d}\varphi}{\mathrm{d}t}, \tag{3.12}$$

where I_c is the critical current of the junction and $\Phi_0 = h/2e$ is the flux quantum [31, 34].
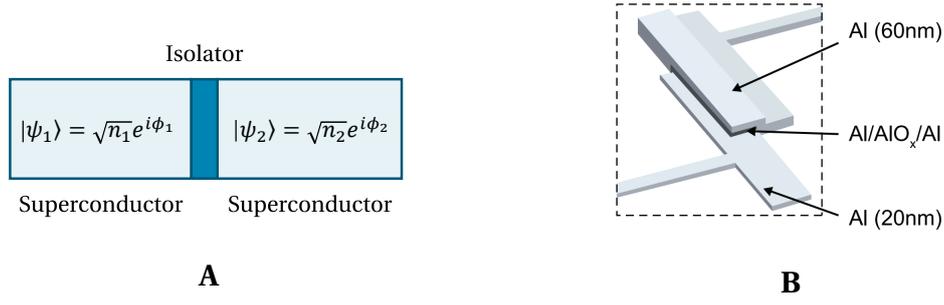
Figure 3.2: **The Josephson junction. A** Schematic representation of a Josephson junction. The superconducting parts are shown in gray separated by an insulating barrier shown in blue. The Cooper pairs in each superconductor can be described by a macroscopic quantum state $|\psi_1\rangle$ and $|\psi_2\rangle$. **B** A cartoon of a Josephson junction [35] fabricated using double-angle electron-beam evaporation. The superconductors are made of tens of nanometers thin aluminum layers, whereas the insulation barrier consists of aluminum oxide.

To see how these nonlinear equations modify the Hamiltonian of the LC circuit, we define the inductance of the junction as $L_\mathrm{J} \equiv V/\dot{I}$ and by calculating the time derivative of the current-phase relation

$$\frac{\mathrm{d}I}{\mathrm{d}t} = I_\mathrm{c}\cos\left(\varphi\right)\cdot\frac{\mathrm{d}\varphi}{\mathrm{d}t} = V\frac{2\pi I_c}{\Phi_0}\cos\left(\varphi\right), \tag{3.13}$$

the inductance L_J is given by

$$L_\mathrm{J} = \frac{\Phi_0}{2\pi I_c \cos\left(\varphi\right)}. \tag{3.14}$$

We see that a change in current with respect to time is related to a voltage across the superconductors nonlinearly. To define the bare Josephson inductance L_0 the cosine term is often ignored, resulting in $L_0 = \frac{\Phi_0}{2\pi I_c}$. For the device used in this thesis, $L_0 \approx 7$ nH. With the Josephson inductance we can calculate the energy stored in the junction

$$E = \int I(t)V(t)\mathrm{d}t \tag{3.15}$$

$$= \frac{\Phi_0}{2\pi}\int I_\mathrm{c}\sin(\varphi)\frac{\mathrm{d}\varphi}{\mathrm{d}t}\mathrm{d}t \tag{3.16}$$

$$= \frac{\Phi_0}{2\pi}\int I_\mathrm{c}\sin(\varphi)\mathrm{d}\varphi \tag{3.17}$$

$$= -E_\mathrm{J}\cos(\varphi). \tag{3.18}$$

Defining the Josephson energy as $E_\mathrm{J} = \Phi_0 I_\mathrm{c}/2\pi$, which can be thought of as the energy associated with an electron tunnelling across the junction, we arrive at the junction part of the Hamiltonian

$$\hat{H}_\mathrm{J} = -E_\mathrm{J}\cos\left(\hat{\varphi}\right). \tag{3.19}$$
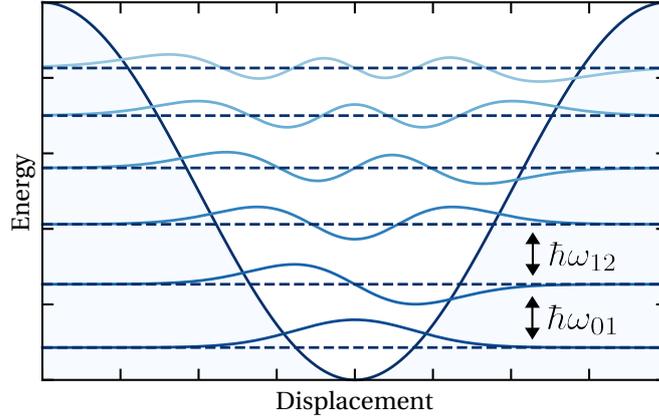
Figure 3.3: **The first six wavefunctions in a cosine potential.** As we go up in energy, the energy gaps between the states decrease, hence $\hbar\omega_{01} > \hbar\omega_{21}$. The wavefunctions have been calculated numerically using the Numerov method [36].

The potential and the first six solutions of the Schrödinger equation are shown in Figure 3.3. This figure already reveals that the further we go up in energy, the narrower the energy gaps between the states become. To quantify this observation, we are defining the anharmonicity of the spectrum. The absolute anharmonicity α_m is defined as the energy difference between the transitions of the state m to m+1 and m-1 to m. One can also think about a relative anharmonicity $\alpha_{r,m} = \alpha_{\mathrm{m}}/E_{01}$, where we relate the energy difference between the states to the first transition. In the next section, we will explore this energy spectrum in more detail.

3.1.5 Transmons as artificial atoms

Many types of superconducting qubits have been developed in the last twenty years only using capacitor pads and Josephson junctions. The first qubits were named after the degree of freedom, which turned out to be a good quantum number depending on the circuit's topology: charge [37–39], flux [40–42], and phase qubits [43, 44]. Further developments showed that hybrid systems, which cannot be assigned to any of these categories since their eigenstates do not correspond to number states of these quantities, have advantageous properties, such as decreased sensitivity to certain noise channels. One of these hybrid systems is known as the transmon [22].

The transmon is essentially an improved version of the Cooper Pair Box (CPB), which is classified as a charge qubit. As shown in Figure 3.4 on the left-hand side, it has a simple topology only consisting of a single Josephson junction. The CPB Hamiltonian is given by

$$\hat{H} = 4E_{\mathrm{C}} \left(\hat{n} - n_{\mathrm{g}} \right)^2 - E_{\mathrm{J}} \cos \left(\hat{\varphi} \right), \tag{3.20}$$

where $\hat{n}$ is the number of Cooper pairs transferred between the separated superconductors.
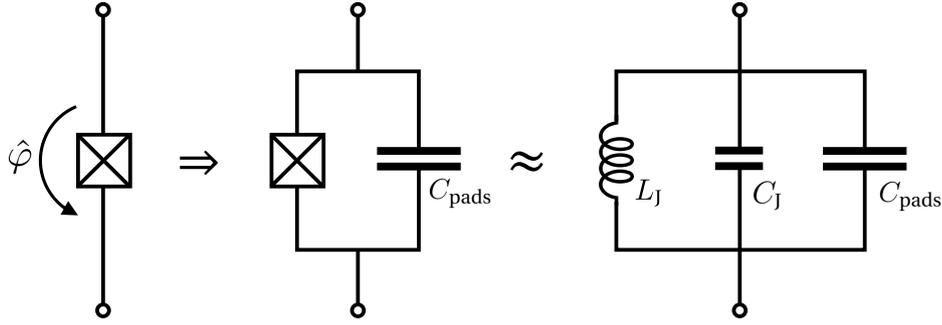
Figure 3.4: **The circuit representation of the Cooper Pair Box (CPB) on the left and the transmon in the middle and on the right.** The Josephson junction is depicted as a boxed cross. To build a transmon from a CPB, we have to shunt it with a large capacitance C_{pads}. The Josephson junction itself can be decomposed into the nonlinear inductance L_{J} and a small junction capacitance C_{J}.

n_{g} is the effective offset charge measured in units of the Cooper pair charge $2e$ contributing to the capacitive energy $E_{\text{C}} = \frac{e^2}{2C_{\Sigma}}$, where $C_{\Sigma} = C_{\text{g}} + C_{\text{J}}$ is the sum of the geometric capacitance C_{g} and the capacitance of the Josephson junction C_{J}. Before solving the Schrödinger equation, we can build some intuition for the system by finding a physical analogue for this Hamiltonian: a charged quantum rotor [22]. We are imagining a point-mass m attached to a massless rod of length l, which can be rotated freely around a fixed point. The gravitational field causes the potential energy of the mass to be $V = -mgl \cdot \cos(\varphi)$, where φ is the angle of the rod relative to its equilibrium position. Using the angular momentum $\hat{L}_z = (\vec{r} \times \vec{p}) \cdot \hat{z} = i\hbar \frac{\partial}{\partial \varphi}$, the full Hamiltonian is given by

$$\hat{H}_{\text{rotor}} = \frac{\hat{L}_z^2}{2ml^2} - mgl \cos(\varphi).\tag{3.21}$$

The integer values of $\hat{L}_z/\hbar$ can be mapped to $\hat{n}$ since the number of Cooper pairs, which can tunnel across the junction is an integer quantity. Moreover, we find $E_{\text{J}} \leftrightarrow mgl$ and $E_{\text{C}} \leftrightarrow \hbar^2/8ml^2$. Therefore, H_{rotor} is identical to the CPB Hamiltonian with $n_{\text{g}} = 0$. This term can be added by modifying H_{rotor} such that the mass carries some charge and is in a uniform magnetic field parallel to the rotor's axis. We use $\vec{p} \to \vec{p} - q\vec{A}$ resulting in $L_{\text{z}} \to L_{\text{z}} + \frac{1}{2}qB_0l^2$, where $\vec{A} = B_0(-y, x, 0)/2$ is the vector potential of the magnetic field. We finalize the analogy by identifying $n_{\text{g}} \leftrightarrow qB_0l^2/2\hbar$.

When solving for the energy levels of the CPB system and plotting them against the effective offset charge n_{g}, we arrive at Figure 3.5 a. As one can see, the eigenenergies are highly dependent on the offset charge. Therefore, charge noise is a significant source of decoherence if the qubit is not operated at the degeneracy point. The arrows are indicating one of these sweet spots, at which the first derivative with respect to n_{g} is vanishing. As it turns out, the effect of charge
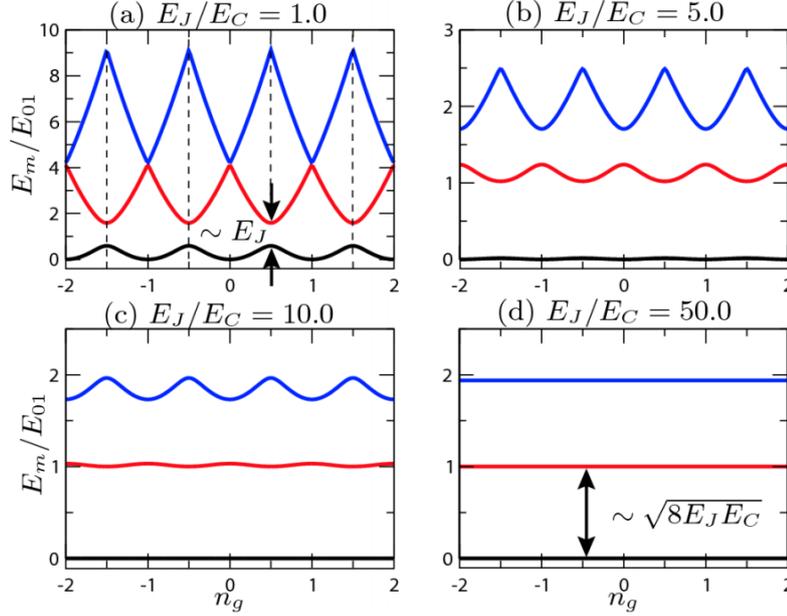
Figure 3.5: **The first three eigenenergies E_m of the qubit Hamiltonian as a function of the effective offset charge n_g.** The larger the ratio between E_J and E_C, the less charge sensitive the eigenenergies E_m [22].

noise is highly dependent on the ratio between E_J and E_C and almost vanishes for large values of E_J/E_C, as shown in Figure 3.5 b–d. Therefore, we want to shunt the Josephson junction by a large capacitance, which will be contributing to E_C. The protection against charge noise can be achieved by fabricating it such that $100 < E_J/E_C < 10^4$, where the transmon essentially becomes a flat-banded multilevel system [22], in which the eigenstates are superpositions of several charge states. Figure 3.6 shows a transmon with its large shunting capacitors and the Josephson junction in between them. However, there is a downside to this approach, as it leads to the cosine flux-dependence of the junction behaving increasingly like a parabolic potential, therefore, reducing the anharmonicity. Luckily, the sensitivity to n_g is suppressed exponentially with $\sqrt{8E_J/E_C}$ while the desired relative anharmonicity of the qubit only decreases algebraically with a slow power law. So, by shunting the Josephson junction, we can reduce the transmons sensitivity to charge noise improving T_2^*. To find an expression for the anharmonicity of a transmon, we make use of the fact that a transmon is operated in a regime where $\varphi \ll 1$. Therefore, we can treat the anharmonicity as a perturbation of a harmonic oscillator and extend the cosine to fourth order obtaining

$$\hat{H} = 4E_\mathrm{C}\hat{n}^2 - E_\mathrm{J} + \frac{E_\mathrm{J}\hat{\varphi}^2}{2} - \frac{E_\mathrm{J}\hat{\varphi}^4}{24}, \tag{3.22}$$

Figure 3.6: **Picture of a transmon inside a 3D cavity.** The large shunting capacitors (light gray) are clearly visible on the silicon substrate (dark gray), whereas the Josephson junction in between them is too small to be seen. The substrate is mounted in a copper cavity.

where the n_g dependence has been removed since it is exponentially small and in a perturbative approach even zero because of the lacking periodicity of the Hamiltonian above. With the creation and annihilation operators $\hat{b}^\dagger$ and $\hat{b}$ for the quadratic part, the Hamiltonian can be rewritten in the form of a Duffing oscillator

$$\hat{H} = \sqrt{8E_\mathrm{C}E_\mathrm{J}} \left(\hat{b}^\dagger\hat{b} + \frac{1}{2} \right) - E_\mathrm{J} - \frac{E_\mathrm{C}}{12} \left(\hat{b}^\dagger + \hat{b} \right)^4. \tag{3.23}$$

The first-order corrections to the energies of the quadratic term are

$$E_\mathrm{m} = -E_\mathrm{J} + \sqrt{8E_\mathrm{C}E_\mathrm{J}} \left(m + \frac{1}{2} \right) - \frac{E_\mathrm{C}}{12} \left(6m^2 + 6m + 3 \right). \tag{3.24}$$

With this correction term, the absolute anharmonicity α_m reads

$$\alpha_m = E_\mathrm{m+1,m} - E_\mathrm{m,m-1} \tag{3.25}$$

$$\alpha = \alpha_1 \approx -E_\mathrm{C}, \tag{3.26}$$

whereas the relative anharmonicity with $E_{01} = \sqrt{8E_\mathrm{C}E_\mathrm{J}}$ is given by

$$\alpha_\mathrm{r,m} \approx - \left(8E_\mathrm{J}/E_\mathrm{C} \right)^{-1/2}. \tag{3.27}$$

Therefore, the anharmonicity is weak when $E_\mathrm{J}/E_\mathrm{C} \gg 1$, which is fulfilled in the transmon regime validating our perturbative approach. A sufficient suppression of dephasing due to charge noise is achieved for $E_\mathrm{J}/E_\mathrm{C} \geq 50$ [45]. Typical values for a transmon as such as in the experiments later would be a transition frequency of $\omega_\mathrm{ge}/2\pi = 6\,\mathrm{GHz}$ with an energy ratio of $E_\mathrm{J}/E_\mathrm{C} = 150$, which results in an anharmonicity of 173 MHz.

How can we modify our quantum rotor analogue of a CPB to correspond to a transmon? A large shunting capacitance can be modelled as a very large moment of inertia and gravitational pull, so $\varphi \ll 1$. Again, we can expand the cosine and separate the rotor Hamiltonian into $\hat{H}_{\text{rotor}} = \hat{H}_{\text{lin}} + \hat{V}$, where $\hat{H}_{\text{lin}} = 4e_{\text{C}}\hat{n}^2 + \frac{E_{\text{J}}}{2}\hat{\varphi}^2$ describes a simple Harmonic oscillator with the frequency $\hbar\omega = \sqrt{8E_{\text{J}}E_{\text{C}}}$ and $\hat{V}$ is the perturbation

$$\hat{V} = -E_{\text{J}}\left(\frac{1}{4!}\hat{\varphi}^4 - \frac{1}{6!}\hat{\varphi}^6 + ...\right). \tag{3.28}$$

Since we can neglect the periodicity of the cosine potential, there is no need to fulfil $\psi(\varphi) = \psi(\varphi + 2\pi)$. We can eliminate the vector potential by a gauge transformation, and the effect of an offset charge n_{g} only matters in the rare event of a full 2π rotation.

3.1.6 Controlling the transmon's state

To perform calculations with our artificial atom, we are using microwave signals to rotate the state vector around the Bloch sphere. Since only one qubit will be operated, we are introducing single-qubit gates, which, in our case, are realized with short microwave pulses. For a two-level system, these can be described using the Pauli matrices

$$\hat{\sigma}_x = \begin{pmatrix} 0 & 1 \\ 1 & 0 \end{pmatrix} \quad \hat{\sigma}_y = \begin{pmatrix} 0 & -i \\ i & 0 \end{pmatrix} \quad \hat{\sigma}_z = \begin{pmatrix} 1 & 0 \\ 0 & -1 \end{pmatrix}. \tag{3.29}$$

To see the effect of these operators on the state of the qubit, we have to calculate the time evolution of the system. Generally, this can be done by using the Schrödinger equation with the state vector $|\psi(t)\rangle$

$$i\hbar\frac{\partial}{\partial t}|\psi(t)\rangle = \hat{H}(t)|\psi(t)\rangle. \tag{3.30}$$

We are going to decompose the qubit Hamiltonian $\hat{H}_{\text{qubit}}$ into the system's part $\hat{H}_0$, which is assumed to be time-independent, and the drive's part $\hat{H}_{\text{d}}$, which accounts for the control pulses:

$$\begin{aligned} \hat{H}_{\text{qubit}} &= \hat{H}_0 + \hat{H}_{\text{d}} \\ &= -\frac{\hbar\omega_{\text{ge}}}{2}\hat{\sigma}_z + \Omega f(t)\hat{\sigma}_y, \end{aligned} \tag{3.31}$$

where $f(t)$ is a continuous wave drive, and Ω is known as the Rabi frequency.

Before analyzing the time evolution of the qubit Hamiltonian, we are calculating the propagator U of the static system's part:

$$i\hbar\frac{\partial}{\partial t}\left|\psi(t)\right\rangle = \hat{H}_0\left|\psi(t)\right\rangle$$

$$\left|\psi(t)\right\rangle = \exp\left[\frac{-i\hat{H}_0 t}{\hbar}\right]\left|\psi(0)\right\rangle$$

$$= U\left|\psi(0)\right\rangle. \tag{3.32}$$

Since we are only interested in the effects of the drive, we can use this propagator to move into the *rotating frame* or the *interaction picture*. For this, we choose a new time-dependent basis

$$\left|\Theta(t)\right\rangle = \hat{U}^\dagger\left|\psi(t)\right\rangle. \tag{3.33}$$

In this new basis, the time evolution under the qubit Hamiltonian is given by

$$i\hbar\frac{\partial}{\partial t}\left|\Theta(t)\right\rangle = i\hbar\left(\frac{\partial\hat{U}^\dagger}{\partial t}\left|\psi(t)\right\rangle + U^\dagger\frac{\partial}{\partial t}\left|\psi(t)\right\rangle\right)$$

$$= -\hat{H}_0\hat{U}\hat{U}^\dagger\left|\Theta(t)\right\rangle + \hat{U}^\dagger\left(\hat{H}_0 + \hat{H}_{\mathrm{d}}\right)\hat{U}\left|\Theta(t)\right\rangle$$

$$= \hat{U}^\dagger\hat{H}_{\mathrm{d}}\hat{U}\left|\Theta(t)\right\rangle$$

$$= \hat{H}'\left|\Theta(t)\right\rangle, \tag{3.34}$$

where we used $\partial\hat{U}^\dagger/\partial t = \left(i\hat{H}_0/\hbar\right)U$ and $\left[\hat{U},\hat{H}\right] = 0$. With Equation (3.31) we now arrive at

$$\hat{H}' = \hbar\Omega f(t)e^{-i\omega_{\mathrm{ge}}t\hat{\sigma}_z/2}\sigma_y e^{-i\omega_{\mathrm{ge}}t\hat{\sigma}_z/2}$$

$$= \hbar\Omega f(t)\begin{pmatrix} 0 & -ie^{-i\omega_{\mathrm{ge}}t} \\ ie^{i\omega_{\mathrm{ge}}t} & 0 \end{pmatrix}$$

$$= i\hbar\Omega f(t)\left(e^{i\omega_{\mathrm{ge}}t}\hat{\sigma}^+ - e^{-i\omega_{\mathrm{ge}}t}\hat{\sigma}^-\right) \tag{3.35}$$

with $\hat{\sigma}^\pm = \frac{1}{2}\left(\hat{\sigma}_x \mp i\hat{\sigma}_y\right)$. The drive is set to be on resonance with the qubit transition frequency:

$$f(t) = \sin\left(\omega_{\mathrm{ge}}t + \phi\right)$$

$$= -\frac{i}{2}\left(e^{i(\omega_{\mathrm{ge}}t+\phi)} - e^{-i(\omega_{\mathrm{ge}}t+\phi)}\right). \tag{3.36}$$

This equation can be substituted into Equation (3.35). After neglecting the terms, which oscillate quickly at $2\omega_{\mathrm{ge}}$ and therefore average out to zero, $\hat{H}'$ can be written as

$$
\begin{aligned}
\hat{H}' &= -\frac{\hbar\Omega}{2}\left(e^{-i\phi}\hat{\sigma}^+ + e^{i\phi}\hat{\sigma}^-\right) \\
&= -\frac{\hbar\Omega}{2}\left(\cos(\phi)\hat{\sigma}_x - \sin(\phi)\hat{\sigma}_y\right).
\end{aligned} \tag{3.37}
$$

We can now see that in the Bloch sphere picture the drive causes the state vector to rotate around a horizontal axis while the angle of the axis is determined by the phase of the drive. To find the rotation frequency, we set $\phi = 0$, which results in the new propagator $\hat{U}'$:

$$
\begin{aligned}
\hat{U}' &= e^{-i\hat{H}'t/\hbar} \\
&= \begin{pmatrix} \cos\left(\Omega t/2\right) & -i\sin\left(\Omega t/2\right) \\ i\sin\left(\Omega t/2\right) & \cos\left(\Omega t/2\right) \end{pmatrix}.
\end{aligned} \tag{3.38}
$$

Starting with a qubit in its ground state, the state of the qubit at time t will be

$$
\hat{U}'\left|0\right\rangle = \cos\left(\frac{\Omega t}{2}\right)\left|0\right\rangle + i\sin\left(\frac{\Omega t}{2}\right)\left|1\right\rangle. \tag{3.39}
$$

A full cycle around the Bloch sphere is completed when $\Omega t = 2\pi$. Therefore, the rate of rotation is $\Omega/2\pi$, called the Rabi frequency.

Control pulses

As stated above, a sufficient anharmonicity is needed so that we can address the $\left|g\right\rangle \to \left|e\right\rangle$ transition without driving other ones. This is especially important when we want to drive the transition with short microwave pulses. These control pulses are typically shaped with a Gaussian envelope $g(t) = \exp\left((t - t_0)^2 / 2\sigma_t^2\right)$, where the width of the pulse is given by σ_t. Since the envelope never reaches zero, it is truncated at $\pm 6\sigma_t$. The spectrum of the untruncated pulse is given by its Fourier transform, which also has a Gaussian shape and a width of $2\pi\sigma_f = 1/\sigma_t$. The shorter the pulse, the wider its spectrum. This means that the anharmonicity sets a limit on how fast qubit operations can be performed. Therefore, α should be several times larger than σ_f. However, it should be noted that this limit can be overcome by using optimal control pulses with pulse shaping techniques such as DRAG [46], which use a wider spectrum to generate faster pulses and at the same time reduce the frequency components, which would drive transitions such as $\left|e\right\rangle \to \left|f\right\rangle$, where $\left|f\right\rangle$ is the second excited state of the qubit.
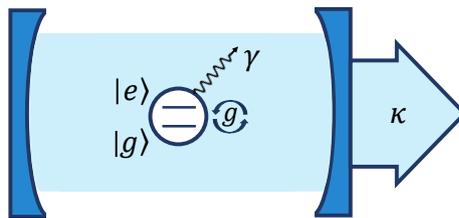
Figure 3.7: **A schematic representation of the interaction between an atom and a cavity.** The two-level system with its states $|g\rangle$ and $|e\rangle$ (white) interacts with the cavity mode (light blue) at a rate g by releasing or absorbing a photon γ. The cavity is depicted as two mirrors (blue). The decay rate κ accounts for the photon loss of the cavity.

3.2 Cavity QED

The transmon was originally developed as an integrated circuit on a substrate [22]. In that fashion, it is coupled to a planar coaxial transmission line, hence the name 2D transmon. Even till today, it is a central component of many scalable platforms and finds application in a variety of quantum information problems [15, 42, 47]. Putting scalability aside, for now, we can make further progress when coupling the qubit to a 3D cavity instead of a 2D transmission line. In this approach, we can still use microwave pulses to manipulate the qubit's state, but furthermore, we can make use of the long-lived 3D photon field inside the cavity.

To gain more insights about the coupling between the transmon and a cavity, which is schematically shown in Figure 3.7, we need to introduce the theory of cavity quantum electrodynamics. This theory describes the interaction between a single atom, which is treated as a two-level system and the photonic modes trapped inside a cavity. By shielding both the two-level system and the electromagnetic field from the noisy environment, the quantum behaviour and states can be precisely controlled, eventually using them for quantum computations.

One phenomenon arising in this setup is the so-called *Purcell effect* named after Edward Purcell, who proposed it in 1945 [48]. It states that the decay rate of a polarized nuclear spin can be increased by placing it inside a resonant cavity. Remarkably, the opposite also applies. When working with transmons, one uses the fact that in an off-resonant environment, the decay rate can drastically be reduced making lifetimes of 100 μs or longer possible. Without this inverse Purcell effect, an excitation of the transmon would decay within picoseconds because of its large dipole moment providing a relatively high coupling rate to the outside world.
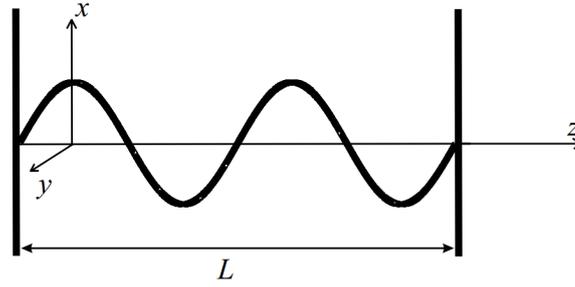
Figure 3.8: **A schematic representation of a cavity** with perfectly conducting walls at $z = 0$ and $z = L$. The electric field is polarized along the x-direction. Due to the boundary conditions, the electric field forms standing waves [49].

3.2.1 Quantization of a single-mode field

To gain a fundamental understanding of the behaviour of an electromagnetic field trapped inside a cavity, we will start by examining the energy spectrum of a radiation field confined in a one-dimensional cavity along the z-axis with perfectly conducting walls at $z = 0$ and $z = L$, as shown in Figure 3.8. For the derivation, we closely follow [49]. Since there are no sources of radiation inside the cavity, Maxwell's equations (in SI units) simplify to

$$\nabla \cdot \vec{B} = 0 \tag{3.40}$$

$$\nabla \cdot \vec{E} = 0 \tag{3.41}$$

$$\nabla \times \vec{E} = -\frac{\partial \vec{B}}{\partial t} \tag{3.42}$$

$$\nabla \times \vec{B} = \mu_0 \varepsilon_0 \frac{\partial \vec{E}}{\partial t}. \tag{3.43}$$

Because of the perfectly conducting walls, the electric field must vanish at the boundaries, thus becoming a standing wave. With the electric field polarized in the x-direction, a single-mode field is then given by

$$E_x(z, t) = \left(\frac{2\omega_m^2}{V \varepsilon_0} \right)^{1/2} q(t) \sin(kz) \tag{3.44}$$

$$B_y(z, t) = \left(\frac{\mu_0 \varepsilon_0}{k_m} \right) \left(\frac{2\omega_m^2}{V \varepsilon_0} \right)^{1/2} \dot{q}(t) \sin(kz), \tag{3.45}$$

where $\omega_m = c(m\pi/L)$, $m = 1, 2, ...$ are the allowed frequencies of the mode and $k_m = \omega_m/c$ is the wave number with the speed of light c. V represents the effective volume of the cavity and $q(t)$ is a time-dependent factor having the dimension of length. The Hamiltonian of an electromagnetic field is given by

$$H = \frac{1}{2} \int dV \left(\varepsilon_0 \vec{E}^2(\vec{r}, t) + \frac{1}{\mu_0} \vec{B}^2(\vec{r}, t) \right) \tag{3.46}$$

$$= \frac{1}{2} \int dV \left(\varepsilon_0 E_x^2(z, t) + \frac{1}{\mu_0} B_y^2(z, t) \right). \tag{3.47}$$

Using equations (3.44) and (3.45) the Hamiltonian reads

$$H = \frac{1}{2} \left(\dot{q}^2 + \omega_m^2 q^2 \right) = \frac{1}{2} \left(p^2 + \omega_m^2 q^2 \right), \tag{3.48}$$

where $\dot{q}(t) = p(t)$ plays the role of the canonical conjugate of $q(t)$. We see that the Hamiltonian of a single mode is formally equivalent to a harmonic oscillator. After using the correspondence rule to replace q and p by operators and introducing the creation and annihilation operators $\hat{a}^\dagger$ and $\hat{a}$ as in section 3.1.3, we arrive at the well-known

$$\hat{H} = \hbar\omega_m \left(\hat{a}^\dagger \hat{a} + \frac{1}{2} \right), \tag{3.49}$$

where $\hat{a}^\dagger \hat{a} = \hat{n}$ now gives the number of photons inside the cavity. The same Hamiltonian holds true even in the three-dimensional case, only the structure of the modes themselves becomes more complicated.

Microwave cavities as LC resonators

Another approach to see why cavities can be modelled as quantum harmonic oscillators is by imagining the walls of the cavity as a capacitor with charge Q containing an electromagnetic field, which meets the boundary conditions of the cavity. Therefore, a single mode can be interpreted as an excitation of an LC circuit with a resonance frequency $\omega_r = 1/\sqrt{LC}$ and the total energy is given by

$$\hat{H}_r = \frac{\hat{\Phi}}{2L} + \frac{\hat{Q}}{2C}, \tag{3.50}$$

and using the creation and annihilation operator as in chapter 3.1.3, this leads to

$$\hat{H}_r = \hbar\omega_r \left(\hat{a}^\dagger \hat{a} + \frac{1}{2} \right). \tag{3.51}$$

3.2.2 Driving the cavity

The cavity as a harmonic oscillator coupled to a transmon inherits only a very small nonlinearity from the qubit (in the kHz range), so we cannot address the single energy eigenstates by applying a classical drive. With this method, we will excite the harmonic oscillator into one of its coherent states with a certain amplitude and phase [49]. Unlike Fock states, they have some instantaneous mean electric and magnetic field and also have minimal and symmetric uncertainty. The position of such a state in phase space can be described by a complex number α. In the case of a fully harmonic oscillator, these even evolve in a classical fashion by following a circular trajectory in phase space.

To reach a coherent state, we apply a classical electric field H_{field} to the vacuum Fock state of the harmonic oscillator, which is also the coherent state $|\alpha = 0\rangle$:

$$H_{\text{field}} = \xi^\star a + \xi a^\dagger \to D(\alpha) = \exp\left(\alpha^\star a - \alpha a^\dagger\right), \tag{3.52}$$

where H_{field} can also be written as the displacement operator $D(\alpha)$, which takes any coherent state from $|\alpha_0\rangle$ to $|\alpha_0 + \alpha\rangle$. In the Fock basis, these coherent states can be described as an infinite superposition of Fock states weighted by a Poisson distribution:

$$|\alpha\rangle = e^{-|\alpha|^2/2} \sum_{n=0}^{\infty} \frac{\alpha^n}{\sqrt{n!}} |n\rangle. \tag{3.53}$$

3.2.3 Quality factors and loss mechanisms

Now that we know how to control a cavity, we need a measure for how well a cavity is suited as a quantum state memory. Here, the quality factor Q of a resonator can be used since it is a measure for the resonator's ability to maintain an excitation within it. In general, it is defined as the losses per cycle compared to the total stored energy E_{tot} [50]:

$$Q \equiv \omega_{\text{r}} \frac{E_{\text{tot}}}{P_{\text{tot}}} = \omega_{\text{r}} T_1 = \frac{\omega_{\text{r}}}{\kappa}, \tag{3.54}$$

where P_{tot} is the total dissipated power. ω_{r} is the resonance frequency of the resonator and T_1 is its energy decay time, which is inversely related to the energy decay rate κ.

For our purposes, we are calling the quality factor of the system loaded quality factor Q_{l} which has two contributions:

$$\frac{1}{Q_{\text{l}}} = \frac{1}{Q_{\text{i}}} + \frac{1}{Q_{\text{c}}} \tag{3.55}$$

with the internal quality factor Q_i, which accounts for the internal losses of the cavity, and the coupling quality factor Q_c, which contains the external losses due to the measurement apparatus. We are going to explore the most important loss mechanisms and their effect on the design of the cavity.

External losses

The external losses are a direct consequence of coupling signal into and out of the resonator. The mode will be damped at a rate, which depends on the real part of the ports admittance and the energy will be dissipated externally. This can be used for readout purposes, as a lower quality factor leads to a strong damping of the mode and therefore to a fast readout. On the other hand, a cavity used for storing a quantum state should be coupled as weakly as possible to an output transmission line.

Internal losses

The internal losses can be divided into dielectric losses, conductor losses, and contact resistance. *Dielectric losses* account for the energy of the mode's electric and magnetic field that is dissipated on the surface of the superconducting metal, e.g., in an oxide layer AlO_x, and on the surface of the substrate, which holds the transmon. Moreover, the dissipation can also take place within the substrate. Although the surface layer has a relatively small volume, its losses dominate the overall losses. Therefore, it is beneficial to store as much energy as possible in the bulk sapphire, which can be done by moving from 2D to 3D transmons. Further, to decrease dielectric losses, we are going to remove the oxide layer of the cavity's surface.

Conductor losses only contribute a small fraction to the total losses of the system since the resonators used in this thesis are made of high purity aluminum and are operated within the superconducting regime (<1.1 K). Nonetheless, the resonators have a finite temperature and therefore contain non-equilibrium quasiparticles [51–53] and have some finite conductivity.

Contact resistance arises at the connections between components because any three-dimensional cavity needs to be assembled from at least two parts. Therefore, cavity joints should be located in regions with the smallest current density and magnetic field across the seam possible. This decisive criterion will lead to the special design of the cavity, which will be introduced in Chapter 4.

3.3 Coupling a transmon to a resonator

So far, we have elaborated on the underlying physics of transmons and cavities. Now we want to bring both parts together and examine the system as a whole. To get a clear picture of how the system's parts will interact with each other, let us first have a look at the equivalent circuit in
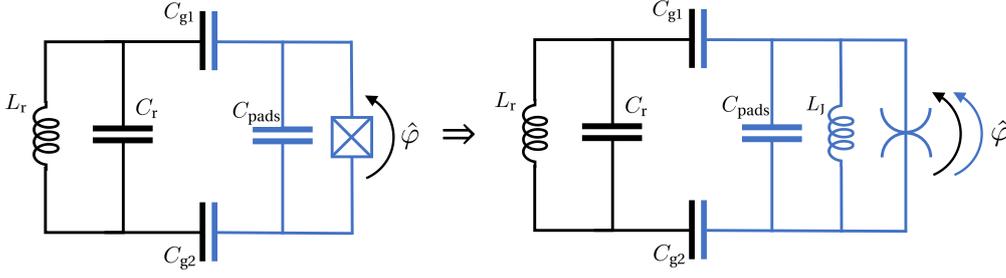
Figure 3.9: **Decomposition of a transmon into its linear and nonlinear part.**
After the decomposition, the higher-order terms are accounted for by the spider
element, depicted as the most right-hand circuit element. Both resonators now
contribute to the flux φ across the junction.

Figure 3.9. The circuit consists of a transmon and a cavity. The qubit is coupled to the rest of the
circuit via its large antennas, which can be modelled as the two coupling capacitors C_{g1} and
C_{g2}. Therefore, it can interact with the cavity, shown as an LC circuit with a capacitance C_r and
an inductance L_r, and the drive V_g.

For the analysis of the coupled system, we will treat the transmon as an anharmonic oscil-
lator. This can be done by rearranging Equation (3.20) and neglecting the offset charge n_g. To
separate the harmonic part from the rest of the transmon Hamiltonian $\hat{H}_t$, we are expanding
the cosine and combining the quadratic terms. As shown on the right-hand side in Figure 3.9,
this corresponds to the decomposition of the transmon into a linear LC circuit with some higher
order perturbation represented by the spider element:

$$\hat{H}_t = 4E_C\hat{n}^2 + \frac{E_J}{2}\hat{\Phi}^2 - E_J\left(\cos(\hat{\Phi}) - \frac{\Phi^2}{2}\right). \tag{3.56}$$

In general, the transmon can be coupled to multiple cavities, hence, we start by diagonalizing n
coupled harmonic oscillators and end up with a linear Hamiltonian $\hat{H}_{lin}$ of the form

$$\hat{H} = \hbar\sum_n \tilde{\omega}_n \hat{a}_n^\dagger \hat{a}_n, \tag{3.57}$$

where $\hat{a}_n$ represents the annihilation operator of the re-diagonalized n-th mode. As shown in
Figure 3.9, each mode will contribute to some amount of flux across the junction

$$\hat{\Phi} = \sum_n \Phi_n^{ZPF}\left(\hat{a}_n^\dagger + \hat{a}_n\right). \tag{3.58}$$

In Section 3.1.3 we have already seen that we can relate the zero-point fluctuations to the
effective admittance $Y(\omega)$ of the circuit using Equation (3.9) and $Y(\omega) = 1/Z(\omega)$.
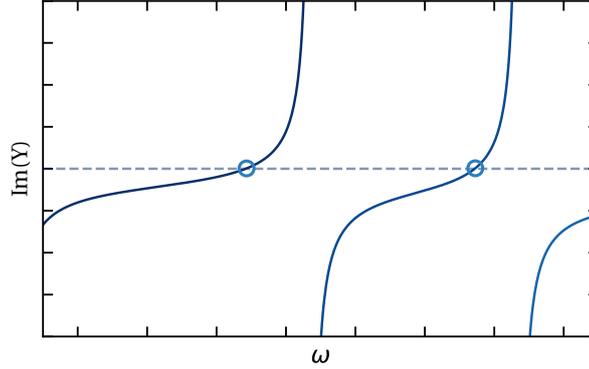
Figure 3.10: **A typical trace for $Y(\omega)$ as seen from the junction.** One can find the participation of a mode in the junction's nonlinearity by using the zero-crossings of the imaginary part of $Y(\omega)$ and the slope at that points.

Since $Y(\omega)$ is a classical circuit parameter, we can use traditional circuit simulators to predict Φ_n^{ZPF}. To determine the admittance of each mode, we have to calculate the circuit's impedance from the junction's point of view across a wide range of frequencies. Since our cavity-transmon system is three-dimensional, we are going to use a finite element solver to calculate the admittance. This will be explained in detail in the next chapter. A typical trace for the imaginary part of $Y(\omega)$ is shown in Figure 3.10. We find the normal modes of the circuit at $Y(\tilde{\omega}_n) = 0$. Moreover, the slope of $Y(\omega)$ at $\omega = \tilde{\omega}_{\text{n}}$ is related to the mode's effective characteristic impedance as

$$Y_n' \equiv \left(\frac{\mathrm{d}Y}{\mathrm{d}\omega}\right)\bigg|_{\omega=\tilde{\omega}_n} = \frac{2i}{\tilde{\omega}_n Z_{\text{eff},n}}. \tag{3.59}$$

The magnitude of the zero-point fluctuations is then given by [54]

$$\Phi_{\text{ZPF}}^n = \sqrt{\frac{\hbar}{2}\frac{1}{\tilde{\omega}_n Y_n'}}. \tag{3.60}$$

To proceed, we write the whole Hamiltonian as

$$\hat{H} = \hbar \sum_n \tilde{\omega}_n \hat{a}_n^\dagger \hat{a}_n + \hat{H}_{\text{nl}}, \tag{3.61}$$

where $\hat{H}_{\text{nl}}$ is the higher order perturbation from Equation (3.56), except the simple flux operator is replaced by the total flux across the junction:

$$\hat{H}_{\text{nl}} = -E_{\text{J}} \left(\cos\left(\sum_n \frac{\Phi_n^{\text{ZPF}}}{\Phi_0}\left(\hat{a}_n^\dagger + \hat{a}_n\right)\right) - \frac{1}{2}\left(\sum_n \frac{\Phi_n^{\text{ZPF}}}{\Phi_0}\left(\hat{a}_n^\dagger + \hat{a}_n\right)\right)^2 \right). \tag{3.62}$$

The full Hamiltonian now corresponds to a transmon coupled to multiple resonator modes. We are going to examine the case of three modes in more detail since this corresponds to the setup, which we are using for the experiments later. To gain useful insights about the interaction between the different resonators, we are Taylor expanding the full Hamiltonian and truncating it at the fourth order. This results in

$$\hat{H} \approx \frac{\hbar E_{\mathrm{J}}}{24} \left(\varphi_{\mathrm{a}} \left(\hat{a}^{\dagger} + \hat{a} \right) + \varphi_{\mathrm{b}} \left(\hat{b}^{\dagger} + \hat{b} \right) + \varphi_{\mathrm{c}} \left(\hat{c}^{\dagger} + \hat{c} \right) \right)^4 , \tag{3.63}$$

where $\varphi_{\mathrm{n}} = \frac{\Phi_n^{\mathrm{ZPF}}}{\Phi_0}$. After using the rotating wave approximation and keeping all the non-rotating terms up to 4th order, the Hamiltonian reads

$$\begin{aligned} \hat{H}/\hbar \approx\; & \tilde{\omega}_{\mathrm{a}} \hat{a}^{\dagger}\hat{a} + \tilde{\omega}_{\mathrm{b}} \hat{b}^{\dagger}\hat{b} + \tilde{\omega}_{\mathrm{c}} \hat{c}^{\dagger}\hat{c} \\ & - \chi_{\mathrm{ab}} \hat{a}^{\dagger}\hat{a}\hat{b}^{\dagger}\hat{b} - \chi_{\mathrm{bc}} \hat{b}^{\dagger}\hat{b}\hat{c}^{\dagger}\hat{c} - \chi_{\mathrm{ca}} \hat{c}^{\dagger}\hat{c}\hat{a}^{\dagger}\hat{a} \\ & - \frac{K_{\mathrm{a}}}{2} \hat{a}^{\dagger}\hat{a}^{\dagger}\hat{a}\hat{a} - \frac{K_{\mathrm{b}}}{2} \hat{b}^{\dagger}\hat{b}^{\dagger}\hat{b}\hat{b} - \frac{K_{\mathrm{c}}}{2} \hat{c}^{\dagger}\hat{c}^{\dagger}\hat{c}\hat{c}, \end{aligned} \tag{3.64}$$

where $\tilde{\omega}_i$ are the renormalized resonance frequencies of the modes due to hybridisation. These frequencies are related to the bare resonance frequencies ω_k via [55]

$$\begin{aligned} \tilde{\omega}_k =\; & \omega_k + \chi_{01} \\ =\; & \omega_k + \frac{g^2}{\Delta}, \end{aligned} \tag{3.65}$$

where g is the coupling strength between the qubit and the cavities and $\Delta = \omega_i - \omega_{\mathrm{ge}}$. χ_{01} is, therefore, the shift of the cavity frequency with the qubit in its ground state. Note that this shift can be positive or negative, depending on whether the qubit frequency is above or below the cavity frequency. χ_{ij} denotes the dispersive coupling strength between the modes $\hat{i}$ and $\hat{j}$. K_i are the self-Kerr coefficients for the mode $\hat{i}$. These are equal to the anharmonicity of a mode and are for a transmon typically denoted with α. Interestingly, even though we began with only one nonlinear resonator, the other ones also inherited a small part of the nonlinearity. The transmon is the most nonlinear part of the system with $\alpha > 100\,\mathrm{MHz}$, and the coupled resonators have self-Kerr coefficients of $K_i \approx 1\text{-}10\,\mathrm{kHz}$. In this 4th order approximation, we can relate the self-Kerr coefficients to the mode's effective characteristic impedance as

$$K_i = \frac{e^2}{2\hbar} \frac{1}{L_0} \cdot Z_{\mathrm{eff,i}}^2 . \tag{3.66}$$

Moreover, in the second line of Equation (3.64) we also find terms that correspond to a cross-Kerr type nonlinearity. The cross-Kerr interaction strength related to the self-Kerr terms as

$$\chi_{ij} = -2\sqrt{K_i K_j}. \tag{3.67}$$

If our system consists of modes with a large detuning, χ_{ij} is the dominant coupling term. We call this regime the dispersive regime. Looking at Equation (3.64) again, if mode $\hat{a}$ has been excited to the first Fock state, the resonance frequency of mode $\hat{b}$ and $\hat{c}$ will be decreased by χ_{ab} and χ_{ca}, respectively, called the dispersive shift or AC-Stark shift, in case the cavity is shifted, or Lamb shift, in case the qubit is shifted. When the dispersive shift is much larger than the linewidth of the modes, the so-called strong dispersive regime, we can detect the state of the transmon by determining the resonance frequency of one of the coupled resonators. Additionally, this phenomenon could also be used, for example, to perform conditional gates on a resonator mode controlled by the state of the transmon.

Number splitting

The inherited nonlinearity of the cavities is small enough that classical drives will displace the cavity mode to a coherent state and therefore create a superposition of Fock states or number of photons inside the cavity. Probing the resonance frequency of the qubit while the cavity mode is in a coherent state will cause the qubit transition frequency to be split into a superposition of many frequencies, which are all separated by the dispersive shift (Equation (3.64)). This phenomenon is called number splitting [56] and can conveniently be used to perform number-selective pulses on the qubit entangling it with the number state of the cavity. Utilizing this method, one can even create Fock states of the photon field inside the cavity only using classical drives on the cavity and the transmon.

Purcell effect

For the optimization of the readout process, it would appear natural to increase the coupling between the qubit and the cavity as far as possible to improve the signal amplitude and readout speed. However, for our qubit, this would enhance the decay channel into the resonator modes, which is given by the Purcell rate γ_{Purcell} as

$$\gamma_{\text{Purcell}} \approx \kappa_{\text{r}} \left(\frac{g}{\Delta} \right)^2, \tag{3.68}$$

where κ_{r} is the decay rate of the cavity's resonance mode into the transmission line. The inverse Purcell rate can be seen as an upper limit to the qubit lifetime T_1^{max}.

High-power readout of the qubit state

Now that we know that the cavity becomes nonlinear in the presences of a qubit, we can think of another way to read out the state of a far detuned qubit besides the dispersive readout. The idea is to probe the cavity at its bare resonance frequency ω_{r} with high power (tens of thousands

of photons). When exceeding the critical n_{crit}, the cavity's response becomes highly nonlinear, and the dispersive Hamiltonian approximation no longer holds. n_{crit} is given by

$$n_{\text{crit}} = \frac{\Delta^2}{4g^2}. \tag{3.69}$$

For $n_{\text{ph}} > n_{\text{crit}}$, the resonance frequency shifts down to the cavity's bare frequency, i.e., the frequency not affected by the dressing of the qubit [57]. This is because a large number of photons will drive a current above the junction's critical current I_{c}, which results in a breakdown of the superconductivity and the nonlinearity.

Now we can make use of the fact that this critical power highly depends on the state of the qubit meaning that the bare state can already be entered for a lower probe power if the qubit is in its excited state. Therefore, we can record a spectrum at ω_{r} with a power that is slightly below the critical power. A peak will only appear if the qubit is in the excited state.

One of the advantages of this readout technique is a better signal-to-noise ratio and a higher fidelity since the lifetime of the qubit is limiting the integration time of the dispersive readout. However, this readout scheme is non-QND, hence the quantum state is disrupted during the measurement, meaning that the measurement is not simply projecting the state onto the measurement basis. Especially, when the qubit is in the excited state, this measurement will cause it to leave our computational basis, and we will have to wait until it decays back into its ground state.

4 Design of the three-mode cavity-transmon system

In this chapter, the main components of the experimental setup are presented: the coaxial $\lambda/4$ resonator and the transmon. To design a system, which is capable of storing a quantum state, one needs at least two more resonators besides the qubit, one for the readout of the transmon and a second one for the storage of the quantum state. For this purpose, we decided to use two coaxial $\lambda/4$ resonators, which are fabricated such that they are in close proximity to each other. This design allows the two cavities to be connected via the transmon, which will be located in between them.

In the following sections, it is shown how the cavities and the transmon were designed and why we have decided on our device parameters. For the cavities, the requirements are high quality factors and a sufficient coupling strength to the transmon, whereas the transmon has to be designed with the anharmonicity and charge dispersion in mind.

4.1 Development of the cavity resonator

To achieve the highest possible quality factors, the cavity resonators need to be optimized to reduce the energy dissipation mechanisms. Much optimization can be done by choosing a beneficial geometry for the cavity, which reduces contact resistance. There is one resonator design, which really stands out by reaching extremely high quality factors while still being easy to fabricate: the coaxial $\lambda/4$ resonator. It was developed by the group of Robert J. Schoelkopf at the Departments of Applied Physics of Yale University [17] and is used in the cavity setup in this thesis.

The cavity's structure can be seen in Figure 4.1. It has a cylindrical shape with a pin reaching into the cavity from the bottom. The upper part of the cavity above the pin can be seen as a circular waveguide with length L. When introducing a voltage difference between the cavity walls and the pin in the middle, the lower part of the resonator resembles a transmission line. The line is short-circuited on the bottom and has an open end on the top. In case of perfectly conducting cavity walls, these boundary conditions force the electric field between the pin and the wall to vanish at the bottom and to have a maximum at the top of the pin. Therefore, the resonance frequencies of the cavity are discretized to $l = (2n+1) \cdot \frac{\lambda}{4}$ with $n = 0,1,2,...$ and the fundamental mode being $l \approx \lambda/4$.

The next mode for the transmission line has a frequency of $f_1 \approx 3\lambda/4$. Therefore, we can be sure that we are only exciting the fundamental mode without addressing other ones when sending in a microwave signal.
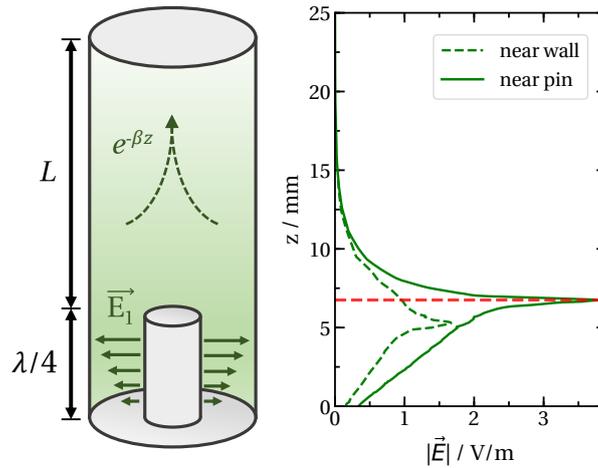
Figure 4.1: **A schematic representation of the $\lambda/4$ resonator and a numerical simulation of its electric field distribution.** The arrows indicate the strength of the electric field of the fundamental mode. As we can see on the right-hand side, the electric field reaches its maximum slightly below the end of the pin (red dashed line), especially when moving closer to the cavity walls. Above the pin, we can also see the decay of the mode into the circular waveguide.

The electric field concentrates around the top of the pin and decays into the waveguide section of the cavity. What differentiates waveguides from cavities is that they are much longer than the wavelengths of the modes it is supposed to carry. (In theory, waveguides are infinitely long.) Under these conditions, the waveguide can only transmit modes with a frequency higher than its cutoff frequency f_c, which for a circular cross section is given by

$$f_c = p_{1,1} \frac{c}{2\pi r}, \tag{4.1}$$

where $p_{1,1}$ is the first root of the first Bessel function and r is the radius of the waveguide. Modes below the cutoff frequency will be damped exponentially.

Calculating the resonance frequency of the cavity

Calculating the exact resonance frequency of a $\lambda/4$ resonator by hand would be a tedious thing to do since one would have to determine the capacitance and inductance of such complex geometry. Luckily, we have access to a fully three-dimensional finite element solver called HFSS (High-Frequency Structure Simulator) by ANSYS, which can calculate the eigenmodes of a given geometry for us. In the simulation, the walls of the cavities were modelled as perfect electric conductors assuming that the loss is dominated by the coupling to the transmission line, which was also included in the simulation.
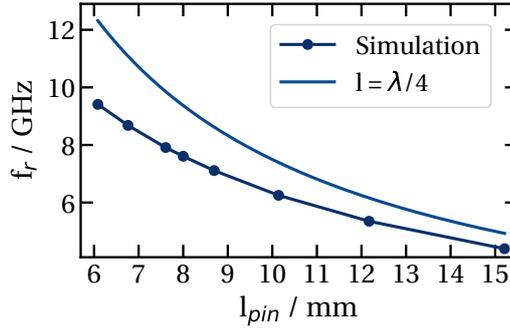
Figure 4.2: **Length of the cavity pin versus its resonance frequency.** As expected, f_r is inversely proportional to l_pin. However, looking at the simulated point, the wavelength appears to be shorter than $l \approx \lambda/4$. This is due to the spatial distribution of the electric field, which extends beyond the top of the pin adding an effective shunt capacitance.

The first thing to note is that the simulations have shown that $l < \lambda/4$, which can be seen in Figure 4.2. This can be explained by the fact that the electric field does not abruptly go to zero at the end of the stub but is effectively spread over a larger region than $\lambda/4$. For a cavity with a resonance frequency of 7.6 GHz, we calculate $l_\mathrm{eff} \approx 1.23 \cdot l_\mathrm{pin}$.

To get a better feel for the distribution of the electric field, we can have a look at the magnitude of the electric field $|\mathbf{E}|$ on a vertical line close to the pin and close to the walls of the cavity, which is shown in Figure 4.1. We can see that for small values of z, the electric field increases linearly. When reaching the tip of the pin, $|\mathbf{E}|$ increases dramatically, which is due to the abrupt ending of the pin leaving sharp edges where the electric field is concentrated. For $z > l_\mathrm{pin}$, $|\mathbf{E}|$ decreases exponentially. We see that a significant portion of the electric field is located inside the waveguide, which adds a shunt capacitance. This is effectively elongating the pin, causing $l < \lambda/4$. Moreover, the maximum moves towards the bottom of the cavity as we probe it closer to the cavity wall. We will use this fact to ensure a strong coupling between the transmon and the cavity since we want to maximize the overlap of the transmon's dipole moment and the electric field.

Additionally, one has to be aware of the fact that inserting the transmon into the cavity will further reduce its resonance frequency. This is because the transmon is evaporated onto a sapphire substrate, which effectively elongates the electric field due to its high dielectric constant of $\epsilon_\mathrm{sapphire} = 8.90\text{–}11.11$ [58].

The distribution of the electric field also reveals the advantage of this type of resonator. Due to the vanishingly small electric field strength at the top of the cavity, we can drastically reduce seam losses, which would occur at the seams between the cavity and a lid that closes the waveguide. To achieve the desired reduction of seam losses, the circular waveguide has to be designed such that the resonance frequency of the cavity f_0 is well below the waveguide's cutoff

frequency f_c. In this configuration, the fundamental mode of the resonator is a TEM mode in the coaxial region and the decaying TM modes in the circular waveguide. Since the TM_{01} mode is the one with the lowest cutoff frequency, it dominates the transport of our signals and is given by the fields (in cylindrical coordinates) [59]

$$\mathbf{E} = \frac{V_0 e^{-\beta z}}{\rho \ln(b/a)} \boldsymbol{\rho} \tag{4.2}$$

$$\mathbf{H} = \frac{V_0 e^{-\beta z}}{2\pi\eta\rho} \boldsymbol{\phi}, \tag{4.3}$$

where a is the radius of the inner and b the radius of the outer conductors. V_0 is the voltage on the transmission line, $\eta = \sqrt{\frac{\mu_0\mu_r}{\epsilon_0\epsilon_r}}$ is the ratio between the electric and magnetic field, and β the damping constant of the fields propagating into the waveguide. To simplify the manufacturing process of the cavity and because of the limited space in the dilution refrigerator, we chose $a = 1.75$ cm and $b = 5.25$ cm since this ratio of 3:1 works best for minimizing the losses from surface resistance by advantageously shaping the electric field distribution [45].

To ensure that the damping of the mode in the z-direction is sufficient by choosing a large enough L, we first have to decide for the frequencies of the two cavities since the damping parameter will depend on the resonance frequency.

Cavity-transmon system

We decided for the setup, which can be seen in Figure 4.3: The two cavities are in close proximity and aligned such that the top of their pins are at the same level. Consequently, the maxima of the electric fields are approximately on the same hight, which is convenient since we want the couple a transmon to both modes. The two resonators are joint together via a small tunnel, in which the transmon will be placed. The antennas of the transmon are then able to reach into both cavities.

This general design is then adjusted to meet the following parameter requirements: The first cavity, from now on called storage cavity, should have a relatively low resonance frequency of $\omega_s/2\pi = 4$–5 GHz. By choosing a low frequency, we can reduce the energy decay rate κ_s of the cavity, as can be seen in equation (3.54). The resonance frequency of the second cavity, called readout cavity, can be higher, but should not be at multiples of $j\omega_s/2\pi \pm k\chi_s \pm l\chi_r$ for $j, k, l = 1,2,...$ since we do not want uncontrolled two-photon processes to exchange excitations between the cavities. Moreover, the frequency of the output signal of the readout cavity needs to be optimized so that it can be amplified by a Josephson parametric converter (JPC). Our JPC model operates in a frequency range between 8.6 GHz and 9 GHz constraining the frequency of the fundamental mode of this cavity to be within that range. For the experiment, we decided to
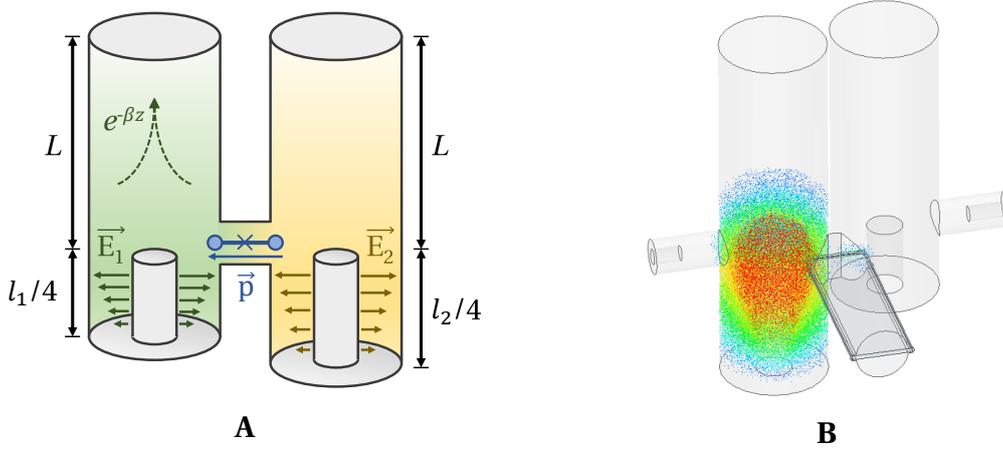
Figure 4.3: **The cavity-transmon system. A** A schematic representation of the cavity-transmon system. It consists of two $\lambda/4$ resonators, one intended for the storage (yellow) and one for the readout (green) of the state. The arrows around the pin indicate the strength of the electric field of the fundamental mode. The dipole moment $\vec{p}$ of the transmon (blue) is approximately parallel to the electric field. **B** The electric field distribution of the fundamental mode in one cavity. The electric field extends beyond the pin and into the circular waveguide above. The other waveguides connected to the cavity, i.e., the coupling port to the transmission line and the hole, through which the transmon can enter, are even smaller in diameter and, therefore, attenuate the electric field strongly confining it inside the cavity.

use a 6.75 mm long pin for the storage cavity and a 14.4 mm long one for the readout resonator resulting in a resonance frequency of 4.634(1) GHz and 8.778(1) GHz, respectively.

To determine the required length of the waveguide section above the pin, we have to calculate the propagation constants $\beta_{\text{TM}_{0n}}$ for the TM_{0n} modes, which are given by [59]

$$\beta_{\text{TM}_{0n}} = \sqrt{\left(\frac{2\pi f_0}{c}\right)^2 - \left(\frac{p_{0n}}{b}\right)^2}, \tag{4.4}$$

where p_{0n} is the n-th root of the zeroth Bessel function $J_0(x)$. We can neglect the propagation through the TE modes even though the TE_{11} has the lowest cutoff frequency since these modes are symmetrically unfavourable to be excited in our geometry. For $f_0 < \frac{p_{0n}c}{2\pi b}$ the propagation constant becomes imaginary and thus corresponds to a damping of the field. To determine the proper length of the waveguide, we only have to do the calculations for the readout cavity since lower frequencies will be damped even more efficiently. The propagation constants for the lowest three sub-cutoff modes for the configuration of $b = 5.25$ cm, which was used in the experiment, and the frequency $f_{\text{readout}} = 8.778$ GHz are listed in Table 4.1.

Table 4.1: **The propagation constants of the lowest three sub-cutoff TM modes** in the circular waveguide part of the cavity. The TM_{01} mode has the lowest frequency and is attenuated more strongly than the higher modes.

Mode	$|\beta|^{-1}$ / mm
TM_{01}	2.37
TM_{02}	0.97
TM_{03}	0.61

Since multiple TM modes are contributing to the energy transport, we are using HFSS to extract an effective propagation constant of $|\beta_{eff}|^{-1} = 2.16$ mm. Since the current-energy density falls as $|H|^2 \propto e^{-2|\beta_{eff}|z}$ we are expecting an attenuation of about e^{-20} at a waveguide length of $L_{min} \approx 10/|\beta_{eff}|$, which is more than sufficient to eliminate seam losses. Since in our case $L_{min} = 21.6$ mm, the two cavities are designed such that the circular waveguide part has a length of 30 mm. This would also make sure that the lower TM_{11} mode is attenuated sufficiently, in case the pin of the cavity is not perfectly symmetric.

Coupling to the environment

The cavity is coupled to the environment via a coaxial pin coupler. As shown in Figure 4.4, this coupler is located inside a hole in the cavity's sidewall. The z-location of the holes center is chosen to be slightly below the end of the stub since the electric field shows its maximum in this region, which would allow for a fast readout if needed. A coaxial transmission line carries the signals from the devices at room temperature to the pin coupler. At the end of the pin, there is, just like in the cavity itself, an abrupt change between the transmission line and a short circular waveguide (in the millimeter range) with a radius of $r_c = 1.78$ mm. Since the cutoff frequency of this waveguide is far above the signals sent to the cavity, the electric field is attenuated exponentially. This means that by varying the length of the pin and therefore the attenuation factor one can set the coupling of the cavity to the port and with it the coupling quality factor Q_c

$$Q_c \propto e^{2|\beta|l_c}, \tag{4.5}$$

where l_c corresponds to the length of the coupling waveguide and β is the propagation constant of the incoming mode. So in practice, the cavity for storing quantum information should be coupled via a short pin leaving a longer waveguide section, thereby strongly under-coupling it at the levels of $\kappa_{ext}/2\pi \approx 1$ kHz, while the one for the readout cavity should almost enter it
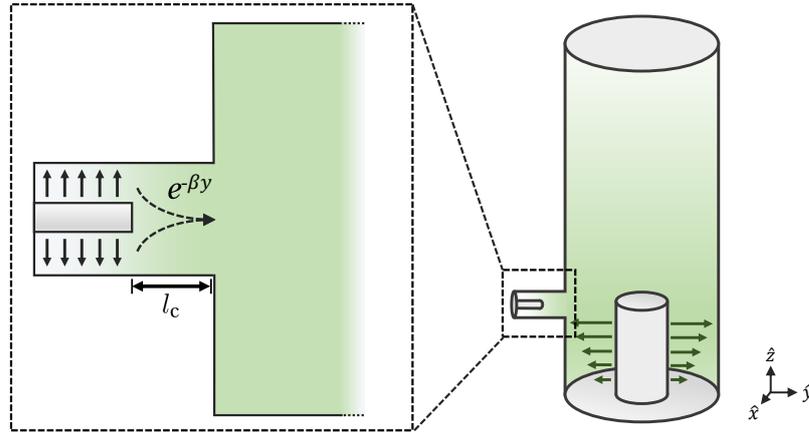
Figure 4.4: **A simplified picture of the electric field entering the cavity via a coupler pin.** Similarly to the cavity, the port also acts as a waveguide with length l_c connected to the coaxial line. Therefore, the coupling quality factor can be set by varying the length of the waveguide l_c.

strongly over-coupling it at rates of $\kappa_{\text{ext}}/2\pi \approx 1$ MHz. In the under-couple case, the losses are dominated by internal losses in the cavity. In the over-coupled case, losses are mostly due to dissipation in the transmission line.

4.2 Introducing the transmon to the cavities

With the two coaxial cavities in place, the next step is to find a way to introduce a transmon to the system. As we will see in the next few sections, there are two major challenges: Firstly, the transmon needs to be coupled strongly to both of the cavities simultaneously, and secondly, one has to be able to position the transmon inside the device with the best possible precision since slight deviations of a tenth of a millimeter can cause shifts in the Hamiltonian parameters, especially in the state-dependent dispersive shift.

To solve the first problem, we have to ensure a preferably large overlap between the electric field of the cavity modes and the dipole moment of the transmon. In principle, this could be done by extending the transmon antennas to reach into both cavities. However, we have to keep one limitation in mind, which is E_C of the qubit. Longer antennas are accompanied by a higher capacitance between the transmon and the walls of the cavity, meaning a lower E_C and a reduced anharmonicity. This would cause two additional problems. On the one hand, if the anharmonicity gets too low, we cannot use the transmon as a two-level system, and on the other, a reduced anharmonicity would also lead to a smaller dispersive shift making it more challenging to read out the qubit state with fast control pulses.
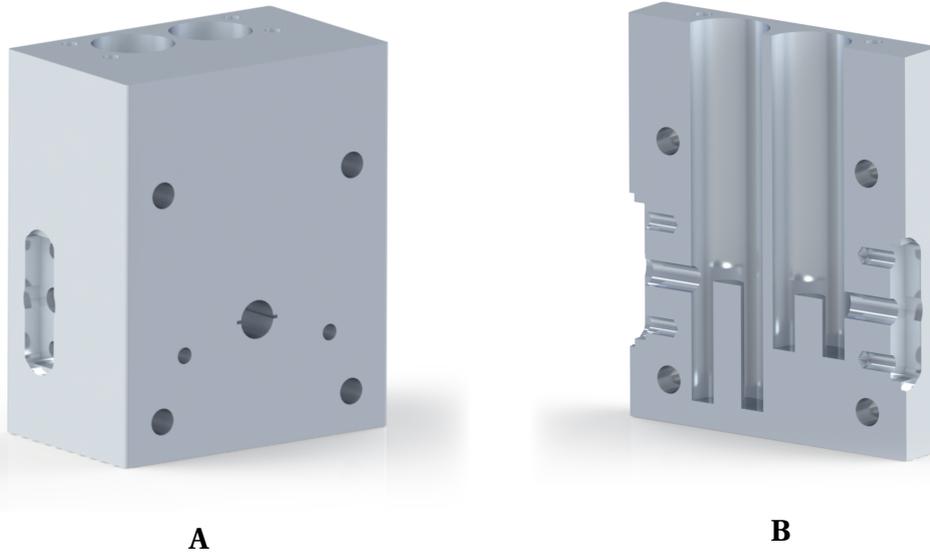
Figure 4.5: **Three-dimensional rendering of the cavity system. A** On the top, one can see two holes, which are the cavities themselves. In the front, we can find the center hole, where the sapphire chip with the transmon will be inserted. **B** The cross section of the cavity system. The front part of the aluminum block is cut out to show the inside of the system. On the left- and the right-hand side we can see the circular waveguides, which will be used to control the coupling to the transmission line.

These requirements give rise to problem number two regarding the positioning of the qubit. We have to ensure that the transmon antennas are far from the cavity walls. However, the only way to precisely park the chip is by lining it up to the walls.

To find a solution for this optimization problem, we start with the general geometry as presented in figure 4.5. As one can see, the system consists of the two cavities (vertical holes) with the pins at the bottom, which makes up the coaxial part of the cavity. On the left- and right-hand side of the block we can find the smaller circular waveguides, with will later house the SMA pins to drive the cavity field and the qubit. Towards the front, we can spot a horizontal hole, which is deep enough to enter both cavities, which can be seen in Figure 4.6 A. This will be the hole, in which the sapphire chip with the transmon on top will be inserted. To position the chip as precisely as possible, the waveguide's diameter is slightly smaller than the width of the chip, while leaving a slit in the wall of the hole. This is used as a guide when inserting the sapphire. The chip can then be pushed in until it reaches the middle wall between the two cavities. Given this setup and geometry, one can now vary many parameters to obtain the desired system Hamiltonian. Of course, with the length of the cavity pins, the fundamental frequencies of the cavities are changing. The coupling quality factor of the cavities depends not only on how far the SMA pins will be inserted into the small waveguides but also on their position relative to the

A

B
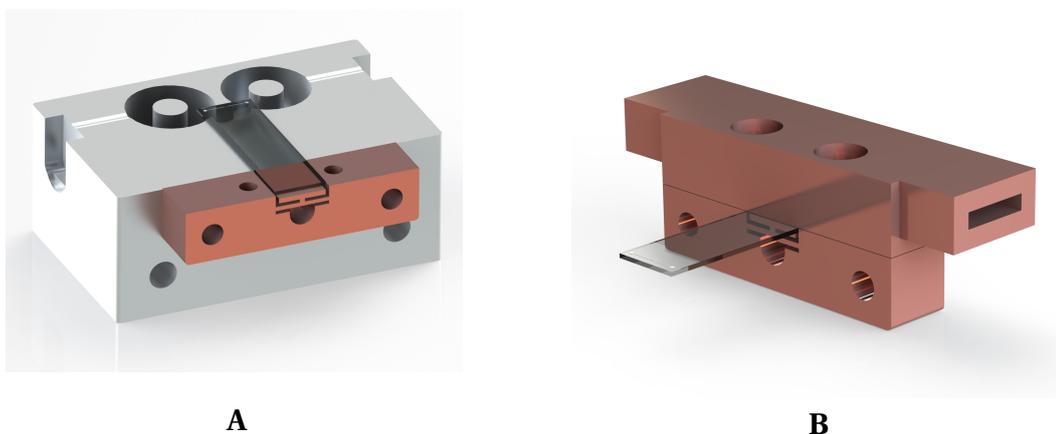
Figure 4.6: **Positioning of the transmon inside the cavity system. A** Rendering of the cut system. One can see how deep the sapphire chip is inserted so that the transmon can reach into both cavities. Two screws are used to secure the position of the clamp. **B** Rendering of the clamp holding the sapphire chip. It is used to hold the sapphire in place while ensuring a sufficient cooling of the chip. On the front end of the chip, the transmon can be seen.

cavity pin. The strongest coupling will be achieved when they are placed at the height where the electric field amplitude is the strongest. Important parameters are the ones, which change the coupling of the transmon to each cavity and the transmon's anharmonicity. To vary the coupling of the qubit to one of the cavities, we can either move it closer towards one of the cavity centers or move the chip up or down in z-direction. Here we make use of the fact that the electric field amplitude is highly dependent on the z-position of the qubit.

The exact parameters, such as how far the transmon has to be inserted, will be explored in the next section since these depend on the transmon geometry itself.

4.3 Finding a suitable transmon geometry

The design of the transmon used in this thesis was inspired by the latest developments of the 3D transmon. 3D transmons consist of two large antenna pads linked by one or even two Josephson junctions, which would make their resonance frequencies flux tunable. By using large antenna pads constructing a large dipole moment, one achieves a strong coupling between the transmon and the electric field inside a cavity. However, in contrast to the 3D transmons often used in rectangular cavities much larger than the transmon itself, our transmon is positioned close to the cavity walls. This results in a reduced E_C and therefore in a smaller anharmonicity. Hence, we face the challenge of reducing the area of the antenna pads to achieve the desired anharmonicity of 100–200 MHz, while maintaining a sufficient coupling to the electric field inside both cavities.

To meet the two requirements, one can, first of all, optimize the system's geometry before taking care of the transmon antennas. We know that the electric field of the cavity is the strongest slightly below the top of the cavity pin and gets stronger, the closer we move towards the cavity's center. That means, we can reduce the length of the antenna by moving the cavities together as close as possible. The lower limit of space between the cavities is set by the manufacturing techniques and is chosen to be 1.4 mm.

Another parameter that can be determined right away is the diameter of the hole, which will house the sapphire chip. Since the transmon needs to be positioned as far away as possible from the cavity wall, the diameter is set to be 2 mm smaller than the width of the chip. This ensures that there is enough material left to manufacture the slit used to guide the chip. Since this hole is a circular waveguide with a width of around half of the diameter of the cavities and the resonance frequency of the transmon is chosen to be between the cavity resonance frequencies, meaning in a range of 5–7 GHz, we can be sure that the attenuation is sufficient to prevent any leakage of the electric field.

Now we are left with basically two parameters to fully determine our system Hamiltonian: the z-position of the chip and the geometry of the antennas. The first can be found by simulating the electric field and choosing the z-position where the electric field is the strongest. This point is located around 1.2 mm below the top of the pin. Therefore, the device is designed such that the top of the two pins are at the same height, and the transmon is inserted 1.2 mm below.

A suitable geometry of the transmon antennas can only be found by trial and error since we can decide for any two-dimensional shape. Firstly, we have to determine the coupling strength, which we want to achieve. For an easy readout of the transmon's state, it has to be coupled strongly to the cavities, which means we are striving for a coupling coefficient of $\chi_{rt}/2\pi > 1$ MHz.

Modelling the transmon in HFSS

To simulate the important Hamiltonian parameters of the system, we are using HFSS to extract the admittance $Y(\omega)$ from the viewpoint of the transmon. This information can then be used for further calculations using the black-box quantization techniques as introduced in section 3.3. The transmon's antennas were modelled as two two-dimensional sheets connected by a lumped inductance and capacitance, which corresponds to the later fabricated Josephson junction with an inductance of 7 nH and a capacitance of 4 fF. Its resistance, which could arise from dissipation in the junction, is neglected. The junction capacitance could only be guessed from the anharmonicity of the fabricated qubit since it will vary depending on the manufacturing process.

In contrast to E_J, which depends on the thickness of the oxide layer of the junction, E_C is set by the device geometry and can, therefore, be determined with numerical simulations. Starting with a typical 3D transmon geometry, which can be seen in 4.7 **A**, we quickly realized
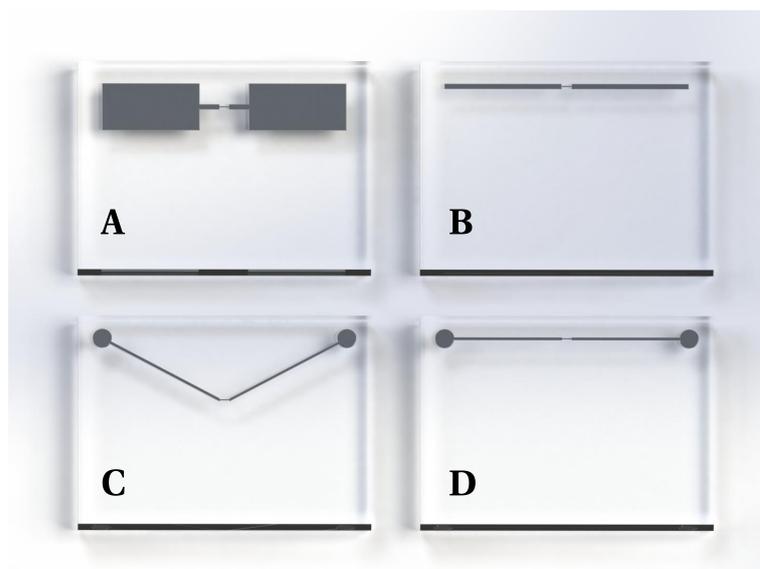
Figure 4.7: **Different versions of the transmon antennas.** In this rendering, the aluminum antennas are shown in gray on the translucent sapphire substrate. **A** Overall large antennas would ensure a strong coupling, but E_C is too low reducing the anharmonicity too far. **B** Thin antennas correspond to a high anharmonicity but a weak coupling to the cavity. **C** This geometry allows for a strong coupling since the antennas are aligned parallel to the electric field vector of the cavity mode, while at the same time the smaller area of the antennas ensures a smaller capacitance keeping the anharmonicity of the qubit at an acceptable level. **D** The closest we could get to the desired system parameters is a strait geometry together with circular antenna pads, which provide a strong coupling.

that this would result in a too-small E_C and, therefore, not a sufficient anharmonicity. Next, we used thinner simple bar-shaped antennas, which can be seen in Figure 4.7 **B**, to reduce the capacitance and found that these give us the desired anharmonicity. However, the coupling to the electric field is too weak to produce the desired dispersive shift of around 1 MHz. This could be compensated for by using longer antennas and a wider sapphire chip, but one would have to drill a larger hole into both cavities distorting the shape of the electric field.

So, the logical next step is to combine the best of both worlds to find suitable transmon geometries, which are shown in Figure 4.7 **C** and **D**. Here we ensure a large coupling by using circular antenna pads with a diameter of 200 µm. With this design, the major part of the antenna reaches far into the cavity, where there is enough spacing between the pads and the cavity walls. An aluminum strip of 50 µm is used to connect the two pads to the junction. The overall length of the transmon is 5 mm, and it is manufactured on an 8 mm wide sapphire chip, which has a length of 21 mm, so it reaches out of the aluminum block to be fixated with a clamp. To improve

the coupling to the cavity mode, our first idea was to angle the antennas, so they are parallel to the electric field vectors. However, as it turns out, a straight antenna design is more beneficial, which might be because overall the antenna is more immersed in the electric field generating a larger overlap between it and the transmon's dipole moment.

Thermalization of the transmon

Besides the lid used for a light-tight seal of the cavities, there is another component not crucial for the system's Hamiltonian but the thermalization of the transmon. The whole aluminum housing is cooled by bolting it to a copper plate, which is mounted to the base plate of a dilution refrigerator. However, the transmon is located on a sapphire chip, which touches the aluminum only over a small area on the slits, which guide the sapphire. So to ensure sufficient contact to the base plate and further secure the position of the chip, a copper clamp is designed, which is shown in Figure 4.6 **B**. Copper is used since it conducts heat better than aluminum at such low temperatures. The copper clamp consists of an upper and a lower part, between which the sapphire chip can be placed. Then the two parts are tightened to ensure good contact between them and the sapphire. The clamp itself is not only cooled via the aluminum housing but is also connected to the base plate using copper braids. These are attached to the clamp in the slits on the side of the clamp. The whole clamp is fixed by two screws going into the aluminum housing.

4.4 Calculating the system's Hamiltonian

To extract the most important system parameters before actually building the system, we performed a full simulation of $Y(\omega)$ and used the black-box quantization techniques introduced in Chapter 3.3 to calculate the zero-point fluctuations for equation (3.62). To further determine the renormalized resonance frequencies and cross- and self-Kerr coefficients, one can either use a fourth-order approximation or numerically diagonalize the full Hamiltonian. For both of these tasks, a Python script has been written, which can be found in the Appendix A. Of course, we also have to truncate the Fock space in the numerical diagonalization since the matrices grow exponentially. Therefore, we here used states up to the twelfth Fock state and expanded the cosine up to twelfth order. The resulting parameters can be seen in Table 4.2. The given error was extracted by assuming that the qubit could be positioned with a precision of $\pm 300\,\mu\text{m}$ and conducting six further simulations moving the qubit in either direction. The error is given as the standard deviation from the different parameter values.

Table 4.2: **The simulated Hamiltonian parameters of the system.** The parameters were calculated expanding the cosine in equation (3.62) up to fourth-order and applying the RWA (With approximation) and by diagonalizing the Hamiltonian (Through diagonalization). The parameters corresponding to the transmon, storage and readout cavity are denoted with t, s, and r, respectively. The rightmost column gives the deviation between the values obtained by the approximation versus the diagonalization. The error was determined by displacing the sapphire chip 0.3 mm from its center position in either direction and calculating the standard deviation for the parameter values.

Parameter	With approximation	Through diagonalization	Deviation
$\omega_\mathrm{s}/2\pi$	4.628(1) GHz	4.628(1) GHz	-
$\omega_\mathrm{t}/2\pi$	6.029(18) GHz	5.917(17) GHz	2 %
$\omega_\mathrm{r}/2\pi$	8.778(1) GHz	8.778(1) GHz	-
$\chi_\mathrm{st}/2\pi$	0.9(5) MHz	1.2(8) MHz	25 %
$\chi_\mathrm{rt}/2\pi$	1.6(7) MHz	1.4(7) MHz	13 %
$\chi_\mathrm{sr}/2\pi$	6(2) kHz	6(2) kHz	-
$K_\mathrm{s}/2\pi$	1.9(6) kHz	3.2(6) kHz	41 %
$K_\mathrm{t}/2\pi$	135(2) MHz	140(2) MHz	4 %
$K_\mathrm{r}/2\pi$	4.5(9) kHz	3.7(9) kHz	18 %

The resonance frequency of the three modes can be engineered to fulfil the criteria stated in Section 4.1, where we have chosen the transmon frequency $\omega_\mathrm{t} = \omega_\mathrm{ge} = 5.892(17)$ GHz to be between the storage and readout cavity with $\omega_\mathrm{s} = 4.628(1)$ GHz and $\omega_\mathrm{s} = 8.778(1)$ GHz, respectively. While considering higher Fock states hardly changes the cavity frequencies, the qubit frequency is shifted by more than 100 MHz. Moving the sapphire also mostly affects the qubit frequency leading to an error of 17 MHz. An explanation for this is the change in E_C when retracting the qubit inside the horizontal hole, increasing the overall capacitance.

With this design we achieved the desired dispersive coupling strength of around 1 MHz with $\chi_\mathrm{st}/2\pi = 1.2(8)$ MHz and $\chi_\mathrm{rt}/2\pi = 1.6(7)$ MHz for the storage- and readout-transmon coupling, respectively. These values show a large deviation between the approximation and the diagonalization with an error of up to 25 %. Moreover, we also see that the coupling strength is highly dependent on the position of the transmon changing by more than 50 % for the storage-transmon coupling. This can be explained by the fact that the amplitude of the electric field drastically decreases towards the cavity walls. This means that the coupling to one cavity will be heavily reduced when moving the qubit away from the cavity's center.

Looking at the self-Kerr coefficients, we are expecting a qubit anharmonicity of 140(2) MHz. Especially the approximated values for K_s and K_r are showing a large deviation from the diagonalization. All in all, we can confirm that the approximations neglect too much information and for a more precise calculation, the diagonalization of the system's Hamiltonian should be considered.

5 Fabrication of the cavity-transmon system

5.1 Fabrication of the cavities

In the course of this thesis, two cavity systems were manufactured: one made of aluminum and another made of niobium. For both systems, the same blueprint as described in Chapter 4 was used.

Both elements have their perks and disadvantages. High-purity aluminum, for example, is cheaper, easier to manipulate, and the treatment of the surface can be done in a single step with acids that are relatively safe to handle. On the other hand, niobium is the element with the highest critical temperature of 9.26 K, meaning that there will be fewer quasiparticles, which would contribute to conductor losses [60]. Therefore, we are expecting higher internal quality factors for the niobium cavities and with them longer lifetimes of the photonic modes. However, the surface treatment of niobium is a more complex process, which can not be done without special equipment and training in handling more dangerous acids like hydrogen fluoride (HF).

The surface treatment, i.e., a removal of 100–200 µm from the cavity walls, is necessary because both cavity systems are fabricated using a combination of drilling and so-called *plunge erosion*. Both techniques leave a rough surface, which needs to be evened out. Moreover, the acids can remove the oxide layer on the surface, which would also lead to increased surface losses. The qualitative connection between the thickness of the removed layer and internal quality factor has already been extensively studied in [50] showing that for both aluminum and niobium, a removal of up to 150 µm leads to an increase of the internal quality factor. More than that shows no further improvements.

Checking the cavity's dimensions

Before proceeding with the treatment of the surface, the cavity's dimensions have been measured to determine the thickness of the removed surface later. Furthermore, the length of the cavity pins has been measured since the resonance frequencies are highly dependent on this parameter.

In the following Table 5.1 the most important dimensions, the diameter of the cavities d_{cav}, the length of the pins l_{pin}, and the length of the waveguide part of the cavities l_{wg}, are given before treating the surface. The diameters of the cavities are nearly identical, only varying by about half a percent. Also, the waveguide sections are nearly similar and long enough to attenuate the electric field before it can reach the top of the cavity. In contrast, the length of the pin is significantly smaller in the niobium cavity. This could be explained by having a closer look at the working principle of plunge erosion. Firstly, a hole with the diameter of the

Table 5.1: **The dimensions of the aluminum and the niobium cavities before the surface treatment.** Here, the diameter of the cavities d_{cav}, the length of the pins l_{pin}, and the length of the waveguide part of the cavities l_{wg} are given. The error of the values is 10 µm.

Material	Cavity	d_{cav} / mm	l_{pin} / mm	l_{wg} / mm
aluminum	Storage	10.39	14.40	29.96
	Readout	10.40	6.75	29.94
Niobium	Storage	10.38	14.18	30.03
	Readout	10.37	6.64	29.99

cavity is drilled into the material. Afterwards, a negative of the cavity, where the pin is now a hole in a cylinder, is fabricated out of wolfram. This piece is then used as an electrode, and a voltage is applied between the cavity material and this wolfram piece. When the negative is moved inside the raw cavity, the discharge, which occurs when the two pieces are in close proximity, will remove a small layer of material. This works very well for the aluminum cavity because the high-purity material will evaporate easily at 2327 °C. On the other hand, niobium is a tough material and will only evaporate at 4744 °C, which is much closer to the evaporation temperature of wolfram at 5930 °C. Consequently, during the process of removing niobium also part of the wolfram electrode will be removed, which is far more significant than in the case of aluminum. This means that the pin will be effectively shortened. To compensate for this effect, we used two electrodes successively to create the pins in the niobium cavities. However, as the measurements show, the niobium pin of the storage cavity is 220(14) µm and the one of the readout cavity 110(14) µm shorter than the respective aluminum pins. Moreover, having a look at the length at the of the waveguide section, we can see that this part is only 50–80 µm longer in the niobium cavity. This can be explained by the fact that the shortening of the wolfram electrode is especially prominent at the top of the electrode, which effectively moves the side, on which the pin is connected to the cavity upwards reducing the length of the pin. Additionally, we note that the wolfram electrode is not only shorted but also becoming round. This leads to a smoother transition from the pin to the cavity wall, which could change the shape of the electric field.

5.1.1 Surface preparation of the aluminum cavity

In order to achieve the highest possible quality factors, the first cavity consists of high purity 5N-aluminum. The surface preparation is done with the commercially available *Aluminum Etch* by Alfa Aesar, which consists of nitric and phosphoric acid and has an etch rate of 100 Å/s at 50 °C for pure aluminum.

Table 5.2: **The dimensions of the aluminum and the niobium cavities after the surface treatment.** Here, the diameter of the cavities d_{cav}, the length of the pins l_{pin} and the length of the waveguide part of the cavities l_{wg} are given. The error of the values is 10 μm.

Material	Cavity	d_{cav} / mm	l_{pin} / mm	l_{wg} / mm
aluminum	Storage	10.10	14.39	29.97
	Readout	10.09	6.73	29.95
Niobium	Storage	10.07	14.17	30.05
	Readout	10.04	6.62	30.01

In a chemical reaction, the nitric acid creates an aluminum oxide layer, which can then be dissolved by the phosphoric acid [61] as

$$7\,\mathrm{Al} + 5\,\mathrm{HNO_3} + 21\,\mathrm{H_3PO_4} \longrightarrow 7\,\mathrm{Al(H_2PO_4)_3} + 13\,\mathrm{H_2O} + 2\,\mathrm{N_2} + \mathrm{NO_2}. \tag{5.1}$$
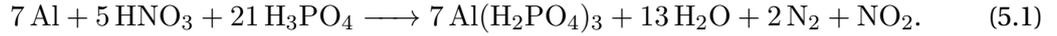
One thing to note here is that the process is exothermal, and the etching rate is highly dependent on the temperature. Therefore, and since we want the chemical reaction to take place at constant 50 °C, we are beginning the treatment by preheating the etching solution to 45 °C. This is to avoid overheating when putting the aluminum cavity into the acid. As soon as the aluminum is in the bath, we can turn off the heat and use a Teflon stirring bean to spread the heat evenly. By stirring the solution, gas bubbles forming inside the cavity system, which would prevent the acid from getting in contact with the aluminum, can be removed. The reaction itself will increase the temperature to 50 °C, which can further be controlled by placing cold, wet towels around the glass cylinder containing the acid. Due to prior works in our group, we decided to etch for 4 h replacing the acid by a fresh aluminum etch solution after 2 h. Former measurements showed that by this a layer of 150(10) μm was removed from the surface.

A comparison of the cavity's dimensions before and after the surface preparation shows that an average of 150(30) μm had been removed from the surface. To extract this value, the distance between eight opposing surfaces were measured. The most important dimensions are given in Table 5.2. In the finer parts of the structure, for example, the guiding slit, a layer of only 107(5) μm had been removed. This can be seen in Figure 5.1 **A** and **B**. An explanation could be the limited acid flow inside this region, leaving gas bubbles and saturated acid around for longer than on the larger surfaces. However, this is not a problem but beneficial since the guiding slit does hardly contribute to the surface loss, and we are desiring a tight fit for the sapphire chip. After etching, the slit has a width of 615 μm and is housing a 330 μm thick sapphire chip. This justifies the earlier assumption that the positioning error of the qubit will be around or below 300 μm.
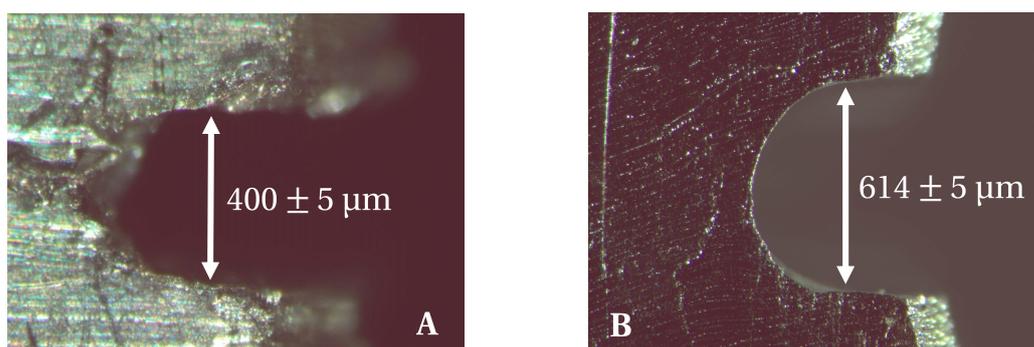
Figure 5.1: **A close-up image of the guiding slit taken with an optical microscope. A** Before the surface treatment, the slit has a width of 400(5) µm. **B** The etching increased the width of the slit to 614(5) µm.

5.1.2 Surface preparation of the niobium cavity

The surface treatment of the niobium cavity is more complex, and there are no commercially available solutions for etching niobium. Therefore, the treatment is done by an experienced chemist, who is using the buffered chemical polishing technique (BCP) [60].

BCP consists of two alternating processes. First, one has to dissolve the oxide layer Nb_2O_5, which forms on the surface of niobium by using HF:

$$Nb_2O_5 + 10\,HF \longrightarrow 2\,NbF_5 + 5\,H_2O. \tag{5.2}$$
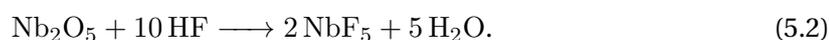
Afterwards, the surface needs to be reoxidized, which is done by a strongly oxidizing acid, here nitric acid HNO_3 is used:

$$6\,Nb + 10\,HNO_3 \longrightarrow 3\,Nb_2O_5 + 10\,NO + 5\,H_2O. \tag{5.3}$$
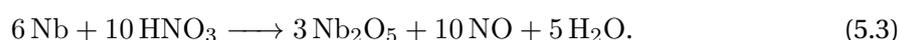
A third component, called a buffer substance, is added to reduce the etching speed. For this, we used phosphoric acid H_3PO_4. Moreover, the mixture needs to be cooled down below 15 °C to ensure a low pick-up of hydrogen atoms, which would reduce the quality factor [60].

For our niobium cavity, we prepared a mixture containing 1 part HF (38–40 %), 1 part HNO_3 (65 %), and 2 parts H_3PO_4 (85 %) in volume, which should result in a removal rate of about 1 µm/min [62]. For the etching procedure, the solution was cooled down to 4 °C. After treating the cavity for 37.5 min, it was rotated by 90° and the solution was replaced by a fresh one. Then the procedure was repeated.

Measuring the cavity's dimensions before and after the etching, we determined that with this procedure, a surface layer of 170(30) µm was removed. Again, the most important dimensions are given in Table 5.2.
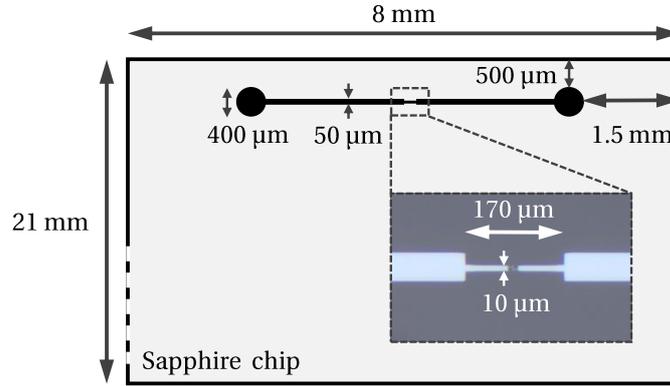
Figure 5.2: **The dimensions of the transmon (black) and the sapphire chip (white).** The antennas are located 500 μm from the top edge and 1.5 mm from the side edge of the sapphire chip. The overall length of the antennas is 5 mm. As shown in the close up of the junction, the leads are shrunken to 10 μm before they are connected to the junction to allow for the fabrication of sharp edges.

5.2 Fabrication of the transmon

The transmon, as shown in black in Figure 5.2, is patterned on a 8.0 mm × 21 mm sapphire chip with a thickness of 330 μm. It consists of two aluminum antennas and an Al/AlO$_x$/Al junction. The antennas have an overall length of 5 mm, and the circular pads a diameter of 400 μm, which are connected to the junction via 50 μm wide leads. More information about the dimensions of the transmon can be seen in the figure above.

The junction is fabricated with the bridge-free technique using standard electron-beam lithography and shadow-mask evaporation. In two evaporations steps, thin aluminum films with a thickness of 25 nm and 30 nm are deposited. These layers are separated by an AlO$_x$ barrier grown through thermal oxidation for 1 min in 0.5 mbar static pressure of a gaseous mixture of 67 % argon and 33 % oxygen.

After fabrication, we can measure the normal-state resistance R_n of the junction to predict the Josephson inductance L_0. For this we use the Ambegaokar-Baratoff relations [63] and Equation (3.14):

$$L_0 = \frac{h}{2\pi^2} \frac{R'_\mathrm{n}}{\Delta}, \tag{5.4}$$

where $R'_\mathrm{n} = 1.17 R_\mathrm{n}$ is the equivalent low-temperature value of the tunnel resistance and Δ is the superconducting energy gap of aluminum. For the upcoming experiments, we are using a transmon with a normal-state resistance of 5.4 kΩ, which corresponds to a Josephson inductance of approximately 7 nH.

6 Measurement setup

The measurement setup used to characterize the system is depicted in Figure 6.1. The resonator is located inside an Oxford delusion refrigerator mounted to the base cooling stage, which is set to reach a temperature of about 15 mK. The input signals are generated at room temperature and carried to the base stage via coaxial stainless-steel cables.

For the upcoming experiments, the microwave signals are either generated by a vector network analyzer (VNA), a signal generator, or an arbitrary waveform generator (AWG), which will be connected to the input ports of the setup inside the cryostat. This setup applies to all upcoming measurement. On its way to the cavities, the signal passes through multiple filters to reduce thermal noise and to protect the measurement instruments. Leaving the VNA at room temperature, the signal is, firstly, guided through a DC-block right before entering the cryostat to filter out any DC-offset and to protect the VNA from any DC offsets from inside the fridge. After that, it undergoes an attenuation of 20 dB at the 4 K stage. Next, the signal passes through a 30 dB attenuator, which is attached to the 15 mK plate of the fridge. By this, thermal noise can be filtered out, while the much stronger input signal is arriving at the base stage. The cables provide additional attenuation of around 7 dB. To further compensate for any undesired signals, we then use a DC-to-12 GHz filter and an Eccosorb filter at the lowest stage, which absorbs any infrared radiation in the signal path.

After all filters, the signal passes through a circulator. This circuit element has three ports and allows the signal to leave the fridge through a different line since we do not want the reflected signal to pass through all the attenuators again, but instead want to amplify it. This means that after reaching the inside of the cavity via the small coupling pin on the side of the cavity wall, the signal is reflected and enters the same circulator.

Moving on into the output line, it is again filtered by a DC-to-12 GHz band-pass filter followed by two isolators, which are attached to the 15 mK stage. They act like circulators where signals can only pass through in one direction, so practically no signal can enter through the output port.

Afterwards, the signal is amplified by a high-electron-mobility transistor (HEMT) at 4 K. Optionally, a Josephson parametric converter can be used as a pre-amplifier before the HEMT. A second amplification of 40 dB takes place at room temperature outside the cryostat using a room-temperature amplifier. Finally, the output signal can be recorded by the VNA.
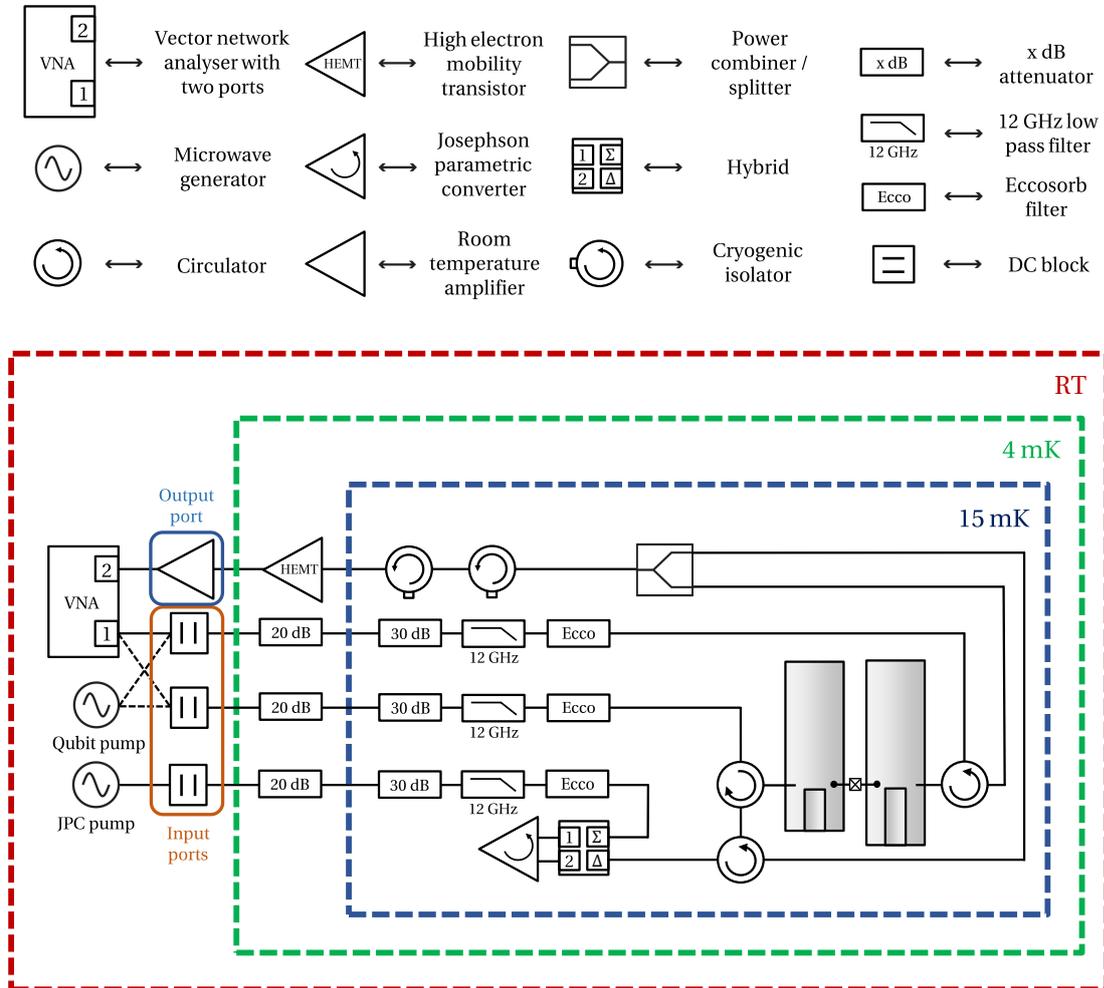
Figure 6.1: **A schematic depiction of the measurement setup.** In the top part, the individual circuit elements are named. The lower part shows the wiring of the measurement setup and the different temperature stages. This part, which is located inside the cryostat, applies to upcoming measurements. More specifically, here the devices, which are used to determine S_{11} of the cavities, are attached to the input and output ports of the setup. The VNA output can be connected to either cavity, indicated by the dashed lines. In addition to the pump for the Josephson parametric converter, a second pump for exciting the qubit can be applied. This will only be needed for the two-tone measurement.

6.1 The readout amplifiers

Amplifying the reflected signal at low temperatures so that it can be read out at room temperature, is a crucial step in our measurement setup because the devices, which are not cooled down are adding significantly more noise, in which our signal would get lost. On the signal's way from one of the cavities to the output port, it is amplified by two devices: a high electron mobility transistor (HEMT) and a Josephson Parametric Converter (JPC).

As can be seen in Figure 6.1, HEMTs are operated at 4 K and provide a gain of around 40 dB over a frequency range of, in our case, 4–8 GHz. However, in the case of single-photon signals, they add tens to hundreds of noise photons. Of course, this can be compensated for by measuring multiple times and averaging, but there is a more efficient way.

Using a JPC as an amplifier will only add such an amount of noise, which is close to the quantum limit of half a photon. This is due to the zero-point fluctuations of a resonator. However, it will only provide a gain of around 20 dB. Now we combine the best of both worlds and use the JPC as a pre-amplifier before guiding the signal through the HEMT to increase the signal-to-noise ratio after the HEMT amplification.

In contrast to a HEMT, which can simply be operated by connecting it to a power source, the main part of JPC is a Josephson ring modulator (JRM), which is embedded inside a resonant circuit. The amplification works by a three-wave-mixing procedure, where besides our signal a pump tone has to be applied. The third frequency is called *idler*.

Generally, the JRM can convert a pump photon at $\omega_{\mathrm{pump}} = \omega_{\mathrm{signal}} + \omega_{\mathrm{idler}}$ into two photons with frequencies ω_{signal} and ω_{idler} and the other way around. The trick is now to apply no signal to the idler port of the JPC, which makes the up-conversion impossible, but allows us to add photons to the signal mode. For this, the idler port is terminated by a 50 Ω terminator to dissipate the photons, which are generated in the idler resonator. In this way, the JPC is operated as a single-mode reflection amplifier.

One thing to note is that JPCs are quite restricted in the range of frequencies that they can amplify since the signal and idler frequencies are given by the length of the stripline resonators, which are connected to the JRM. Therefore, their dynamical bandwidths are only up to 10 MHz. However, they inherit a small flux tunability from the Josephson junctions, allowing the gain frequency range to be shifted by a few 100 MHz.

In this thesis, we used the JPC SN004 with a dynamic bandwidth of 7 MHz at a gain of 20 dB. The amplifier is flux tunable in a range of 8.610–9.026 GHz. Moreover, by varying the pump frequency by 5–10 MHz one can move the amplification peak by around 2–5 MHz. The applied pump power can range from -8 dBm to -6 dBm for an optimal operation. One thing to note here is that a stronger pump power will not only increase the gain but also shift it towards lower frequencies. The linear regime of this JPC ranges from signal input powers of -135 dBm to -125 dBm.
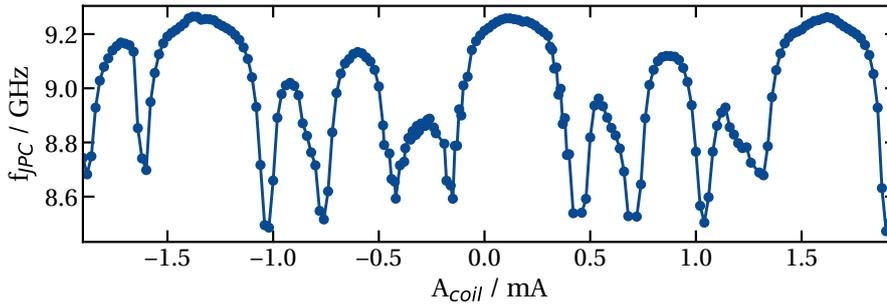
Figure 6.2: **The resonance frequency of the JPC $f_{\mathbf{JPC}}$ depending on the coil current $A_{\mathbf{coil}}$.** Within one period, there are multiple points corresponding to the target amplification frequency.

Setting up the JPC

During the set up of the JPC we have to choose the target frequency, the DC bias current for the coils, which will flux bias the signal and idler resonators, the frequency and the power of the pump signal. To set the center gain frequency to the target frequency, we will be alternating between finding the correct DC bias and the proper pump parameters.

To determine the current resonance frequency of the resonators, we can measure the phase response with a VNA without applying a pump signal. After setting the electrical delay to about 96 ns and choosing the mode *extended phase*, we can see the 2π phase shift of the resonator. After applying a few 10 μA in the bias current, one can see the resonance frequency shifting. Similarly to a squid, the resonance frequency is a periodic function of the flux with, in our case, a period of around 1.5 mA. Since during the cooldown of the superconducting elements flux can be trapped inside the loops of the circuit, the whole periodic function will be shifted, which is why we have to search for the proper DC value, i.e., the correct flux bias, for each new experiment. Since we are not applying the pump signal, which will shift the gain peak towards lower frequencies, we are trying to set the resonance frequency 100 MHz above the target frequency. Note that in one period, there are eight points, which correspond to the target function. To determine the correct points, we are capturing a full 2D flux map and relating the resonance frequency f_{JPC} to the coil current A_{coil}. The result can be seen in Figure 6.2.

Having set the coil current, we can use a signal generator to apply the pump tone at -7 dBm, while turning the probe signals down to -110 dBm. At the given bias current, the correct pump frequency is the sum of the signal and idler resonance frequencies. We are relying on manufacturer data to relate the signal frequency, our target frequency, to the idler frequency in order to find a good starting point for finding the best pump frequency. We now continue to increase the pump power in steps of 1 dBm until we can see the amplification peak. Afterwards, the pump power can be varied in smaller increments to achieve a symmetric gain profile with a maximum gain of around 20 dB.

7 Characterization of the three-mode cavity-transmon system

In this chapter, we are using the techniques presented in the previous chapters to characterize the cavity-transmon system. Since we will be using multiple different measurement devices throughout the experiments, they will be introduced with the experiment. We start with the measurements of the resonance frequencies and decay rates of the cavities made from aluminum and niobium without the qubit inside. Then, the sapphire chip with the transmon is inserted into the aluminum cavity causing the three modes to couple. We are determining all parameters of the system's Hamiltonian and comparing them to the simulation results presented in chapter 4.

7.1 Quality factor of the cavities

There are essentially two ways, with which one could determine the quality factors of a cavity. The first would be capturing a spectrum for a small range of frequencies around the resonance frequency of the cavity with a VNA. Afterwards, the spectra can be fitted using the circle fit routine, introduced below, which determines the desired parameters. Another way to determine the quality factors is to perform a time-domain measurement on the reflected signal, while the cavity receives a short microwave pulse. The response of the cavity can be fitted to calculate the parameters.

7.1.1 Measuring the quality factors with the VNA

To capture a spectrum, a VNA sends out a probe signal with frequency ω and compares its complex voltage $V_{\text{in}}(\omega)$ with the scattered signal $V_{\text{out}}(\omega)$. The complex scattering parameter S_{11} is then given by

$$S_{11}(\omega) = \frac{V_{\text{out}}(\omega)}{V_{\text{in}}(\omega)}. \tag{7.1}$$

For analyzing the results, we are using the magnitude of the scattered signal $|S_{11}(\omega)|^2$, which will be given in units of decibel (dB)

$$|S_{11}(\omega)|^2[\text{dB}] = 10 \log_{10}\left(|S_{11}(\omega)|^2\right), \tag{7.2}$$

and the relative phase, which can be found in the argument of S_{11}.

One of the advantages of measuring with a VNA is that the experimental setup is relatively simple since only one device is needed. Before conducting the measurement, we only have to decide on a frequency range and resolution. To improve the signal-to-noise ratio, we can either increase the number of spectra that will be recorded and averaged or reduce the intermediate frequency (IF) bandwidth. By doing the latter, we are narrowing the frequency window, which is used for the recording of one point of our spectrum. By this, we can exclude noise from other frequencies. However, the IF bandwidth is inversely proportional to the measurement time. As always, we have to find a compromise between noise and waiting time.

Practically, we are doing a reflection measurement, although because of the circulator, the signal leaves the system through a different port. If only the external losses with a rate κ_{ext} are present, the transmitted signal S_{11} will be given by a Lorentzian and the reflected signal goes to $S_{11}(\omega_0) = 0$ at the resonance frequency ω_0 [64]:

$$S_{11}(\omega) = 1 - \frac{\kappa_{\text{ext}}}{\kappa_{\text{ext}} + 2i(\omega - \omega_0)}. \tag{7.3}$$

However, in the experiment the resonator, shows a finite internal energy decay rate κ_{int}. To account for these losses, an imaginary component is added to the resonance frequency $\tilde{\omega} = \omega_0 + i\kappa_{\text{int}}/2$. The transmitted signal with internal losses in the cavity resonator is given by

$$S_{11}(\omega) = 1 - \frac{\kappa_{\text{ext}}}{\kappa_{\text{ext}} + \kappa_{\text{int}} + 2i\left(\omega - \omega_0\right)}. \tag{7.4}$$

Using the definition of the quality factor in Equation (3.54) and assuming that the only external losses are due to the coupling of the resonator to the transmission line, S_{11} reads

$$S_{11}(\omega) = 1 - \frac{Q_{\text{l}}}{Q_{\text{c}} + 2iQ_{\text{l}}Q_{\text{c}}\left(\omega/\omega_0 - 1\right)}. \tag{7.5}$$

We can go on and show that the complex transmitted signal traces out a circle in the IQ plane [65]. For this, we define an angle $\theta(\omega)$ such that

$$\tan\left(\theta(\omega)\right) = 2Q_{\text{l}}\left(\frac{\omega}{\omega_0} - 1\right). \tag{7.6}$$

With this definition, our reflected signal is given by

$$S_{11}(\theta) = 1 - \frac{Q_{\text{l}}}{Q_{\text{c}}}\left(\frac{1}{1 - i\tan(\theta)}\right). \tag{7.7}$$

After using trigonometric identities, we end up with

$$S_{11}(\theta) = 1 - \frac{Q_{\text{l}}}{2Q_{\text{c}}}\left(1 + e^{2i\theta}\right). \tag{7.8}$$
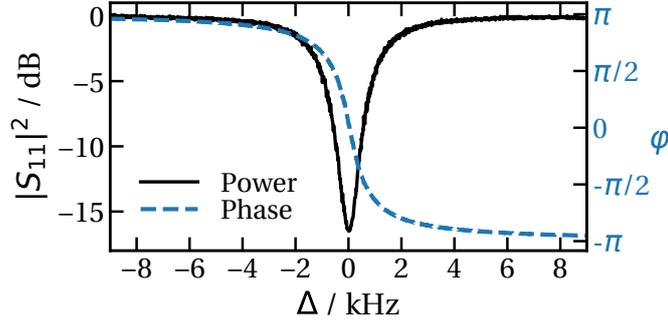
Figure 7.1: **The resonance peak of the readout cavity (aluminum).** The plot is showing the magnitude (black) and the phase (dashed blue) of S_{11} for a probe power of -15 dBm. The magnitude has been chosen such that the off-resonant reflection is at 0 dBm. On the x-axis, the resonance frequency of 8.77832827(6) GHz is set to zero. The width of the dip corresponds to an internal quality factor of 17.4×10^{-6}. During the crossing of the resonance frequency, the phase is shifted by 2π.

Now we can see that the diameter of the circle is given by $\frac{2Q_{\mathrm{l}}}{Q_{\mathrm{c}}}$. Impedance mismatches, crosstalk, and other imperfections will result in a displacement of the circle in the complex plane. This circle can now be fitted with the circle fit routine written by Zöpfl and Schneider [66]. The fit is a robust tool to extract the loaded, internal, and coupling quality factors of a resonator. Moreover, it determines its resonance frequency.

Besides the frequency range, we can also set the power of the VNA signal P_{in}, which will be sent to the cavities. However, the actual parameter of interest is the average number of photons $\bar{n}_{\mathrm{ph}}$, which we will trap inside the cavities given P_{in}. With the knowledge of the cavities' quality factors and resonance frequencies together with the overall attenuation, including input lines and filters, we can estimate an upper bound for $\bar{n}_{\mathrm{ph}}$ [67]:

$$\bar{n}_{\mathrm{ph}} = \frac{2}{\hbar\omega^2}\frac{Q_{\mathrm{l}}^2}{Q_{\mathrm{c}}}P_{\mathrm{in}}. \tag{7.9}$$

7.1.1.1 Results

As an example, the resonance peak of the readout cavity in aluminum is shown in Figure 7.1. At the resonance, the reflected signal is reduced by 16 dBm showing a Lorentzian shape. The phase of the signal follows a hyperbolic tangent and is shifted by 2π while crossing the resonance frequency. The resonance frequencies of the two cavity systems are given in Table 7.1. They were extracted using the circle fit routine. We can see that the resonance frequencies of the aluminum and niobium system differ by 198 MHz and 456 MHz for the storage and readout cavities, respectively. This can partially be explained by the difference in cavity pin length due

Table 7.1: **The measured resonance frequencies, lifetimes, and coherence times of the cavities.** The frequencies were extracted used the circle fit routine. The cavity lifetimes and coherence times were calculated for the single-photon level since this provides an overall lower bound to T_1 and T_2^*.

Material	Cavity	f_r / GHz	T_2^* / ms	T_1 / ms
aluminum	Storage	4.633 837 45(4)	0.68(16)	0.69(4)
	Readout	8.778 328 27(6)	0.28(8)	0.28(8)
Niobium	Storage	4.831 549 000(3)	0.84(11)	0.85(3)
	Readout	9.234 840 496(2)	0.49(4)	0.49(6)

to the evaporation of the wolfram electrode during the fabrication process of the niobium cavity. However, this difference in frequency is larger than the difference in pin length would suggest. Another effect, which could contribute to the increase in frequency, is the degradation of the electrode. This leads to a rounding of the pin's edges and also shortens the pins effectively, which might reshape the electrical field. Looking at the resonance frequencies of the storage and readout aluminum cavity, we can see that the simulations predicted accurate resonance frequencies since these are only deviating from the measurements by 18 MHz and 60 MHz. This could be due to the limited precision of the manufacturing or etching process.

Now we can record the spectra with different probe powers to see how the internal quality factor changes depending on the energy stored inside the resonator. In Figure 7.2, the internal quality factor is plotted against the average number of photons in the cavity, calculated with Equation 7.9. The first thing to note is that the niobium cavities have an overall higher internal quality factor than the ones made from aluminum. For the aluminum cavity, the internal quality factor reaches values from around 15×10^6 for a few photons to up to 27×10^6, while the niobium cavities achieve values from 25×10^6 to 43×10^6. The error bars of the circle fit are too small to be seen in the figure. While this error might be true when probing with high power, for small photon numbers the fluctuations rather suggest an error of around 3×10^6. The difference in the internal quality factor between aluminum and niobium can be explained by the smaller number of tow-level systems (TLS) on the niobium surface, which are known to dissipate energy extracted from the cavity mode [67]. However, for niobium, much higher internal quality factors in the range of 200 to 300 million were expected. Two possible explanations for this could be that, firstly, we might have used not enough etching solution to dissolve the H_2, which can then be found in the surface layer resulting in a higher surface loss [60]. Secondly, we used PTFE-coated pliers during the etching procedure. This coating could have been partially dissolved and afterwards deposited on the cavity walls. Both of these effects could be accounted for with a high-temperature vacuum annealing.
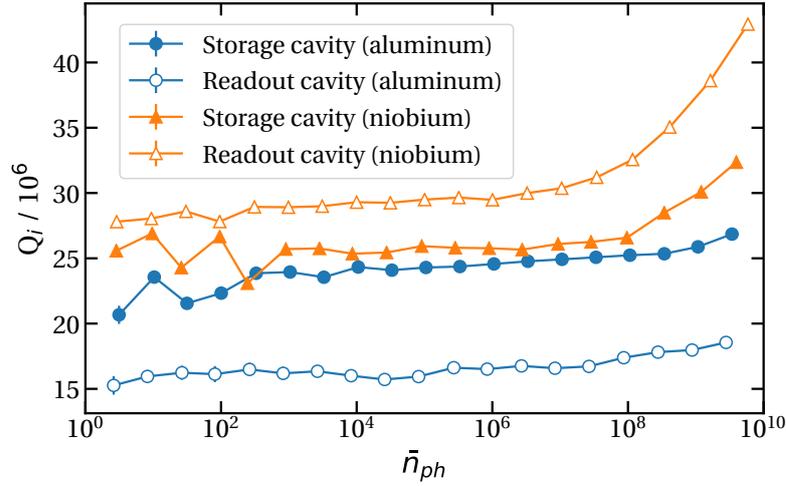
Figure 7.2: **The internal quality factor as a function of the average number of photons inside the cavity.** Overall, the niobium system (orange) is showing slightly higher internal quality factors compared to the aluminum system (blue). Q_i increases with the average photon number. The error bars are too small to be seen.

More interestingly, we can observe an increase in Q_i for larger photon numbers. This effect is especially prominent in the niobium system for $\bar{n}_{ph} > 10^8$ and common in these types of resonators. Since this loss mechanism can be saturated, we are considering material defects, i.e., impurities on the surface of the cavity as its cause and therefore, the limiting factor for the cavity lifetime [67].

Since the purpose of this cavity-qubit system is to store the qubit's state as a cavity mode, the most important parameter is the lifetime of the cavity modes at the single-photon level. We have to note the fact that with the VNA, one essentially measures dephasing and the energy decay rate of the cavity at the same time. The quality factor is given by the width of the absorption peak, which gets broader not only with a higher energy loss rate but also if the peak shifts during the averaging of the measurements. The peak shifts will effectively reduce the extracted quality factor and could be caused by the slightest variations in the length of the cavity pin since even changes in the picometer range can shift the frequency by several hertz. This means that having determined the resonance frequencies and the internal quality factors, we can use Equation 3.54 to calculate $T_{2,s/r}^*$ of the cavities. The results are given in Table 7.1. Our cavities achieve a maximum coherence time of 0.68(11) ms, which is about 7–17 times longer than typical transmon lifetimes of around 100–40 µs.

All in all, we see that our cavities are very well suited for their use as a quantum storage. Nonetheless, we also want to measure the lifetimes of the cavities. Therefore, we need to only measure the energy decay rate. To resolve this problem, we now present a method for determining the quality factor in the form of time-domain measurements.
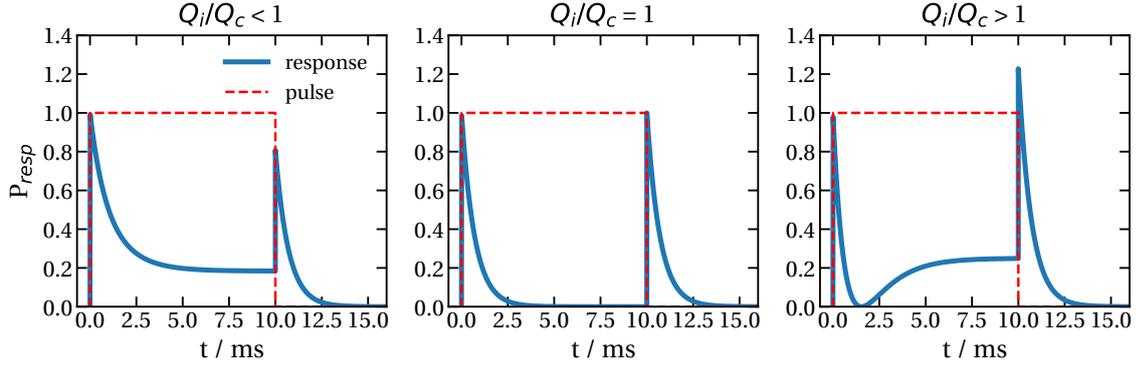
Figure 7.3: **The cavity response P_{resp} (blue line) after applying a square pulse (red dashed line) for three different ratios of $Q_{\text{c}}/Q_{\text{i}}$.** During the pulse, the cavity starts to gain photons. Since the phase of the photons, which are then emitted by the cavity, is shifted by π, they destructively interfere with the photons, which are reflected off the input port of the cavity. For $Q_{\text{c}}/Q_{\text{i}} < 1$, there will always be more photons, which are reflected off the port, so the response never reaches $P_{\text{resp}} = 0$. In the case of $Q_{\text{c}}/Q_{\text{i}} = 1$, the response reaches $P_{\text{resp}} = 0$ in the saturated limit since the photons will exactly cancel each other out. For $Q_{\text{c}}/Q_{\text{i}} > 1$, the response reaches zero before saturating at higher power levels. That can be explained by the fact that photons emitted by the cavity are starting to dominate the response signal after it has reached zero. Therefore, when saturated, the phase of the response is shifted by π. After the pulse is over, the signal decays exponentially revealing Q_{l}.

7.1.2 Determining the quality factors with time-domain measurements

In contrast to the continuous wave measurement with a VNA, this method works by sending short probe pulses to the cavity and recording the response, i.e., the reflected signal. Therefore, we now need a signal generator and a device, which is able to perform time-domain measurements. The output of the VNA is replaced by the *KEYSIGHT MXG Analog Signal Generator N5183B*, and to analyze the response of the cavities, the *Tektronix RSA 5115B* is replacing the input of the VNA. The signal generator produces square pulses with a certain power P_{Pulse}, frequency ω_{Pulse} and length t_{Pulse}. While setting ω_{Pulse} to the resonance frequency of the cavity, we will vary P_{Pulse} to determine the quality factor for multiple input powers. The duration of the pulse is chosen such that the resonator is completely saturated by the time the pulse ends. A sufficient t_{Pulse} can easily be determined when taking a look at the response signal, which can come in three different shapes depending on the ratio of $Q_{\text{c}}/Q_{\text{i}}$ [68]. The three different curves, together with the pulse, are shown in Figure 7.3.

To explain this curve, we can separate it into two parts: the response signal during the pulse and the one after the pulse. At the beginning of the pulse, no energy is stored inside the cavity. This results in a mismatch and the whole signal is being reflected, which produces a spike.

During the pulse, the cavity slowly starts filling up with photons, and the matching improves. The time scale for this is determined by the coupling to the transmission line Q_c. To see why the power of the response signal is now decreasing, we have to remember that the photons, which entered the cavity and are emitted again, are phase-shifted by π compared the photons reflected on the input port of the cavity. Therefore, they are interfering destructively, and the signal decreases. To go on explaining the response curves, we have to distinguish three different cases: the over coupled ($Q_\text{i}/Q_\text{c} < 1$), the critically coupled ($Q_\text{i}/Q_\text{c} = 1$), and the under coupled ($Q_\text{i}/Q_\text{c} > 1$) cavity.

In the first case, when the response reaches its equilibrium state, there are still more photons being reflected off the cavity port than photons emitted by the cavity. Consequently, the destructive interference is not perfect, and we are left with a constant stream of reflected photons, even when the cavity is saturated, i.e., the power dissipated in the cavity is equal to the power entering the cavity. However, in the critically coupled case, the number of reflected photons is equal to the number of emitted photons, and the signal completely vanishes as soon as the cavity is saturated.

In the third case, the response reaches zero before raising again to its equilibrium point. This is owed to the fact that by the time the cavity is saturated, more photons are emitted by the cavity than reflected off the port. This means that full destructive interference occurs before the equilibrium is reached, which produces a minimum in the signal during the pulse. Afterwards, the signal rises again and is phase-shifted by π. In this example, at the end of the pulse, the equilibrium between the photons going in and out of the cavity is reached. The equilibrium power depends on the Q_c and Q_i as [68]

$$\frac{P(0)}{P(t_\text{Pulse})} = \left(\frac{\frac{Q_\text{i}}{Q_\text{c}} + 1}{\frac{Q_\text{i}}{Q_\text{c}} - 1} \right)^2 . \tag{7.10}$$

However, this is only true if $\omega_\text{Pulse} = \omega_\text{r/s}$. In case of a slight detuning, the response signal starts oscillating, and perfect destructive interference can not be achieved. Even for the off-resonant case, there is an analytical expression for the response during the pulse, which was derived by Paul Heidler in our group and can be found in the Appendix C. If the quality factor was not power dependent, we could use this expression to fit our signal and extract the internal and coupling quality factor. As soon as the pulse ends, we can observe a spike in the response, which can be even higher than the original pulse power. This is because, after the end of the pulse, no more photons arrive at the cavity and can be reflected off the port. Therefore, the measured signal for $t > t_\text{Pulse}$ contains all the photons leaking out of the cavity. In the over coupled case, there will be fewer photons than at the beginning of the pulse, in the critically coupled case, the height of the peaks are equal, and in the under coupled case, the power after the pulse surpasses the one at the beginning of the pulse.
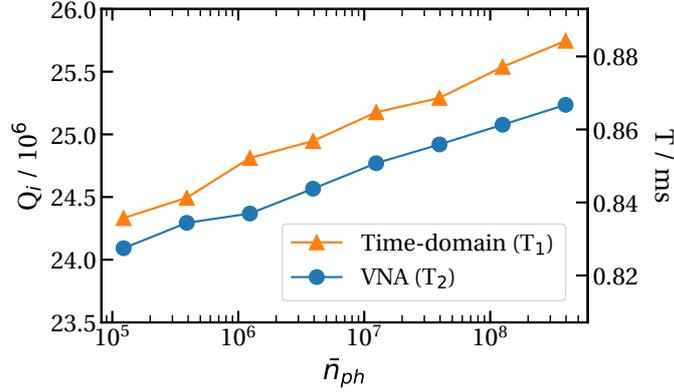
Figure 7.4: **The internal quality factors of the storage cavity in aluminum as measured with a VNA (blue circles) and a time-domain setup (orange triangles).** The values determined by time-domain measurements are 1.5 % higher than the ones recorded with a VNA. The quality factors measured with the time-domain setup and the VNA are converted into the lifetimes and coherence times, respectively. The error bars are too small to be visible.

After peaking, the signal decays, and if the quality factor did not depend on the power stored inside the cavity, this would be an exponential decay. However, as we can see in Figure 7.2, this is not the case. The internal quality factor depends on the number of photons stored inside the cavity. This means that also equation C.1 no longer describes the time dependence correctly if the square pulse deposits a larger number of photons in the cavity.

However, we can nonetheless use the decay of the energy inside the cavity for $t > t_{\text{pulse}}$ to extract Q_l. For this, we only use the first points of the whole decay in a range of 5 dBm and fitted them with an exponential curve. By using the ratio given in equation 7.10, we can then calculate the internal and coupling quality factor.

7.1.2.1 Results

To compare internal quality factors extracted from the VNA and time-domain measurements, we are presenting the values for the storage cavity in aluminum. As shown in Figure 7.4, the time-domain measurements result in around 1.5 % higher quality factors compared to the VNA measurements. However, this increase is smaller than the error assigned to the internal quality factors at the single-photon level. Therefore, we can safely assume that the VNA recordings are sufficient to determine the lifetime of a cavity.
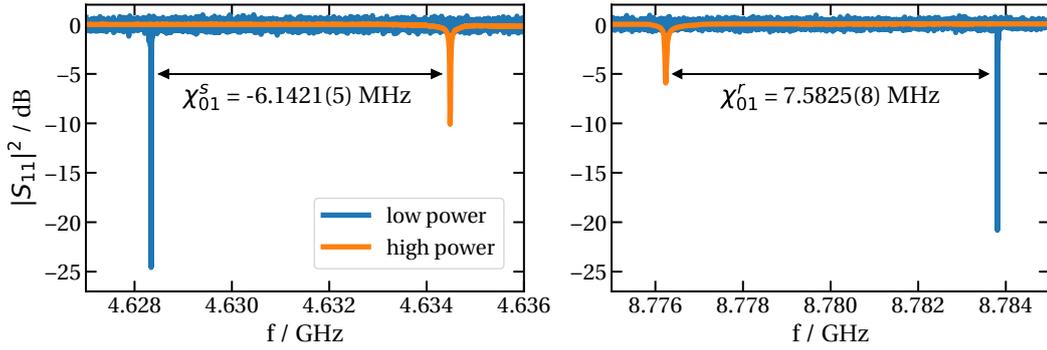
Figure 7.5: **Measuring the cavity resonances with high (orange) and low (blue) power.** The high-power measurement corresponds to $\bar{n}_{\mathrm{ph}}^{\mathrm{high}} \approx 10^6$, whereas the low-power measurement was done with $\bar{n}_{\mathrm{ph}}^{\mathrm{low}} \approx 5$ in the resonator. On the left and right, we can see the two resonances in the storage and readout cavity, respectively.

7.2 The cavity-transmon coupling

There is a variety of methods for determining the strength of the coupling between the cavities and the transmon. Here, measurements using continuous-wave signals as well as pulsed signals were conducted. For the following experiment, we established a close-to-critical coupling between the cavity and the transmission line ($Q_{\mathrm{c}} \approx Q_{\mathrm{i}}$), so the resonance peak would reach maximum depth and would not be broadened by the losses into the transmission lines.

7.2.1 Switching off the nonlinearity

One of the simplest ways to measure the dispersive shift is to make use of the fact that currents higher than the critical current I_{c} of the transmon's junction are carried by quasiparticles (electrons) not Cooper pairs. Therefore, they are not affected by the nonlinearity. That means, when measuring the resonance frequency of one cavity in the cavity-transmon system, one expects to only see a dispersive shift χ_{01} when probing with a power corresponding to a few photons. In this low-power regime, the resonance frequency of the bare cavity ω_{r} gets shifted by the transmon in the ground state to $\tilde{\omega}_{\mathrm{r}} = \omega_{\mathrm{r}} + \chi_{01}$. In Figure 7.5, one can see S_{11} measurements conducted both in the storage and readout cavity in aluminum for different powers.

For the high-power measurements, we used a power corresponding to an average photon number $\bar{n}_{\mathrm{ph}}^{\mathrm{high}} \approx 10^6$ and for the low-power measurements one resulting in $\bar{n}_{\mathrm{ph}}^{\mathrm{low}} \approx 5$.

The results are listed in Table 7.2. For the storage cavity, the dispersive shift due to the transmon in the ground state is with -6.1421(5) MHz smaller than the shift of the readout cavity 7.5825(8) MHz. Firstly, this confirms that our nonlinear circuit element is working and, secondly, we are expecting the state-dependent dispersive shift to be slightly stronger on the readout cavity.

Table 7.2: **The measured dispersive shift by using high and low photon numbers.**
As desired the coupling between the readout cavity and the transmon is higher
than the coupling the storage cavity.

Material	Cavity	$\chi_{01}/2\pi$ / MHz
aluminum	Storage	-6.1421(5)
	Readout	7.5825(8)

Note that the values above have a different sign, which is due to the fact that the transmon's
frequency is higher than the storage but lower than the readout cavity.

7.2.2 Exciting the transmon

To determine the all the remaining parameters of the system, i.e., the state-dependent dispersive
shifts, the anharmonicity of the qubit α, and the qubit life and coherence time, we have to first
find the transition frequency between the ground and the excited state of the transmon. For the
upcoming measurements, we are continuing with a time-domain setup. However, we will have
to generate pulses with a Gaussian-shaped envelope instead of a rectangular one to excite the
qubit. This is due to the fact that the spectrum of a rectangular pulse contains a wide range of
frequencies. Since we only want to drive the $|g\rangle$-to-$|e\rangle$ transition of the qubit without pumping
other transitions, we ideally want to send a pulse with a single frequency. This, of course, is
impossible because the signal is not infinitely long. However, we can reduce the spectral width
of the pulse by using a Gaussian envelope. These pulses will be generated by an AWG from
Signadyne.

   The AWG has an output rate of 1 GS/s, which means that in theory, we could generate a
signal of up to 500 MHz. Because of a filtering procedure, the maximum output frequency is
reduced and, therefore, our AWG can only generate signals of up to 450 MHz. However, since
the qubit's transition frequency lies in the range of multiple gigahertz, and we would rather
generate signal far lower than the theoretical Nyquist limit, we will need to upmix the signal.
This can be done by mixing the output of the AWG with a local oscillator (LO). The setup for this
procedure, together with the devices for the excitation of the qubit and readout of the cavities,
is shown in Figure 7.6. The inputs of the IQ mixer are the LO signal, the sinusoidal AWG signal
with a Gaussian envelope (I) with the amplitude A_{I} and an offset O_{I}, and the quadrature of the
AWG signal (Q), which is phase-shifted by ϕ and has an amplitude A_{Q} and an offset O_{Q}.

   Generally, this will result in an output of the mixer containing the LO frequency together
with the so-called left and right sidebands corresponding to the difference and the sum of the
AWG and LO frequencies, respectively. However, we can reduce the strength of the undesired
LO frequency by varying O_{I} and O_{Q}. Additionally, the signal of the undesired sideband can be

reduced by choosing the correct ratio A_I/A_Q and phase difference ϕ. This method is called single-sideband modulation.

Before the AWG signal can enter the mixer, it needs to be attenuated by 20 dB to avoid driving nonlinearities in the mixer, while still using the maximum output voltage and therefore the maximum resolution of the signal. Hence, the upmixed signal is amplified by 26 dB after passing through a 5.6–7.0 GHz filter for noise reduction. Then, the DC components are removed, and the signal is split for the calibration of the single-sideband modulation using a signal analyzer.

Before the signal enters the cryostat, we add additional signal generators, EXGs from *Keysight*, for the excitation of the qubit and to generate a readout pulse for the cavities. For some of the upcoming experiments, either the AWG or the signal generator for the excitation of the qubit is connected. To achieve a high readout fidelity, we are going to use the high-power readout procedure to determine the state of the qubit. Hence, we are using rectangular pulses to probe the cavity at its bare resonance frequency.

The cavity's response, leaving the cryostat through the output port is downmixed, filtered and amplified to be read out with an ADC.

Determining the qubit's transition frequency

To determine the qubit's transition frequency, we are going to use the time-domain setup in Figure 7.6 without the AWG. With one of the signal generators, we are trying to excite the qubit by applying a rectangular pulse with a set test frequency f_test. This pulse has a length of 50 µs, so we are avoiding a broadening of the spectrum around f_test. The appropriate power of the excitation pulse has to be found through trial and error since we are exciting the qubit through the readout cavity, which is attenuating $f_\text{test} \approx 6$ GHz. Since only one photon needs to reach the qubit, a good excitation power was found to be -35 dBm. After the first pulse, we immediately apply the second one, which is used for the high-power readout of the cavity. As stated in Section 3.3, we have determined the excitation power, which is just below the critical power triggering the resonance of the bare cavity. This can easily be done by recording a spectrum of the high-power peak of the cavity and lowering the pulse power until the resonance vanishes. For the readout cavity and a 5 µs pulse, this happened at a power of -8 dBm.

With these parameters, we can now start varying the test frequency until we see a change in the cavity response. The results can be seen in Figure 7.7. We find the qubit transition frequency at 5.93587(1) GHz. The width of the resonance is determined to be 0.26(1) MHz.
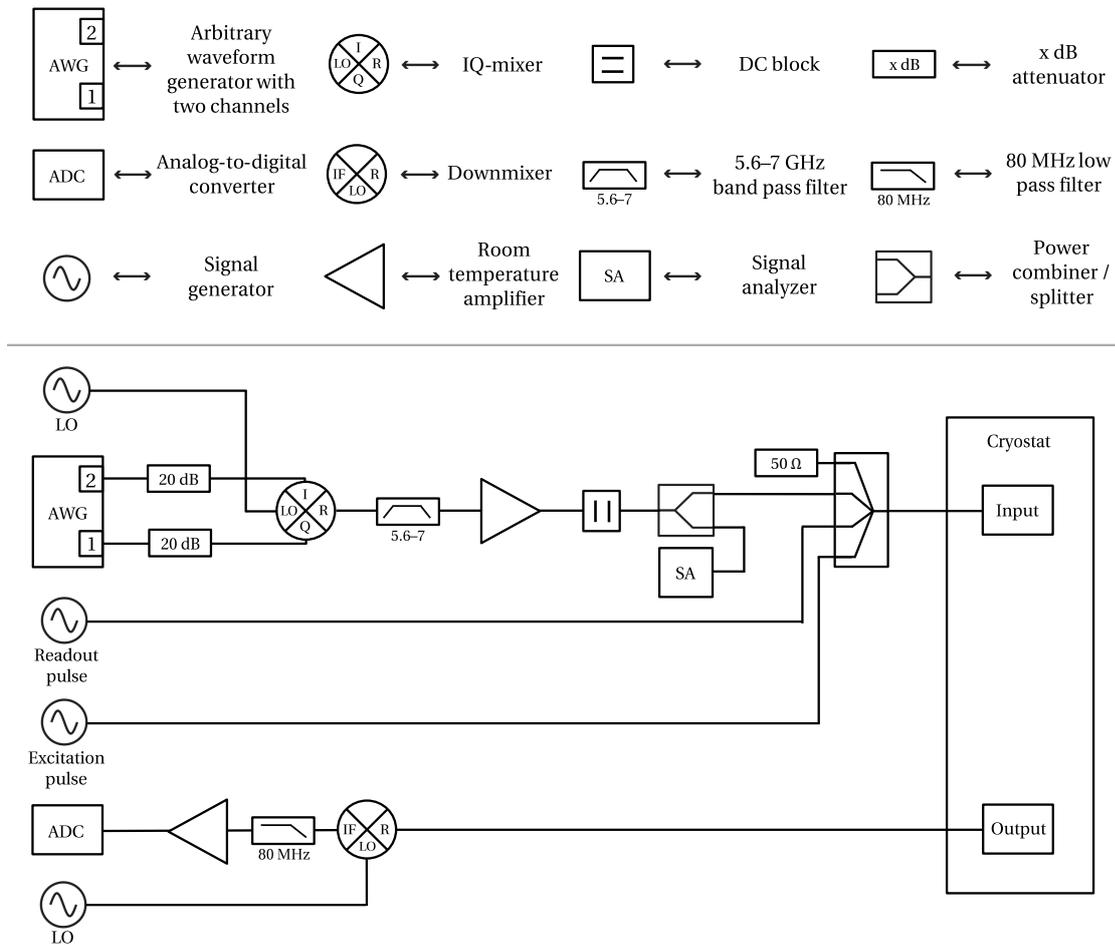
Figure 7.6: **A schematic depiction of the setup used for the generation and recording of pulses**. In the top part, the individual circuit elements are explained. The lower part shows the wiring of the measurement setup up to the input and output port of the cryostat leading to one of the cavities. An AWG is used to generate pulses with a Gaussian envelope. An ADC is recording the cavity's response to the readout pulse. Four additional signal generators are used as local oscillators and to generate excitation and readout pulses.
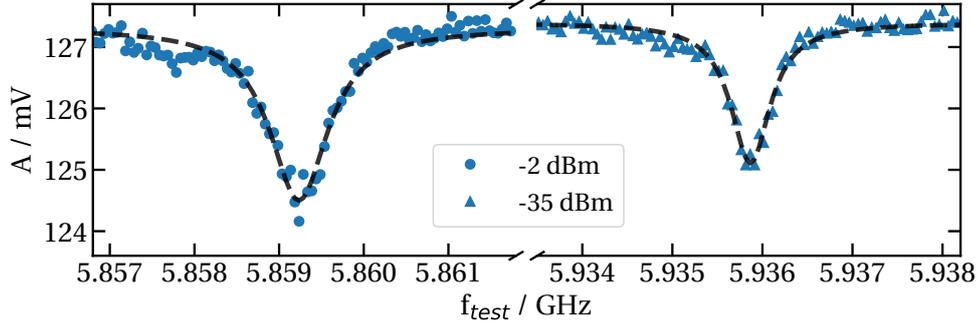
Figure 7.7: **Determining the qubit's transition frequencies.** Right part: The qubit's $|g\rangle$-to-$|e\rangle$ transition is found at a frequency of 5.93587(1) GHz. The measurements are fitted to a Lorentzian (dashed line). Left part: Determining the qubit's anharmonicity using two-photon absorption. The resonance frequency is found at 5.85923(1) GHz, which corresponds to an anharmonicity of 153.27(3) MHz.

Anharmonicity of the qubit

Without changing the setup, we can go on to determine the qubit's anharmonicity. We are going to use two-photon processes to excite the qubit directly from $|g\rangle$ to $|f\rangle$. Since a two-photon absorption is highly unlikely, we have to increase the qubit excitation power to -2 dBm. Looking at the simulations, we are expecting the anharmonicity to be around -140 MHz, which is why we are varying the test frequency in a region, which is -70 MHz lower than the $|g\rangle$-to-$|e\rangle$ transition frequency.

The result can be seen in the left part of Figure 7.7. The two-photon resonance appears at 5.85923(1) GHz, which is corresponding to an anharmonicity of 153.27(3) MHz. With the anharmonicity, we can now deduce more fundamental qubit parameters. Using Equation (3.27) and Equation (3.14), we find the ratio of $E_\mathrm{j}/E_\mathrm{c} = 197.29(8)$, which confirms that our qubit can be classified as a transmon. Moreover, we can calculate the Josephson inductance $L_\mathrm{J} = 7.41(8)$ nH, which is around 6 % higher than the expected value of 7 nH. This deviation could be explained by the fact that during the successive measurements of the normal-state resistance, the value fluctuates by an amount corresponding to a change in inductance of around 0.2 nH. Additionally, the qubit was exposed to air for a few hours after measuring the normal-state resistance and before the closure of the cryostat. This could have led to an additional change in the Josephson inductance. Nonetheless, considering that the desired value for the inductance can only be engineered through trial and error in the oxidation processes during the fabrication of the transmon, the achieved inductance and therefore anharmonicity of our qubit is well suited the upcoming experiments.
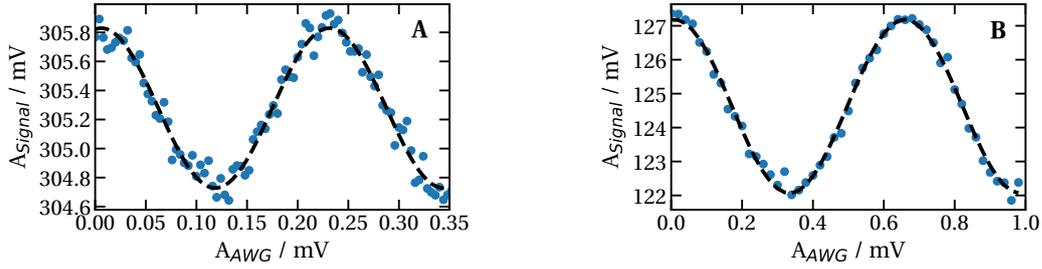
Figure 7.8: **Rabi oscillations. A** With a fixed pulse length of 400 ns send trough the storage cavity, the state of the qubit is rotated by π for an amplitude of 0.226(2) V. The measurements (dots) are fitted to a cosine (dashed line). **B** Since the readout cavity is more weakly coupled to the transmission line, the π rotation is achieved for 0.651(4) V.

7.2.3 Dispersive shift

To determine the dispersive shift between the qubit and the two cavities, we are going to compare the resonance frequencies of the cavities while the qubit is in the ground state to the resonance frequencies when the qubit is excited. To do so, we first have to determine the necessary amplitude or duration of the pulse, to populate the $|e\rangle$ state of the transmon. To reduce the width of the qubit resonance, which will be beneficial in later experiments, we are now using the AWG to generate Gaussian-shaped pulses instead of rectangular ones.

Rabi oscillations

With a Rabi experiment, we can find the amplitude of a pulse, which corresponds to a π rotation given a certain pulse length. During the excitation pulse, the qubit's state rotates around the x-axis of the Bloch sphere and the angle of rotation increases with duration or amplitude of the pulse. Therefore, when fixing the duration, we can find the qubit oscillating between $|g\rangle$ and $|e\rangle$ while increasing the amplitude. To measure these rotations, we are using the fact that a change in the population of the ground state maps to a change in amplitude of the resonance peak. For this experiment, we are using a pulse length of 400 ns. The length corresponds to the 6σ width of the Gaussian. Points further from the center are set to zero. Afterwards, the resonance frequency of the cavity is probed with a 5 µs readout pulse.

The results can be seen in Figure 7.8. As shown in Equation (3.39), the measurement follows a cosine, which can be used for a fit to extract the oscillation period. When sending signals through the storage or the readout cavity, a π rotation is achieved for 0.113(2) V and 0.3251(2) V, respectively. The differences can be explained by the fact that the input signals have to pass the cavities, in which they are attenuated differently depending on the detuning between qubit and cavity resonance frequency.
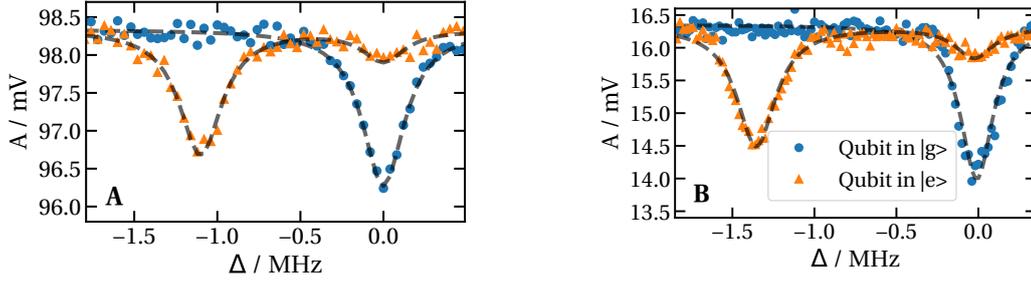
Figure 7.9: **Measurement of the state-dependent dispersive shift.** For the storage cavity (**A**) and the readout cavity (**B**) the resonance frequency with the qubit in the ground state (blue) shifts by 1.13(3) MHz and 1.34(2) MHz, respectively, when the qubit is excited (orange). Both peaks are fitted with a Lorentzian (dashed line). To improve the readability, the frequency axis is normalized to the resonance frequency of the unshifted cavity. In the measurement with the qubit in the excited state, a second peak appears, which corresponds to the qubit decaying during the readout pulse.

Dispersive shift

With this knowledge at hand, we can now determine the state-dependent dispersive shift easily. For this, we are recording a spectrum of the cavity's low-power peak with and without applying the π-pulse. With the qubit in the excited state, the center of the peak will shift by χ_{st} or χ_{rt}, which can be determined by fitting the peak to a Lorentzian. To record a spectrum with the setup mentioned above, we are varying the frequency of the readout pulse.

The results can be seen in Figure 7.9. The storage cavity is showing a state-dependent dispersive shift of $\chi_{st} = 1.13(3)$ MHz, while the storage cavity is shifted by $\chi_{rt} = 1.34(2)$ MHz. With these parameters, we can calculate the coupling rate g between the qubit and either one of the cavities. We find $g_{st} = 83.576(5)$ MHz and $g_{rt} = 183.477(4)$ MHz. Moreover, we can spot an unshifted peak even after π-pulsing the qubit. This can be explained by the qubit state decaying during the readout measurement. Since the readout pulse has a length of 5 µs and 73(2) % of the time, the qubit can be found in the ground state, we can already estimate the lifetime of the qubit with $T_1 = 16(2)$ µs.

7.2.4 Lifetime and coherence time of the qubit

To give a more precise value of T_1, we can measure the decay of the excited state directly. This can be done by exciting the qubit into the $|e\rangle$ state and applying the readout pulse after a waiting time τ. During that time, the probability of finding the qubit in the excited state decreases exponentially. For the determination of the qubit state, we switch back to the high-power readout procedure. The pulse sequence is shown in Figure 7.10 **A**, and the results can be seen in Figure 7.11 **A**. After fitting the measurement, we can extract a qubit lifetime of $T_1 = 14.5(3)$ µs.
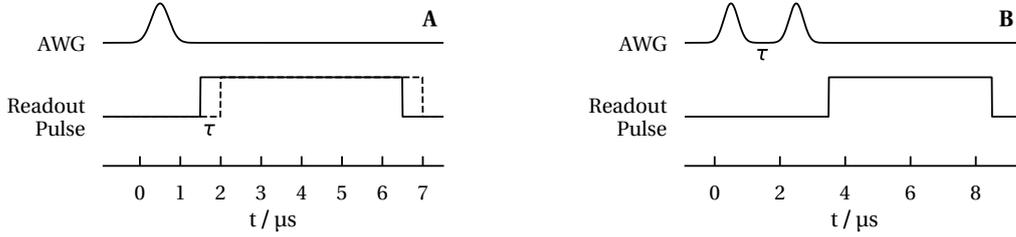
Figure 7.10: **Pulse sequences for the measurement of the life and coherence time of the qubit. A** Pulse sequence for determining T_1. During the waiting time, the qubit decays exponentially. **B** Pulse sequence for determining T_2^*. The phase between the two AWG pulses is changed depending on τ.

Coherence time

To determine the coherence time of the qubit T_2^*, we are performing a Ramsay-type experiment. The pulse sequence can be seen in Figure 7.10 **B**. We start by bringing the qubit into a superposition state $|\psi\rangle = (|g\rangle + |e\rangle)/\sqrt{2}$ using a calibrated 400 ns pulse. After a waiting time τ we are applying the same pulse with a phase shift, which depends on τ to create an oscillating signal. The intentional phase shift prevents us from interpreting small detuning effects as a decreased coherence time. After the second pulse, the readout pulse is applied, and we find an oscillating signal with an exponential envelope decaying as T_2^*.

The results can be seen in Figure 7.11 **B**. Fitting the signal, we can extract $T_2^* = 2.1(1)$ µs. This is much lower than T_1 meaning that the qubit is significantly affected by noise channels, which contribute to dephasing. Examples for this are interactions with the substrate [22], quasiparticle tunneling [69] and charge or flux noise. Additionally, since the qubit frequency depends on the number of photons in the cavity, fluctuations can also cause dephasing. To further determine possible noise sources, we performed the Ramsey-type experiment again with one spin echo. Since this resulted in the same coherence time, we can exclude slow noise channels like fluctuations in the qubit frequency. The short coherence time could, therefore, be explained by high-frequency noise, for example, excess microwave photons.

7.2.5 Self- and cross-Kerr coefficients of the cavities

To fully determine the system's Hamiltonian, we still have to find the self-Kerr coefficients K_r and K_s and the cross-Kerr coefficient χ_{rs} of the cavities. These parameters can be determined by measuring the resonance frequencies of the cavities depending on the number of photons inside the same or the other one. Therefore, we first have to relate the amplitude of the excitation pulse to the number of average photons, which will be trapped inside the cavity.
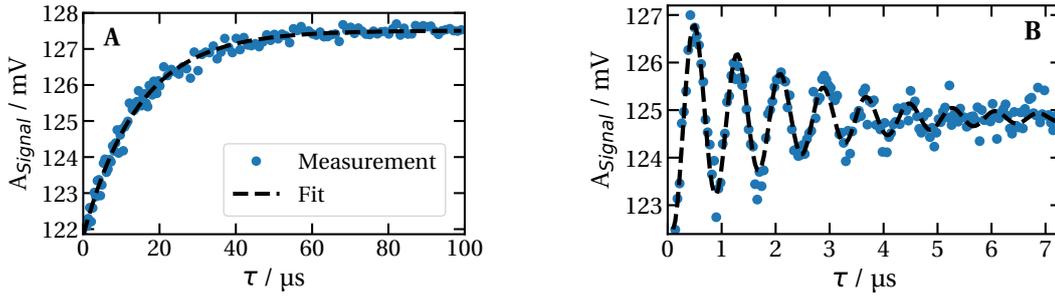
Figure 7.11: **Determining the lifetime and coherence time of the qubit. A** Measurement of the qubit's lifetime. After the initial excitation, the excited state of the qubit decays exponentially. Here we can see the exponential increase of the probability of finding the qubit in its ground state after a waiting time τ. The fit (dashed line) reveals a lifetime of $T_1 = 14.5(3)$ µs. **B** Measurement of the qubit's coherence time. The fit (dashed line) reveals a coherence time of $T_2^* = 2.1(1)$ µs.

Number splitting

Since the resonance frequency of the qubit depends on the number of photons inside one of the cavities, we can use the dispersive shift on the qubit to determine the average number of photons inside the cavity. The pulse sequence for this experiment, which is shown in Figure 7.12 **A**, starts by exciting one of the cavities with a 1 µs square pulse, which will displace the cavity state to a coherent state $|\alpha\rangle$. After this pulse, we are performing a qubit spectroscopy, during which the state of the qubit is read out through the other cavity.

In Figure 7.12 **B**, examples of the qubit spectroscopy are given. The peaks are corresponding to the different numbers of photons inside the cavity and are labelled with the Fock states. One thing to note here is that to be able to distinguish the multiple peaks clearly, we have to choose a wide enough Gaussian pulse for the excitation of the qubit. The photon number is following the Poisson distribution, which can be seen in Figure 7.12 **C**, where the probability of finding zero to five photons in the cavity depending on the power of the excitation pulse P_{in} is shown.

Now we can fit the distribution of the peaks for different cavity excitation powers to a Poisson distribution and relate them to the average number of the photons inside the cavity $\bar{n} = |\alpha|^2$. The relation between the power of the excitation pulse and the number of photons inside the cavities can be seen in Figure 7.13 **A**. For the storage cavity, we will trap 0.0806(4) photons per microwatt and for the readout cavity 0.124(3) photons per microwatt. The difference between these numbers can be explained by the difference in the coupling strength between the cavities and transmission line. Moreover, the fits show that within the error range there are no photons in the cavity for $P_{\mathrm{in}} = 0$, which confirms a sufficient cooling of the cavities.
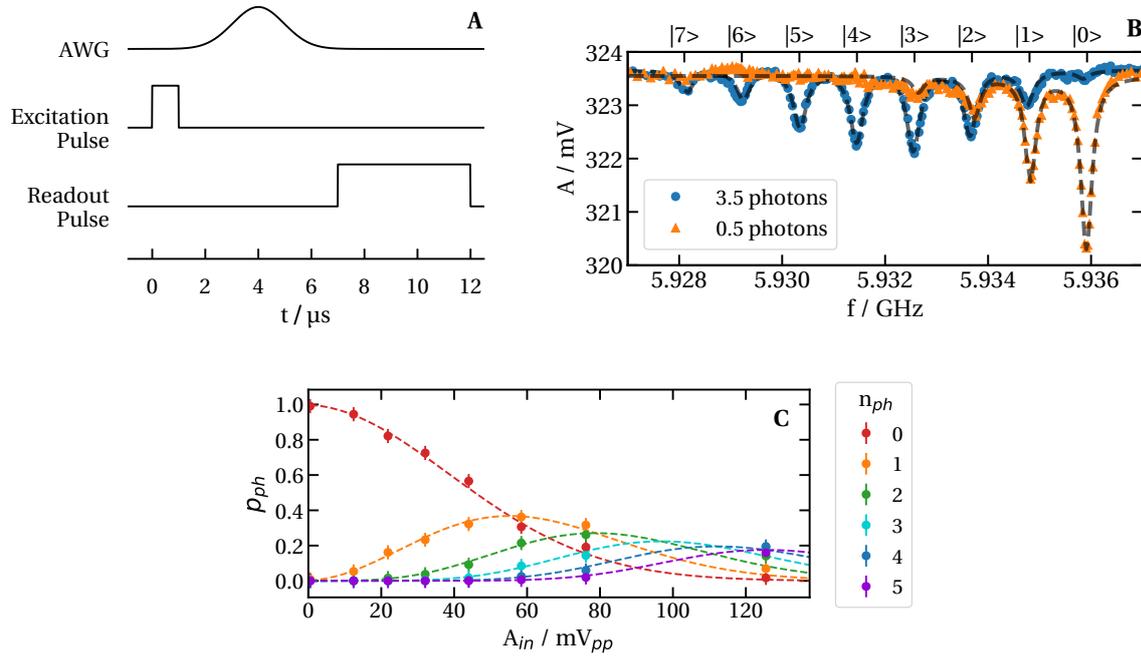
Figure 7.12: **Number splitting experiment. A** Pulse sequence for the determination of the average number of photons inside a cavity. **B** Qubit spectroscopy with a coherent state in the storage cavity. **C** The probability p_{ph} of finding n_{ph} photons in the readout cavity depending on the amplitude of the excitation pulse A_{in}. The values closely follow the Poisson fit shown as a dashed line.

Cavity-to-cavity Kerr coefficients

Now we can determine the cavity cross-Kerr coefficient by populating one of the cavities with a few photons and measuring the resonance frequency of the other one. Just like before, we start by applying an excitation pulse of 1 µs, and afterwards, we are recording a spectrum of the low-power peak of the other cavity with a 5 µs readout pulse. The resonance frequency is then plotted against the number of photons inside the cavity and fitted linearly to extract the cross-Kerr coefficient. Similarly, we can apply both pulses to the same cavity to fill them with photons additionally to the readout photons. The additional photons will cause the resonance frequency to shift, and we obtain the self-Kerr coefficients by a linear fit.

The results leading to the self- and the cross-Kerr coefficients can be seen in Figure 7.13 **B** and **C**, respectively. For the storage and readout cavity, we could measure a self-Kerr coefficient of K_{s} = -2.5(3) kHz and K_{r} = -3.7(2) kHz, respectively. This indicates that the readout cavity has inherited a larger proportion of the junction's nonlinearity, which was to be expected from the dispersive shift measurements. The cross-Kerr coefficient between the cavities is found to be χ_{sr} = -6.4(5) kHz.
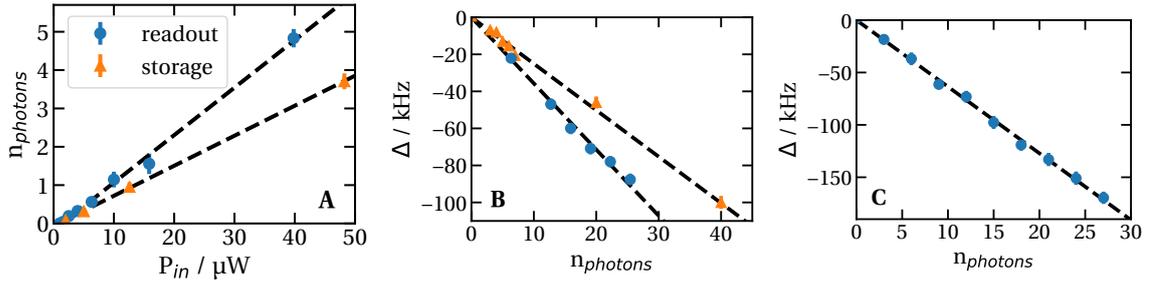
Figure 7.13: **Cavity self- and cross-Kerr. A** The relation between the power of the excitation pulse and the average number of photons inside the cavities. **B** The resonance frequency of the cavities as a function of the average number of photons in the same cavity. The relation is shown in blue for the storage cavity and in orange for the readout cavity. **C** The resonance frequency of the storage cavity as a function of the average number of photons in the readout cavity. The linear fits are shown as a dashed line.

7.2.6 Summary of the system parameters

In Table 7.3, a summary of all the system's parameters of the aluminum cavity-qubit system is given. Additionally, for comparison, the simulated parameters are shown. Overall, we find that the simulation closely matches the measured values. The resonance frequencies are only showing slight deviations of around 1 % or lower. Similarly, the measured dispersive shifts differ from the simulation by less than 10 % and considering the possible misalignment of the qubit, the values are overlapping within the error range. This deviation and the fact that χ_{st} and χ_{rt} are smaller than expected is most likely due to the lower anharmonicity of the simulated qubit. Looking at Equation (3.67), we see that a smaller anharmonicity is resulting in smaller dispersive shifts. However, even when neglecting the junction capacity in the simulation, we could not achieve an anharmonicity matching the measured value. One explanation for this deviation could be an uneven removal of the cavity's surface during the etching process. Removing more material in the region of the transmon's position would result in a smaller capacitance and therefore a larger anharmonicity.

The most striking deviation can be found in the self-Kerr coefficient of the storage cavity. However, this comes with no surprise since the self-Kerr coefficients of the cavities are highly dependent on the qubit's position. This high sensitivity is reflected in the large error of the simulated value. Moreover, K_s and K_r are a few hundred hertz lower than what Equation (3.67) would suggest for the measured dispersive shift. However, this is also true for the values extracted from the simulation through diagonalization, indicating that the fourth-order approximation systematically overestimates the state-dependent dispersive shift.

Table 7.3: **Comparison between the measured and simulated system parameters.** The lifetimes and coherence times of the cavities have been measured without the qubit using the time-domain cavity ring-down and the spectroscopy method, respectively.

Parameter	Measurement	Simulation	Deviation
$\omega_{\mathrm{s}}/2\pi$	4.633 837 45(4) GHz	4.628(1) GHz	1 %
$\omega_{\mathrm{t}}/2\pi$	5.93587(1) GHz	5.917(17) GHz	<1 %
$\omega_{\mathrm{r}}/2\pi$	8.77832827(6) GHz	8.778(1) GHz	<1 %
$\chi_{\mathrm{st}}/2\pi$	-1.13(3) MHz	-1.2(8) MHz	6 %
$\chi_{\mathrm{rt}}/2\pi$	-1.34(2) MHz	-1.4(7) MHz	4 %
$\chi_{\mathrm{rs}}/2\pi$	-6.4(5) kHz	-6(2) kHz	7 %
$K_{\mathrm{s}}/2\pi$	-2.5(3) kHz	-3.2(6) kHz	28 %
$K_{\mathrm{t}}/2\pi$	-153.27(3) MHz	-140(2) MHz	9 %
$K_{\mathrm{r}}/2\pi$	-3.7(2) kHz	-3.7(9) kHz	-
$g_{\mathrm{st}}/2\pi$	83.576(5) MHz	87.2(3) MHz	4 %
$g_{\mathrm{rt}}/2\pi$	183.447(4) MHz	199.1(3) MHz	9 %
$T_{1,\mathrm{s}}^{*}$	690(16) µs		
$T_{1,\mathrm{t}}^{*}$	14.5(3) µs		
$T_{1,\mathrm{r}}^{*}$	280(80) µs		
$T_{2,\mathrm{s}}^{*}$	680(16) µs		
$T_{2,\mathrm{t}}^{*}$	2.1(1) µs		
$T_{2,\mathrm{r}}^{*}$	280(80) µs		

The g factor is smaller than we would expect from the simulation. However, since this parameter was calculated using the anharmonicity, we are extracting a smaller g because of the lower anharmonicity in the simulation.

The life- and coherence times could not be simulated, but comparing T_1 and T_2^* between the storage cavity and the transmon, we find an over one order of magnitude longer lifetime for the cavity. The coherence time is over two orders of magnitude longer compared to the qubit. One thing to note here is that the cavity lifetimes and coherence times have been measured without the qubit in the system. We are expecting T_1 to decrease as soon as we couple the cavities to the qubit. To confirm this hypothesis, we would need to perform time-domain cavity ring-down measurements with the qubit inside. Our transmon's lifetime is quite typical for a 3D transmon. However, it is possible to reach much longer lifetimes. Transmons with a lifetime and coherence time of nearly 100 µs were reported years ago [12], but it is still a hard task to achieve such high

values. The short coherence time of our qubit could be explained by high-frequency noise, for example, excess microwave photons. To test this hypothesis, one could try to ensure a better thermalization of the output line or use additional filters to prevent stray photons from leaking into the cavity.

8 Conclusion and future directions

In this thesis, we could show how a coaxial cavity-qubit system can be designed from scratch and what needs to be considered during this process. Coaxial cavities are very well suited for their usage as a quantum memory. Since they are not only providing very high internal quality factors of above tens of millions and therefore photon lifetimes in the millisecond range but are also relatively easy to manufacture and small, which makes their use in dilution cryostats especially appealing. Our low-frequency cavity could achieve a lifetime and coherence time of 0.69(1) ms and 0.68(1) ms, respectively, for the single-photon level in the aluminum cavity and without the qubit in the system. Even longer lifetimes and coherence times could have been achieved with the niobium cavity system. However, due to the lack of time, we were not able to characterize the system again after the vacuum annealing.

The 3D transmon qubit, which was used in combination with the cavities, showed a lifetime of 14.5(3) µs. Therefore, storing the qubit state as a photon field inside the cavity, we would be able to increase the state's lifetime significantly.

The most difficult part of designing such a system is the integration process of the transmon into the cavity system. While everything needs to be packed tightly to ensure a strong coupling between the transmon and the cavity mode, we still have to leave a sufficient amount of room between the transmon antennas and the cavity wall to avoid suppression of the transmon's anharmonicity. In this thesis, we showed, how the desired system parameters, such as the coupling strength between the cavity and the transmon, can be designed step by step with finite element simulations. The comparison between the values extracted with the fourth-order approximation of the system's Hamiltonian and its diagonalization showed that higher-order terms still affect the parameters, especially the dispersive shift and the self-Kerr coefficients of the cavities.

Future directions

The next step would be to implement the conversion of a transmon state to a cavity state and back. This could be done using a four-wave mixing procedure, for example, mapping the qubit's ground state to a superposition of odd Fock states and the excited state to the even Fock states. Afterwards, the cavity state could be examined with Wiegner tomography.

In the long run, we could go even further and use the cavity mode as a qubit itself to ensure even longer lifetimes [70]. More importantly, we could then make use of the larger available Hilbert space to implement quantum error correction schemes, such as the *GKP code* by Gottesman, Kitaev, and Preskill proposed in 2001 [19]. This code has recently been demonstrated with superconducting cavities [71]. All these exciting developments are happing almost monthly and bring us one step closer to the final goal: building a universal quantum computer.

Bibliography

[1] Richard P. Feynman. Simulating physics with computers. *International Journal of Theoretical Physics*, 21(6):467–488, June 1982.

[2] Peter W. Shor. Polynomial-Time Algorithms for Prime Factorization and Discrete Logarithms on a Quantum Computer. *SIAM J. Comput.*, 26(5):1484–1509, October 1997.

[3] Lov K. Grover. A Fast Quantum Mechanical Algorithm for Database Search. In *Proceedings of the Twenty-eighth Annual ACM Symposium on Theory of Computing*, STOC '96, pages 212–219, New York, NY, USA, 1996. ACM. event-place: Philadelphia, Pennsylvania, USA.

[4] John Preskill. Quantum Computing in the NISQ era and beyond. *arXiv:1801.00862 [cond-mat, physics:quant-ph]*, January 2018. arXiv: 1801.00862.

[5] Sergio Boixo, Sergei Isakov, Vadim Smelyanskiy, Ryan Babbush, Nan Ding, Zhang Jiang, Michael J. Bremner, John Martinis, and Hartmut Neven. Characterizing Quantum Supremacy in Near-Term Devices. *Nature Physics*, 14:595–600, 2018.

[6] Suhas Kumar. Fundamental Limits to Moore's Law. November 2015.

[7] Gene M. Amdahl. Validity of the Single Processor Approach to Achieving Large Scale Computing Capabilities. In *Proceedings of the April 18-20, 1967, Spring Joint Computer Conference*, AFIPS '67 (Spring), pages 483–485, New York, NY, USA, 1967. ACM. event-place: Atlantic City, New Jersey.

[8] T. D. Ladd, F. Jelezko, R. Laflamme, Y. Nakamura, C. Monroe, and J. L. O'Brien. Quantum computers. *Nature*, 464(7285):45–53, March 2010.

[9] Daniel Loss and David P. DiVincenzo. Quantum computation with quantum dots. *Physical Review A*, 57(1):120–126, January 1998.

[10] Barbara M. Terhal. Quantum error correction for quantum memories. *Reviews of Modern Physics*, 87(2):307–346, April 2015.

[11] Hanhee Paik, D. I. Schuster, Lev S. Bishop, G. Kirchmair, G. Catelani, A. P. Sears, B. R. Johnson, M. J. Reagor, L. Frunzio, L. I. Glazman, S. M. Girvin, M. H. Devoret, and R. J. Schoelkopf. Observation of High Coherence in Josephson Junction Qubits Measured in a Three-Dimensional Circuit QED Architecture. *Physical Review Letters*, 107(24):240501, December 2011.

[12] Chad Rigetti, Jay M. Gambetta, Stefano Poletto, B. L. T. Plourde, Jerry M. Chow, A. D. Córcoles, John A. Smolin, Seth T. Merkel, J. R. Rozen, George A. Keefe, Mary B. Rothwell, Mark B.

Ketchen, and M. Steffen. Superconducting qubit in a waveguide cavity with a coherence time approaching 0.1 ms. *Physical Review B*, 86(10):100506, September 2012.

[13] G. Wendin. Quantum information processing with superconducting circuits: a review. *Reports on Progress in Physics*, 80(10):106001, September 2017.

[14] R. Barends, J. Kelly, A. Megrant, A. Veitia, D. Sank, E. Jeffrey, T. C. White, J. Mutus, A. G. Fowler, B. Campbell, Y. Chen, Z. Chen, B. Chiaro, A. Dunsworth, C. Neill, P. O'Malley, P. Roushan, A. Vainsencher, J. Wenner, A. N. Korotkov, A. N. Cleland, and John M. Martinis. Superconducting quantum circuits at the surface code threshold for fault tolerance. *Nature*, 508(7497):500–503, April 2014.

[15] D. Ristè, S. Poletto, M.-Z. Huang, A. Bruno, V. Vesterinen, O.-P. Saira, and L. DiCarlo. Detecting bit-flip errors in a logical qubit using stabilizer measurements. *Nature Communications*, 6:6983, April 2015.

[16] A. D. Córcoles, Easwar Magesan, Srikanth J. Srinivasan, Andrew W. Cross, M. Steffen, Jay M. Gambetta, and Jerry M. Chow. Demonstration of a quantum error detection code using a square lattice of four superconducting qubits. *Nature Communications*, 6:6979, April 2015.

[17] Matthew Reagor, Wolfgang Pfaff, Christopher Axline, Reinier W. Heeres, Nissim Ofek, Katrina Sliwa, Eric Holland, Chen Wang, Jacob Blumoff, Kevin Chou, Michael J. Hatridge, Luigi Frunzio, Michel H. Devoret, Liang Jiang, and Robert J. Schoelkopf. Quantum memory with millisecond coherence in circuit QED. *Physical Review B*, 94(1):014506, July 2016.

[18] Isaac L. Chuang, Debbie W. Leung, and Yoshihisa Yamamoto. Bosonic quantum codes for amplitude damping. *Physical Review A*, 56(2):1114–1125, August 1997.

[19] Daniel Gottesman, Alexei Kitaev, and John Preskill. Encoding a qubit in an oscillator. *Physical Review A*, 64(1):012310, June 2001.

[20] Barry C. Sanders, Stephen D. Bartlett, and Hubert de Guise. From Qubits to Continuous-Variable Quantum Computation. *arXiv:quant-ph/0208008*, August 2002. arXiv: quant-ph/0208008.

[21] Michel Devoret, Benjamin Huard, Robert Schoelkopf, and Leticia Cugliandolo. *Quantum Machines: Measurement and Control of Engineered Quantum Systems: Lecture Notes of the Les Houches Summer School: Volume 96, July 2011*. Oxford University Press, June 2014.

[22] Jens Koch, Terri M. Yu, Jay Gambetta, A. A. Houck, D. I. Schuster, J. Majer, Alexandre Blais, M. H. Devoret, S. M. Girvin, and R. J. Schoelkopf. Charge-insensitive qubit design derived from the Cooper pair box. *Physical Review A*, 76(4):042319, October 2007.

[23] Deutsch David and Jozsa Richard. Rapid solution of problems by quantum computation. *Proceedings of the Royal Society of London. Series A: Mathematical and Physical Sciences*, 439(1907):553–558, December 1992.

[24] P.W. Shor. Algorithms for quantum computation: discrete logarithms and factoring. In *Proceedings 35th Annual Symposium on Foundations of Computer Science*, pages 124–134, Santa Fe, NM, USA, 1994. IEEE Comput. Soc. Press.

[25] James N. Eckstein and Jeremy Levy. Materials issues for quantum computation. *MRS Bulletin*, 38(10):783–789, October 2013.

[26] B. P. Lanyon, J. D. Whitfield, G. G. Gillett, M. E. Goggin, M. P. Almeida, I. Kassal, J. D. Biamonte, M. Mohseni, B. J. Powell, M. Barbieri, A. Aspuru-Guzik, and A. G. White. Towards quantum chemistry on a quantum computer. *Nature Chemistry*, 2(2):106–111, February 2010.

[27] Cornelius Hempel, Christine Maier, Jonathan Romero, Jarrod McClean, Thomas Monz, Heng Shen, Petar Jurcevic, Ben P. Lanyon, Peter Love, Ryan Babbush, Alán Aspuru-Guzik, Rainer Blatt, and Christian F. Roos. Quantum Chemistry Calculations on a Trapped-Ion Quantum Simulator. *Physical Review X*, 8(3):031022, July 2018.

[28] Lilian Childress and Ronald Hanson. Diamond NV centers for quantum computing and quantum networks. *MRS Bulletin*, 38(2):134–138, February 2013.

[29] O. Gargiulo, S. Oleschko, J. Prat-Camps, M. Zanner, and G. Kirchmair. Fast flux control of 3d transmon qubits using a magnetic hose. *arXiv:1811.10875 [cond-mat, physics:quant-ph]*, November 2018. arXiv: 1811.10875.

[30] Michael A. Nielsen and Isaac L. Chuang. *Quantum Computation and Quantum Information*. Cambridge University Press, Cambridge ; New York, October 2000.

[31] Michael Tinkham. *Introduction to Superconductivity*. Courier Corporation, 2004. Google-Books-ID: VpUk3NfwDIkC.

[32] Michel Devoret, Benjamin Huard, Robert Schoelkopf, and Leticia Cugliandolo. *Quantum Machines: Measurement and Control of Engineered Quantum Systems: Lecture Notes of the Les Houches Summer School: Volume 96, July 2011*. Oxford University Press, June 2014.

[33] B. D. Josephson. The discovery of tunnelling supercurrents. *Reviews of Modern Physics*, 46(2):251–254, April 1974.

[34] B. D. Josephson. Possible new effects in superconductive tunnelling. *Physics Letters*, 1(7):251–253, July 1962.

[35] Jiansong Gao. *The physics of superconducting microwave resonators*. phd, California Institute of Technology, 2008.

[36] B. V. Noumerov. A Method of Extrapolation of Perturbations. *Monthly Notices of the Royal Astronomical Society*, 84(8):592–602, June 1924.

[37] V. Bouchiat, D. Vion, P. Joyez, D. Esteve, and M. H. Devoret. Quantum coherence with a single Cooper pair. *Physica Scripta*, 1998(T76):165, 1998.

[38] Y. Nakamura, Yu A. Pashkin, and J. S. Tsai. Coherent control of macroscopic quantum states in a single-Cooper-pair box. *Nature*, 398(6730):786, April 1999.

[39] K. W. Lehnert, K. Bladh, L. F. Spietz, D. Gunnarsson, D. I. Schuster, P. Delsing, and R. J. Schoelkopf. Measurement of the excited-state lifetime of a microelectronic circuit. *Physical Review Letters*, 90(2):027002, January 2003.

[40] Mooij, Orlando, Levitov, Tian, van der Wal CH, and Lloyd. Josephson persistent-current qubit. *Science (New York, N.Y.)*, 285(5430):1036–1039, August 1999.

[41] Friedman, Patel, Chen, Tolpygo, and Lukens. Quantum superposition of distinct macroscopic states. *Nature*, 406(6791):43–46, July 2000.

[42] I. Chiorescu, Y. Nakamura, C. J. P. M. Harmans, and J. E. Mooij. Coherent Quantum Dynamics of a Superconducting Flux Qubit. *Science*, 299(5614):1869–1871, March 2003.

[43] Yang Yu, Siyuan Han, Xi Chu, Shih-I. Chu, and Zhen Wang. Coherent temporal oscillations of macroscopic quantum states in a Josephson junction. *Science (New York, N.Y.)*, 296(5569):889–892, May 2002.

[44] John M. Martinis, S. Nam, J. Aumentado, and C. Urbina. Rabi Oscillations in a Large Josephson-Junction Qubit. *Physical Review Letters*, 89(11):117901, August 2002.

[45] Jacob Zachary Blumoff. *Multiqubit experiments in 3D circuit quantum electrodynamics*. PhD thesis, Yale University, 2017.

[46] F. Motzoi, J. M. Gambetta, P. Rebentrost, and F. K. Wilhelm. Simple Pulses for Elimination of Leakage in Weakly Nonlinear Qubits. *Physical Review Letters*, 103(11):110501, September 2009.

[47] R. Versluis, S. Poletto, N. Khammassi, N. Haider, D. J. Michalak, A. Bruno, K. Bertels, and L. DiCarlo. Scalable quantum circuit and control for a superconducting surface code. *arXiv:1612.08208 [quant-ph]*, December 2016. arXiv: 1612.08208.

[48] E. M. Purcell. Spontaneous Emission Probabilities at Radio Frequencies. In Elias Burstein and Claude Weisbuch, editors, *Confined Electrons and Photons: New Physics and Applications*, NATO ASI Series, pages 839–839. Springer US, Boston, MA, 1995.

[49] Christopher Gerry and Peter Knight. *Introductory Quantum Optics*. Cambridge University Press, Cambridge, UK ; New York, November 2004.

[50] Matthew Reagor. *Superconducting Cavities for Circuit Quantum Electrodynamics*. PhD thesis, Yale University, 2015.

[51] M. Lenander, H. Wang, Radoslaw C. Bialczak, Erik Lucero, Matteo Mariantoni, M. Neeley, A. D. O'Connell, D. Sank, M. Weides, J. Wenner, T. Yamamoto, Y. Yin, J. Zhao, A. N. Cleland, and John M. Martinis. Measurement of energy decay in superconducting qubits from nonequilibrium quasiparticles. *Physical Review B*, 84(2):024501, July 2011.

[52] Ioan M. Pop, Kurtis Geerlings, Gianluigi Catelani, Robert J. Schoelkopf, Leonid I. Glazman, and Michel H. Devoret. Coherent suppression of electromagnetic dissipation due to superconducting quasiparticles. *Nature*, 508(7496):369–372, April 2014.

[53] C. Wang, Y. Y. Gao, I. M. Pop, U. Vool, C. Axline, T. Brecht, R. W. Heeres, L. Frunzio, M. H. Devoret, G. Catelani, L. I. Glazman, and R. J. Schoelkopf. Measurement and control of quasiparticle dynamics in a superconducting qubit. *Nature Communications*, 5:5836, December 2014.

[54] Simon E. Nigg, Hanhee Paik, Brian Vlastakis, Gerhard Kirchmair, S. Shankar, Luigi Frunzio, M. H. Devoret, R. J. Schoelkopf, and S. M. Girvin. Black-Box Superconducting Circuit Quantization. *Physical Review Letters*, 108(24):240502, June 2012.

[55] Susanne Richer. Perturbative Analysis of Two-Qubit Gates on Transmon Qubits. *MA thesis*, 2013.

[56] D. I. Schuster, A. A. Houck, J. A. Schreier, A. Wallraff, J. M. Gambetta, A. Blais, L. Frunzio, J. Majer, B. Johnson, M. H. Devoret, S. M. Girvin, and R. J. Schoelkopf. Resolving photon number states in a superconducting circuit. *Nature*, 445(7127):515–518.

[57] M. D. Reed, L. DiCarlo, B. R. Johnson, L. Sun, D. I. Schuster, L. Frunzio, and R. J. Schoelkopf. High-Fidelity Readout in Circuit Quantum Electrodynamics Using the Jaynes-Cummings Nonlinearity. *Physical Review Letters*, 105(17):173601, October 2010.

[58] Alang Kasim Harman, Susumu Ninomiya, and Sadao Adachi. Optical constants of sapphire (α-Al2o3) single crystals. *Journal of Applied Physics*, 76(12):8032–8036, December 1994.

[59] David M. Pozar. *Microwave Engineering, 4th Edition*. Wiley, November 2011. Google-Books-ID: JegbAAAAQBAJ.

[60] Hasan Padamsee. *RF Superconductivity: Science, Technology, and Applications*. John Wiley & Sons, April 2009. Google-Books-ID: Pfo2js9IdrIC.

[61] PotashCorp. Bright Dipping Aluminum. 2015.

[62] V. Palmieri. New Materials for Superconducting Radiofrequency Cavities. Tsukuba, Japan, 2001.

[63] Vinay Ambegaokar and Alexis Baratoff. Tunneling Between Superconductors. *Physical Review Letters*, 10(11):486–489, June 1963.

[64] Kurtis Lee Geerlings. *Improving Coherence of Superconducting Qubits and Resonators*. PhD thesis, Yale University, 2013.

[65] S. Probst, F. B. Song, P. A. Bushev, A. V. Ustinov, and M. Weides. Efficient and robust analysis of complex scattering data under noise in microwave resonators. *Review of Scientific Instruments*, 86(2):024706, February 2015.

[66] David Zöpfl. Characterisation of stripline resonators in a waveguide. *MA thesis*, 2017.

[67] A. Bruno, G. de Lange, and S. Asaad. Reducing intrinsic loss in superconducting resonators by surface treatment and deep etching of silicon substrates | Request PDF, 2015.

[68] Jens Knobloch. Basic Concepts of Measurements Made on Superconducting RF Cavities. 1998.

[69] G. Ithier, E. Collin, P. Joyez, P. J. Meeson, D. Vion, D. Esteve, F. Chiarello, A. Shnirman, Y. Makhlin, J. Schriefl, and G. Schon. Decoherence in a superconducting quantum bit circuit. *Physical Review B*, 72(13):134519, October 2005. arXiv: cond-mat/0508588.

[70] Kevin S. Chou, Jacob Z. Blumoff, Christopher S. Wang, Philip C. Reinhold, Christopher J. Axline, Yvonne Y. Gao, L. Frunzio, M. H. Devoret, Liang Jiang, and R. J. Schoelkopf. Deterministic teleportation of a quantum gate between two logical qubits. *Nature*, 561(7723):368–373, September 2018.

[71] P. Campagne-Ibarcq, A. Eickbusch, S. Touzard, E. Zalys-Geller, N. E. Frattini, V. V. Sivak, P. Reinhold, S. Puri, S. Shankar, R. J. Schoelkopf, L. Frunzio, M. Mirrahimi, and M. H. Devoret. A stabilized logical quantum bit encoded in grid states of a superconducting cavity. *arXiv:1907.12487 [quant-ph]*, July 2019. arXiv: 1907.12487.

[72] Serge Haroche. Nobel Lecture: Controlling photons in a box and exploring the quantum to classical boundary. *Reviews of Modern Physics*, 85(3):1083–1102, July 2013.

[73] Paul Heidler. Design and Fabrication of a Coaxial Microwave Cavity. Master's thesis, LFU, Innsbruck, 2019.

[74] IBM's Test-Tube Quantum Computer Makes History, December 2001.

[75] D. Vion, A. Aassime, A. Cottet, P. Joyez, H. Pothier, C. Urbina, D. Esteve, and M. H. Devoret. Manipulating the Quantum State of an Electrical Circuit. *Science*, 296(5569):886–889, May 2002.

[76] Jeremy Hsu. CES 2018: Intel's 49-qubit chip shoots for quantum supremacy. *IEEE Spectrum Tech Talk*, 2018.

[77] Yuanhao Wang, Ying Li, Zhang-qi Yin, and Bei Zeng. 16-qubit IBM universal quantum computer can be fully entangled. *npj Quantum Information*, 4(1):46, September 2018.

[78] Eyob A. Sete, John M. Martinis, and Alexander N. Korotkov. Quantum theory of a bandpass Purcell filter for qubit readout. *Physical Review A*, 92(1):012325, July 2015.

[79] Otto Brune. Synthesis of a Finite Two-terminal Network whose Driving-point Impedance is a Prescribed Function of Frequency. *Journal of Mathematics and Physics*, 10(1-4):191–236, 1931.

[80] R. M. Foster. A reactance theorem. *The Bell System Technical Journal*, 3(2):259–267, April 1924.

[81] E. T. Jaynes and F. W. Cummings. Comparison of quantum and semiclassical radiation theories with application to the beam maser. *Proceedings of the IEEE*, 51(1):89–109, January 1963.

[82] Brian Vlastakis, Gerhard Kirchmair, Zaki Leghtas, Simon E. Nigg, Luigi Frunzio, S. M. Girvin, Mazyar Mirrahimi, M. H. Devoret, and R. J. Schoelkopf. Deterministically Encoding Quantum Information Using 100-Photon Schrödinger Cat States. *Science*, 342(6158):607–610, November 2013.

[83] Christopher S. Wang, Jacob C. Curtis, Brian J. Lester, Yaxing Zhang, Yvonne Y. Gao, Jessica Freeze, Victor S. Batista, Patrick H. Vaccaro, Isaac L. Chuang, Luigi Frunzio, Liang Jiang, S. M. Girvin, and Robert J. Schoelkopf. Quantum simulation of molecular vibronic spectra on a superconducting bosonic processor. *arXiv:1908.03598 [quant-ph]*, August 2019. arXiv: 1908.03598.

[84] Yvonne Y. Gao, Brian J. Lester, and Yaxing Zhang. Programmable Interference between Two Microwave Quantum Memories. *Physical Review X*, 8(2):021073, June 2018.

A Python scripts

The module contains two functions. The first may be used to calculate the resonance frequencies and the zero-point fluctuations. It will also determine the coupling parameters with the fourth-order approximation and the RWA. The second function contains the code for the diagonalization of the full Hamiltonian.

```python
def with_approximation(x,y,l_j=7*10**(-9)):
    ''' Determine the zero point fluctuations from the simulation
        of the admittance Y of a three-mode system using only up to
        fourth order therms and applying the RWA. (The resonace
        frequency of the qubit is the centre frequency. Only used
        the simulated points close to the zero crossings)

        Params:
            x (list): list of frequencies (as omega/2pi)
            y (list): simulated admittance
            l_j (float): Junction inductance in H

        Return:
            f_r (np.array): resonance frequencies (as omega/2pi)
            chi_matrix (np.array): coupling frequencies
                                    (as omega/2pi)
            f_zpf (np.array): zero point fluctuations
                                (as omega/2pi)

        Print:
            f_r, chi_matrix, E_J, E_C, E_J/E_C
    '''

    import numpy as np
    from lmfit.models import QuadraticModel
    import bokeh.models
    import bokeh.plotting as bp
    from bokeh.layouts import gridplot
    from bokeh.io import output_notebook

    y_old = y[0]
    counter = 0
    num_points = len(y)
    x_zero = np.zeros((3,6))
    y_zero = np.zeros((3,6))
    search_window = 3

    #Find the points nearest to the zero crossing
    #to determine the zeros of Y

    for i in range(num_points):
        if y[i]*y_old < 0 and y[i] > 0:
            x_zero[counter,:] = x[i-search_window:i+search_window]
```

```
44                y_zero[counter,:] = y[i-search_window:i+search_window]
45                counter += 1
46          y_old = y[i]
47
48      #Determine the slope, the points are fitted with a parabola
49
50      def parabola(x,a,b,c):
51          y = a*x**2 + b*x + c
52          return y
53
54      def slope(x,a,b):
55          y = 2*a*x + b
56          return y
57
58      #Specify the starting point for the fitting routine
59
60      a_start = [400.913, 2.394e-05, -19.663]
61      b_start = [-3496.052, 0., 345.143]
62      c_start = [7621.592087057387, 0., -1514.524088566597]
63
64      a = []
65      b = []
66      c = []
67
68      for i in range(3):
69          mod = QuadraticModel()
70          pars = mod.guess(y_zero[i,:], x=x_zero[i,:])
71          pars['a'].set(value=a_start[i])
72          pars['b'].set(value=b_start[i])
73          pars['c'].set(value=c_start[i])
74          result = mod.fit(y_zero[i,:],
75                           pars, x=x_zero[i,:])
76          a.append(result.best_values['a'])
77          b.append(result.best_values['b'])
78          c.append(result.best_values['c'])
79
80      #Ploting the fits for review
81
82      Y_fits = {}
83      for i in range(3):
84          Y_fits[str(i)] = bp.figure(plot_width=250,
85                                     plot_height=150,
86                             x_range=[x_zero[i,0]-
87                                      x_zero[i,1]+
88                                      x_zero[i,0],
89                                      x_zero[i,-1]+
90                                      x_zero[i,1]-
91                                      x_zero[i,0]],
92                             y_range=[y_zero[i,0]-
93                                      y_zero[i,1]+
94                                      y_zero[i,0],
95                                      y_zero[i,-1]+
96                                      y_zero[i,1]-
```

```
 97                                      y_zero[i,0]])
 98          x_plot = np.linspace(x_zero[i,0]-x_zero[i,1]
 99                               +x_zero[i,0],
100                               x_zero[i,-1]+x_zero[i,1]
101                               -x_zero[i,0],
102                               num=50)
103          Y_fits[str(i)].line(x_plot,parabola(x_plot,a[i],b[i],
104                                        c[i]),color='red')
105          Y_fits[str(i)].circle(x_zero[i,:],y_zero[i,:],
106                                color='blue')
107
108      bp.show(gridplot([[Y_fits[str(0)],Y_fits[str(1)],
109                        Y_fits[str(2)]]]))
110
111      #Calulate the zeros and the slops
112
113      m = []
114      f_r = []
115      y_punkt = []
116
117      for i in range(3):
118          zero = ((-b[i]+np.sqrt(b[i]**2-4*a[i]*c[i]))/(2*a[i]))
119          if zero < x_zero[i,-1] and zero > x_zero[i,0]:
120              f_r.append(zero)
121          else:
122              f_r.append((-b[i]-np.sqrt(b[i]**2-4*a[i]*c[i]))/
123                        (2*a[i]))
124
125          m.append(slope(f_r[i],a[i],b[i]))
126
127
128      #Calculate the zero point fluctuations
129
130      h_quer = 1.054572*10**(-34)
131      h = h_quer*2*np.pi
132      e = 1.60217662*10**(-19)
133      L_j = l_j
134
135      #Qubit
136      Im_Y_dot_q = f_r[1]*m[1]
137      Z_q = 2/(Im_Y_dot_q)
138      alpha_q = e**2/(2*L_j*h_quer)*Z_q**2/(2*np.pi)
139
140      #Lower mode
141      Im_Y_dot_s = f_r[0]*m[0]
142      Z_s = 2/(Im_Y_dot_s)
143      alpha_s = e**2/(2*L_j*h_quer)*Z_s**2/(2*np.pi)
144
145      #Upper mode
146      Im_Y_dot_r = f_r[2]*m[2]
147      Z_r = 2/(Im_Y_dot_r)
148      alpha_r = e**2/(2*L_j*h_quer)*Z_r**2/(2*np.pi)
149
```

```python
150        #Chi: lower mode <-> qubit
151        chi_sq = 2*np.sqrt(alpha_q*alpha_s)
152
153        #Chi: upper mode <-> qubit
154        chi_rq = 2*np.sqrt(alpha_q*alpha_r)
155
156        #Chi: lower mode <-> upper mode
157        chi_sr = 2*np.sqrt(alpha_s*alpha_r)
158
159        E_J = (h_quer/(2*e))**2/L_j/h
160        C_q = 1/(f_r[1]*2*np.pi*10**9*np.sqrt(L_j))**2
161        E_C = alpha_q
162
163        f_zpf_s = np.sqrt(Z_s*h/2/(2*np.pi))
164        f_zpf_q = np.sqrt(Z_q*h/2/(2*np.pi))
165        f_zpf_r = np.sqrt(Z_r*h/2/(2*np.pi))
166
167        chi_matrix = np.zeros((3,3))
168
169        chi_matrix[0][0] = alpha_s
170        chi_matrix[1][1] = alpha_q
171        chi_matrix[2][2] = alpha_r
172
173        chi_matrix[0][1] = chi_sq
174        chi_matrix[1][0] = chi_sq
175
176        chi_matrix[2][1] = chi_rq
177        chi_matrix[1][2] = chi_rq
178
179        chi_matrix[0][2] = chi_sr
180        chi_matrix[2][0] = chi_sr
181
182        f_zpf = [f_zpf_s, f_zpf_q, f_zpf_r]
183
184        f_r = 10**9*np.array(f_r)
185
186        print('f_s = %.4f GHz'%f_r[0])
187        print('f_q = %.4f GHz'%f_r[1])
188        print('f_r = %.4f GHz'%f_r[2])
189        print('-------------------------------')
190        print('alpha_q = %.4f MHz'% (alpha_q/(10**6)))
191        print('alpha_s = %.4f kHz'% (alpha_s/(10**3)))
192        print('alpha_r = %.4f kHz'% (alpha_r/(10**3)))
193        print('-------------------------------')
194        print('chi_sq = %.4f MHz'% (chi_sq/(10**6)))
195        print('chi_rq = %.4f MHz'% (chi_sq/(10**6)))
196        print('chi_sr = %.4f kHz'% (chi_sq/(10**3)))
197        print('-------------------------------')
198        print('E_J = %.4f MHz'% (E_J/(10**6)))
199        print('E_C = %.4f MHz'% (E_J/(10**6)))
200        print('E_J/E_C = %.4f',% (E_J/E_C))
201
202        return f_r, chi_matrix, f_zpf
```

```python
def diagonalize_hamiltonian(f_s, l_j, f_zpfs, cos_trunc=6,
                            fock_trunc=6):
    ''' Full diagonalization of the transmon cavities system.
        Params:
            f_s (list): list of resonance frequencies
                        (as omega/2pi)
            f_zpf (np.array): zero point fluctuations
                              (as omega/2pi)
            l_j (float): Junction inductance in H
            cos_trunc (int): to set the cosine appoximation
            fock_trunc (int): to reduce the fock space

        Return:
            singe_mode_energy (np.array): dressed resonance
                                          frequencies
                                          (as omega/2pi)
            chi_matrix (np.array): coupling frequencies
                                   (as omega/2pi)

        Print:
            singe_mode_energy, chi_matrix
    '''

    import qutip
    import numpy as np
    from math import factorial as fact
    from scipy.constants import pi, hbar, e, h

    #Calculates the expansion of the cosine
    #starting at the forth order:

    def cos_approx(x):
        return sum((-1)**i * x**(2*i) / float(fact(2*i))
                   for i in range(2, cos_trunc + 1))

    f_s, l_j, f_zpfs = (np.array(x) for x in (f_s, l_j, f_zpfs))
    f_zpfs = np.transpose([[x] for x in f_zpfs])
    Phi_0 = hbar / (2*e)
    f_j = Phi_0**2 / (h*l_j)
    n_modes = len(f_s)

    #Generate the basic operators
    n = qutip.num(fock_trunc)
    a = qutip.destroy(fock_trunc)
    ad = a.dag()

    #Generate the number operators:
    n_ops = []
    for i in range(n_modes):
        raw_field_ops = [qutip.qeye(fock_trunc)]*n_modes
```

```
256              raw_field_ops[i] = n
257              n_ops.append(qutip.tensor(*raw_field_ops))
258
259          #Generate the field operators:
260          field_ops = []
261          for i in range(n_modes):
262              raw_field_ops = [qutip.qeye(fock_trunc)]*n_modes
263              raw_field_ops[i] = a+ad
264              field_ops.append(qutip.tensor(*raw_field_ops))
265
266
267          #Calculate the linear part of the Hamiltonian
268          H_lin = sum(x*y for x,y in zip(f_s, n_ops))
269
270          #Calculate the non-linear part of the Hamiltonian
271          cos_arg = [sum(x*y for x,y in zip(f_zpf/Phi_0, field_ops))
272                        for f_zpf in f_zpfs]
273          H_nonlin = -f_j*sum([cos_approx(x) for x in cos_arg])
274
275          #Creat the full Hamiltonian
276          H = H_lin + H_nonlin
277
278          #Calculate the eigenvalues and eigenvectors of H
279          eigenvalues, eigenvecs = H.eigenstates()
280
281          #normalisation of the energy values
282          eigenvalues -= eigenvalues[0]
283
284          #calulates the energy of single exitations for every mode
285          single_states = []
286
287          for i in range(n_modes):
288              exitations = [0]*n_modes
289              exitations[i] = 1
290              single_states.append(qutip.tensor(*[qutip.basis(fock_trunc,
291                                               i) for i in exitations]))
292
293          singe_mode_energy = [max(zip(eigenvalues, eigenvecs),
294                              key = lambda y : (x.dag()
295                                                 * y[1]).norm())[0]
296                              for x in single_states]
297
298          #Calculate the chis
299          chi_matrix = np.zeros((n_modes,n_modes))
300
301          for i in range(n_modes):
302              for j in range(i, n_modes):
303                  exitations = [0]*n_modes
304                  exitations[i] += 1
305                  exitations[j] += 1
306                  excited_state = qutip.tensor(*[qutip.basis(fock_trunc,
307                                               i) for i in exitations])
308                  energy_excited_state = max(zip(eigenvalues, eigenvecs),
```

```
309                                                 key = lambda y :
310                                                 ( excited_state.dag()
311                                                 * y[1]).norm())[0]
312             chi = (energy_excited_state - (singe_mode_energy[i]
313                                                 + singe_mode_energy[j]))
314             chi_matrix[i][j] = chi
315             chi_matrix[j][i] = chi
316
317     print('--------dressed frequencies---------')
318     print('f_q = %.4f GHz'% (singe_mode_energy[1]/(10**9)))
319     print('f_s = %.4f GHz'% (singe_mode_energy[0]/(10**9)))
320     print('f_r = %.4f GHz'% (singe_mode_energy[2]/(10**9)))
321     print('-------self-Kerr coefficients-------')
322     print('alpha_q = %.4f MHz'% (-chi_matrix[1][1]/(10**6)))
323     print('alpha_s = %.4f kHz'% (-chi_matrix[0][0]/(10**3)))
324     print('alpha_r = %.4f kHz'% (-chi_matrix[2][2]/(10**3)))
325     print('-------cross-Kerr coefficients------')
326     print('chi_sq = %.4f MHz'% (-chi_matrix[0][1]/(10**6)))
327     print('chi_rq = %.4f MHz'% (-chi_matrix[2][1]/(10**6)))
328     print('chi_sr = %.4f kHz'% (-chi_matrix[0][2]/(10**6)))
329     print('--------------------------------')
330
331     return singe_mode_energy , chi_matrix
```

B Technical drawings

Figures B.1 to B.3 are showing the exact dimensions for all cavities used in the experiments.
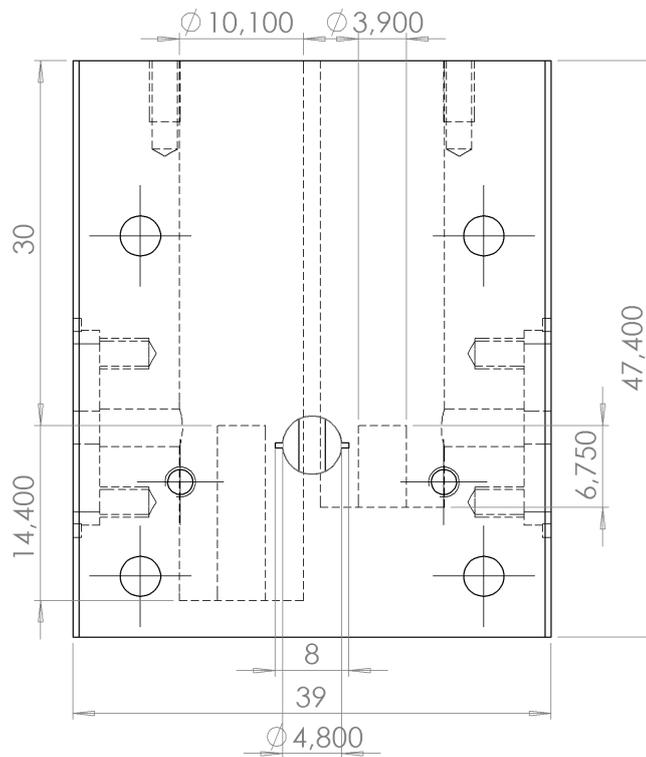
Figure B.1: Technical drawing of the cavity. (Front view)
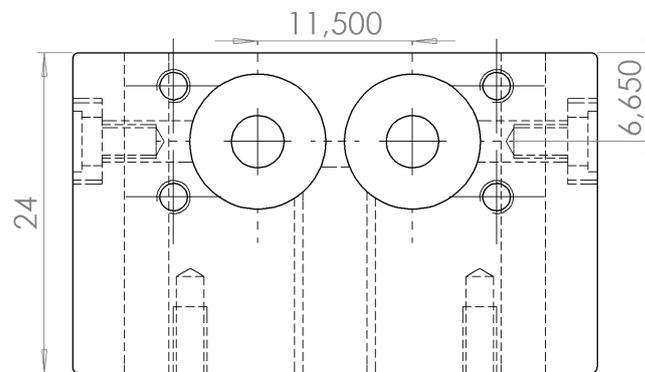
Figure B.2: Technical drawing of the cavity. (Top view)
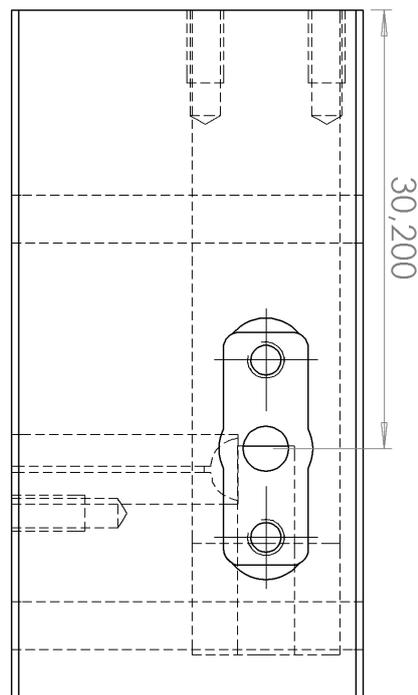
Figure B.3: Technical drawing of the cavity. (Side view)

C Formulas

The analytical solution for the time-dependent cavity response as developed by Paul Heidler:

$$P(t) = P_0 \cdot \left(\frac{1}{(Q_c + Q_i)^2 f_r^2 + 2Q_c Q_i \delta} \right)^2$$

$$\cdot \Bigg((2Q_c Q_i \delta)^2 + 4Q_i^2 f_r^2 \exp\left(-2\pi \left(\frac{(Q_c + Q_i)f_r}{Q_c Q_i} \right) t \right)$$

$$+ (Q_c - Q_i)^2 f_r^2 + 4 \exp\left(-\frac{\pi f_r (Q_c + Q_i)}{Q_c Q_i} t \right)$$

$$\cdot Q_i f_r ((Q_c - Q_i) f_r \cos(2\pi\delta t) - 2Q_c Q_i \delta \sin(2\pi\delta t)) \Bigg) \quad \text{(C.1)}$$

where $\delta = f_{\text{Pulse}} - f_r$ is the detuning between the frequency of the signal and the resonance frequency of the cavity.